INFORMATION TO USERS

This material was produced from a microfilm copy of the original document. While the most advanced technological means to photograph and reproduce this document have been used, the quality is heavily dependent upon the quality of the original submitted.

The following explanation of techniques is provided to help you understand markings or patterns which may appear on this reproduction.

1. The sign or "target" for pages apparently lacking from the document photographed is "Missing Page(s)". If it was possible to obtain the missing page(s) or section, they are spliced into the film along with adjacent pages. This may have necessitated cutting thru an image and duplicating adjacent pages to insure you complete continuity.

2. When an image on the film is obliterated with a large round black mark, it is an indication that the photographer suspected that the copy may have moved during exposure and thus cause a blurred image. You will find a good image of the page in the adjacent frame.

3. When a map, drawing or chart, etc., was part of the material being photographed the photographer followed a definite method in "sectioning" the material. It is customary to begin photoing at the upper left hand corner of a large sheet and to continue photoing from left to right in equal sections with a small overlap. If necessary, sectioning is continued again — beginning below the first row and continuing on until complete.

4. The majority of users indicate that the textual content is of greatest value, however, a somewhat higher quality reproduction could be made from "photographs" if essential to the understanding of the dissertation. Silver prints of "photographs" may be ordered at additional charge by writing the Order Department, giving the catalog number, title, author and specific pages you wish reproduced.

5. PLEASE NOTE: Some pages may have indistinct print. Filmed as received.

Xerox University Microfilms
300 North Zeeb Road
Ann Arbor, Michigan 48106

76-19,252

STEPHANY, William Phillip, 1937-
AN ABSOLUTE MEASUREMENT OF THE ^{6}Li (n,α) CROSS SECTION AT 964 keV.

The University of Michigan, Ph.D., 1976
Engineering, nuclear

Xerox University Microfilms, Ann Arbor, Michigan 48106

AN ABSOLUTE MEASUREMENT OF THE ^{6}Li (n,α) CROSS SECTION AT 964 keV

by
William Phillip Stephany

A dissertation submitted in partial fulfillment
of the requirements for the degree of
Doctor of Philosophy
(Nuclear Engineering)
in The University of Michigan
1976

Doctoral Committee:

Professor Glenn F. Knoll, Chairman
Professor Ziya A. Akcasu
Professor David R. Bach
Associate Professor John Bardwick
Professor John S. King

ACKNOWLEDGEMENTS

The author wishes to express his appreciation to Professor Glenn F. Knoll for incisive discussions throughout the course of this work and for encouraging support at some needed moments.

Also the author appreciatively recognizes the support he received from the Argonne Universities Association and the Atomic Energy Commission for a three year Fellowship in Nuclear Engineering. The author gratefully acknowledges the research project support received from the Atomic Energy Commission under Contract No. AT (11-1) - 2025.

This work could not have been completed without the constant cooperation of Dr. David Gilliam, the author's co-worker during the majority of time spent doing the research embodied in this dissertation. Several specific contributions for which the author expresses appreciation are the actual source calibrations, use of the tubular source support framework, and essential aid in design and construction of the low scatter laboratory facilities.

The inventiveness and knowledge of electronics freely offered by Dr. Raulf Polichar is gratefully acknowledged.

Dr. Ronald Fleming's contributions to the evaluation of numerous complexities encountered along the path are appreciated.

The patient and gracious cooperation of the staff of the University of Michigan's Ford Nuclear Reactor and Health Physics group as represented by Mr. Robert Martin, Mr. Gary Cook, Mr. George Ford, Mr. Arthur Solari and Mr. Richard Neville is gratefully acknowledged.

The author also wishes to acknowledge the assistance of several students in the Nuclear Engineering Department who have worked on the research project. The efforts of Mr. Gregory Moses, Mr. John Gunning and Mr. John Engdahl are appreciated.

The time and energy of the author's wife, Suzanne, for typing and editing the dissertation are sincerely appreciated.

TABLE OF CONTENTS

	Page
Acknowledgements	ii
List of Tables	ix
List of Figures	xii
Chapter	
I. Introduction	1
A. Motivation	1
B. Experimental Work in Perspective	1
II. Equipment and Facilities	4
A. Photoneutron and Photon Sources	4
B. Photoneutron Laboratory	6
C. Detector-Target Composite	8
D. Detection System	10
E. Detector Mount and Support Frame	13
F. Manganese Bath	16
III. Experimental Procedure	18
A. Overview of the Procedure	18
B. Description of Major Procedures	20
1. Preparation of Detector and Experiment Package	20
2. System Calibrations and Background Counting	21
3. Photon and Photoneutron Experiments	22
4. Manganese Bath Runs	24
5. Gamma Activity Comparisons	24
IV. Primary Data-Neutron Events	26
A. Preliminaries	26

		Page
1.	System Calibration	26
2.	System Noise and Spurious Background	27
3.	Detector Performance	29
4.	Photon Background Subtraction Techniques	30
B.	Neutron Induced Events	34
1.	General Comments	34
2.	Neutron Events for Each Data Acquisition Interval	36
3.	Statistical Evaluation of the Data	39
V.	Secondary Data	50
A.	Neutron Activity Determination	50
1.	Saturated Count Rates	50
2.	Integrated Neutron Activities	51
a.	General Comments	51
b.	Parasitic Absorption Correction	52
c.	Neutron Leakage Correction	52
d.	Deuterium Photoneutron Correction	52
e.	Source Yield Evaluation	53
B.	Mean Scalar Fluence	56
1.	General Comments	56
2.	Source-Target Spacing	56
a.	General Comments	56
b.	Source-Reference Plate Spacing	56

		Page
	c. Reference Plate Thickness	58
	d. Target Surface to Reference Plate Distance	58
	e. Corrections to the Source-Target Spacing Values	61
	3. Neutron Current per Unit Source Strength	63
	a. General Comments	63
	b. Source-Target Spatial Distribution	63
C.	Number of Target Nuclei	67
	1. General Comments	67
	2. Monitor Foil Deposit Mass Thickness	69
	3. Determination of Target Areas	71
	4. Calculation of the Number of Target Nuclei	73
D.	Photoneutron Source Spectrum	74
VI.	Corrections	76
A.	Detection Efficiency	76
	1. General Comments	76
	2. Reaction Product Energies, Emission Angles and Range Data	77
	3. Near Target Efficiency	82
	4. Far Target Efficiency	85
B.	Local Inscatter	89
	1. Analytic Model	89
	2. Inscatter Due to Hydrogen in Epoxy	93

Page

3. Inscatter Due to Non-hydrogenous Components 97

C. Charged Particle Production 102

1. General Comments 102

2. Analysis of Charged Particle Sources 103

a. Proton Yield from the Air Envelope 103

b. Proton Yield from the Epoxy Fillet 112

3. Summary of Charged Particle Correction 113

VII. Cross Section Evaluation 115

A. Integral Value of the $^{6}Li(n,\alpha)$ Cross Section 115

1. General Comments 115

2. Method One -- Algebraic Elimination of the Room Return Flux Contribution 115

3. Method Two -- The Apparent Cross Section 119

B. Value of the $^{6}Li(n,\alpha)$ Cross Section at 964 keV 122

C. Error Evaluation 125

1. General Comments 125

2. Estimated Uncertainty in the Integral Cross Section 126

3. Estimated Uncertainty in the Cross Section Value at 964 keV 131

VIII. Conclusion 135

A. Comparison with Other Data 135

		Page
B.	Comments and Suggestions	137
Appendix I.	Tabulated Photoneutron Source Energy Spectrum	139
Appendix II.	$^{6}Li(n,\alpha)$ Cross Section Shape Function as Reported by Friesenhahn (Fri, 74) as Used to Determine σ_{964}	140
List of References		141

LIST OF TABLES

		Page
Table 2.1.	Photoneutron Source Specifications	5
Table 2.2	Operating Characteristics of Surface Barrier Detector	9
Table 3.1.	Sequence of Experimental Procedures for Cross Section Measurement	18
Table 4.1.	Measured System Noise Level and Spurious Background Counts	28
Table 4.2.	Data Acquisition Sequence for the Cross Section Measurement	35
Table 4.3.	Primary Events from the Close Spacing Experiment	37
Table 4.4.	Primary Events from the Far Spacing Experiment	38
Table 4.5.	Number of Primary Events per Interval Compared with the Mean--Close Spacing Run	42
Table 4.6.	Number of Primary Events per Interval Compared with the Mean--Far Spacing Run	43
Table 4.7.	Primary Counts Used for Cross Section Evaluation	49
Table 5.1.	Saturated Count Rates for Activity Determination	51
Table 5.2.	Bath Correction Factors and Neutron Activity of the Na-Be Source	54
Table 5.3.	Initial and Integrated Source Neutron Activities	55
Table 5.4.	Measured Reference Sphere to Plate Distances for Close and Far Spacing Experiments	58
Table 5.5.	Source Center to Target Surface Spacing Results	61

Table 5.6.	Summary of Source-Target Spacing Results	62
Table 5.7	Results for Determining $J^{\bullet}$ (R_0)	65
Table 5.8	Mean Scalar Fluence and Intermediate Values for the Close and Far Spacing Experiments	68
Table 5.9	Weight Gain of Monitor Foils Reported by ORNL	70
Table 5.10	Results of Target Mass Thickness Determination	71
Table 5.11	Measured Target Deposit Diameters and Calculated Areas	73
Table 5.12	Summary of Results for the Number of Target Nuclei	74
Table 6.1.	Summary of Detection Efficiency Calculation for the Near Target	85
Table 6.2.	Triton and Alpha Angular Ranges for Particle Escape from the Far Target toward Detector	87
Table 6.3.	Summary of Detection Efficiency Calculations for the Far Target	88
Table 6.4.	Chemical Composition of ORTEC "High Vac" Epoxy	93
Table 6.5.	Geometric Variables for Evaluating Lavite Ring Inscattering	99
Table 6.6.	Summary of Results for Inscattering Corrections Due to Components of the Experimental Package	100
Table 6.7.	Relative Flux Perturbation Due to Local Inscatter	102
Table 6.8.	Calculated Proton Count for Close and Far Spacing Experiments	107

Table 6.9.	Error Terms for the $^{14}N(n,p)$ Correction	110
Table 6.10.	Summary of Charged Particle Correction and Its Effect on Primary Event Data	114
Table 7.1.	Values Used in Equations 7.A.2 and 7.A.3 to Determine the Cross Section	117
Table 7.2.	Integral Cross Section Values and Room Return Contributions Obtained by Solution of Equations 7.A.2 and 7.A.3	118
Table 7.3.	Values of the Apparent Cross Section and Its Linearly Dependent Variables	122
Table 7.4.	Variable Values and Associated Errors for Determination of the Integral Cross Section	127
Table 7.5.	Independent Error Sources	129
Table 7.6.	Cross Correlated Error Sources	130
Table 7.7	Effect of Source Spectrum Calibration on σ_{964}	132
Table 7.8.	Effect of the $^{6}Li(n,\alpha)$ Cross Section Shape Function on σ_{964}	133
Table 7.9.	Summary of Final Cross Section Values and Errors	134

LIST OF FIGURES

		Page
Figure 2.1.	Photoneutron Laboratory	7
Figure 2.2.	Schematic Diagram of Pulse Processing System	11
Figure 2.3.	Schematic Diagram of Electrical Connections to Detector	12
Figure 2.4.	Detector and Mock Source in Support Frame	14
Figure 4.1.	Typical Data from Photoneutron Source Run	31
Figure 4.2.	Primary Events per Interval above Gamma Region Compared with the Mean --Close Spacing Run	44
Figure 4.3.	Primary Events per Interval Obtained by Gamma Background Subtraction Compared with the Mean--Close Spacing Run	44
Figure 4.4	Total Number of Primary Events per Interval Compared with the Mean-- Close Spacing Run	45
Figure 4.5.	Primary Events per Interval above Gamma Region Compared with the Mean --Far Spacing Run	45
Figure 4.6.	Primary Events per Interval Obtained by Gamma Background Subtraction Compared with the Mean--Far Spacing Run	46
Figure 4.7.	Total Number of Primary Events per Interval Compared with the Mean--Far Spacing Run	46
Figure 4.8.	Total Number of Primary Events per Interval Compared with the Mean, Excluding I-B-7--Close Spacing Run	48
Figure 5.1.	Schematic Cross Section of Detector and Mount	60

Figure 5.2	Computed Spectrum of Na-Be Photoneutron Source (NPL Monte Carlo Code)	75
Figure 6.1.	Alpha and Triton Energy, and Alpha Emission Angle as a Function of Triton Emission Angle	78
Figure 6.2.	Cumulative Triton Yield as a Function of Emission Angle	79
Figure 6.3.	Alpha Particle Range in LiF	81
Figure 6.4.	Triton Range in LiF	81
Figure 6.5.	Schematic Representation of Near Target and Detector for Efficiency Calculations	82
Figure 6.6.	Schematic Representation of the Far Target and Detector for Efficiency Calculations	86
Figure 6.7.	Diagram for Inscatter Evaluation	90
Figure 6.8.	Cross Sectional View of Epoxy Fillets, Lavite Ring and Target Deposits	94
Figure 6.9.	Air Envelope Coupled with Detector for $^{14}N(n, p)$ Correction--Close Spacing Run	106
Figure 6.10.	Pulse Height Spectrum and $^{14}N(n, p)$ Correction--Close Spacing Run	108
Figure 6.11.	Pulse Height Spectrum and $^{14}N(n, p)$ Correction--Far Spacing Run	109
Figure 7.1.	The Apparent Integral Cross Section	121
Figure 7.2.	$^{6}Li(n,\alpha)$ Cross Section Shape Function and Integral Neutron Source Spectrum	124
Figure 8.1.	Comparison of this Result with Other Values	136

CHAPTER I

INTRODUCTION

A. Motivation.

The $^{6}Li\ (n,\alpha)\ H^{3}$ reaction has been applied in fast neutron spectroscopy because of its high Q-value and lack of competing reactions to 1.72 MeV (Ut, 71). The semiconductor sandwich spectrometer (Ric, 72)and LiI (Eu) scintillator (Bab, 61) are the principal detection devices used in this application. In addition, the absence of competing reactions and the simplicity of its structure makes the $^{6}Li\ (n,\alpha)$ cross section desirable as a standard for flux normalization in the energy range from thermal to 1.7 MeV. However, the confidence level of the cross section value in the high keV energy range is only 15% to 20% precluding its use as a standard and the need for precise absolute measurements has been pointed out frequently (Der, 70; Ut, 71).

B. Experimental Work in Perspective.

The ^{24}Na-Be photoneutron source, producing nearly monoenergetic neutrons at 964 keV, is ideally suited for making the $^{6}Li\ (n,\alpha)$ cross section measurement required. Not only is the neutron energy highly desirable but the source yield can be absolutely determined by the manganese bath method.

Previous measurements of the $^{6}Li\ (n,\alpha)$ cross section

revealed inaccuracies in the ^{6}Li content, large multiple scattering corrections (using Li-loaded glass scintillators) or thick LiF samples to be major error sources (Ut, 71). The experiment was designed to eliminate these obstacles. Thin LiF targets were vapor deposited directly onto the surfaces of a fully depleted surface barrier detector, with the ^{6}Li enrichment measured by mass spectrographic analysis after vapor deposition. Thus the previously recognized problems of multiple scattering encountered using Li-loaded glass scintillators, inaccurate knowledge of the ^{6}Li content of the target, and large target self-absorption corrections were bypassed. This technique of using a Na-Be photoneutron source, with the neutron yield absolutely determined by the manganese bath method, combined with the use of thin ^{6}LiF targets directly applied to the electrodes of a surface barrier detector, is a unique attempt at determination of this cross section. Since establishment of a cross section as a reference standard requires absolute determination of its value by independent methods to assure elimination of possible unknown systematic error sources, this measurement offers a valuable contribution.

The significance of its contribution must also be gauged by the precision obtained. In this sense, the measurement did not achieve its goal. The gains made

in overcoming previous obstacles were diminished because of unanticipated difficulties encountered. The detector's behavior in the high gamma flux (estimated as approximately 10^9 gamma/cm^2-sec), a significant inscatter correction caused by the detector mount and, finally, a large correction for unanticipated proton events occurring in the air envelope surrounding the detector led to a final error of 18% in the value.

CHAPTER II

EQUIPMENT AND FACILITIES

A. Photoneutron and Photon Sources.

The photoneutron source used in this work is a 3 cm diameter sphere of sodium fluoride surrounded by a 3mm thick shell of metallic beryllium. The beryllium shell was not encapsulated. The inner sphere was composed of reagent grade sodium fluoride with 1% by weight of aluminum added. The aluminum was added to enable machining without shattering. The sphere was formed by cold pressing, giving a density of 89.5% of theoretical density.

The beryllium shell was fabricated in the form of two hemispheres. Attempts to produce a "snap fit" junction between the hemispheres, implemented by cooling one shell, failed. The hemispheres were joined by using four beryllium pins through the hemispheres. The source was never absolutely sealed, and a gap of several mils thickness around the equator of the source between the hemispheres was observed. This gap was filled by wrapping in 4 mil diameter beryllium wire secured by spot welding. The wire stopped the movement of the shells which was induced by the unavoidable jarring of the source during remote handling. The dimensions and masses of the source are summarized in Table 2.1.

Table 2.1.

Photoneutron Source Specifications

NaF Core Diameter	2.954 cm
Be Shell, I.D.	3.01 cm
Be Shell, O.D.	3.596 cm
Be Mass	18.73 gms
NaF Mass	30.96 gms
Al Mass	0.313 gms

The diameter of the NaF sphere was intentionally made slightly less than the inner diameter of the Be shell to allow for thermal expansion during irradiation, since the coefficient of thermal expansion of NaF is approximately three times that of Be. Prior to the first irradiation the source was x-rayed and observed to be homogeneous. The x-raying also showed the NaF sphere to be partially cracked. This is not significant in terms of the uniformity of the neutron activity of the source but was an added reason for us to add the Be wire to assure rigidity of the shell.

The source neutron yield was estimated for design purposes using the work of Bensch and Vesely (Ben, 69). These results were confirmed by our experience with numerous irradiations. We estimated the gamma activity regularly achieved during a 15 hour irradiation in the Ford Reactor to be 30 Ci, with the corresponding neutron

activities close to 3.5×10^7 neutrons/sec.

The spatial uniformity of the ^{24}Na activity produced by neutron irradiation was of major concern. This was achieved by positioning the source at the vertical midplane of the 2 Mw pool-type Ford Reactor core in a thermal neutron flux of approximately 10^{12} n/cm^2sec. During the irradiation the source was continuously rotated at 3 rev/min.

During activation the source was sealed in a thin walled Al can which was filled with compacted Al foil balls to assure good heat transfer with minimal flux depression. The cans were carefully checked for leak tightness prior to submersion into the core.

The photon source, used for background measurements in this work, is a machined Al sphere with a 4 cm outer diameter, having a thickness of 5 mm. The 3 cm diameter spherical cavity of the source was filled with powdered NaF. The filling hole was then welded shut. The mass of NaF was determined by weight gain of the source after filling to be 22.7 gms.

This photon source was activated to achieve equal ^{24}Na activity as that of the photoneutron source, with irradiation times based on the ratio of the NaF masses.

B. Photoneutron Laboratory.

The floor plan of the photoneutron laboratory is shown in Figure 2.1. The entire inner surface of the

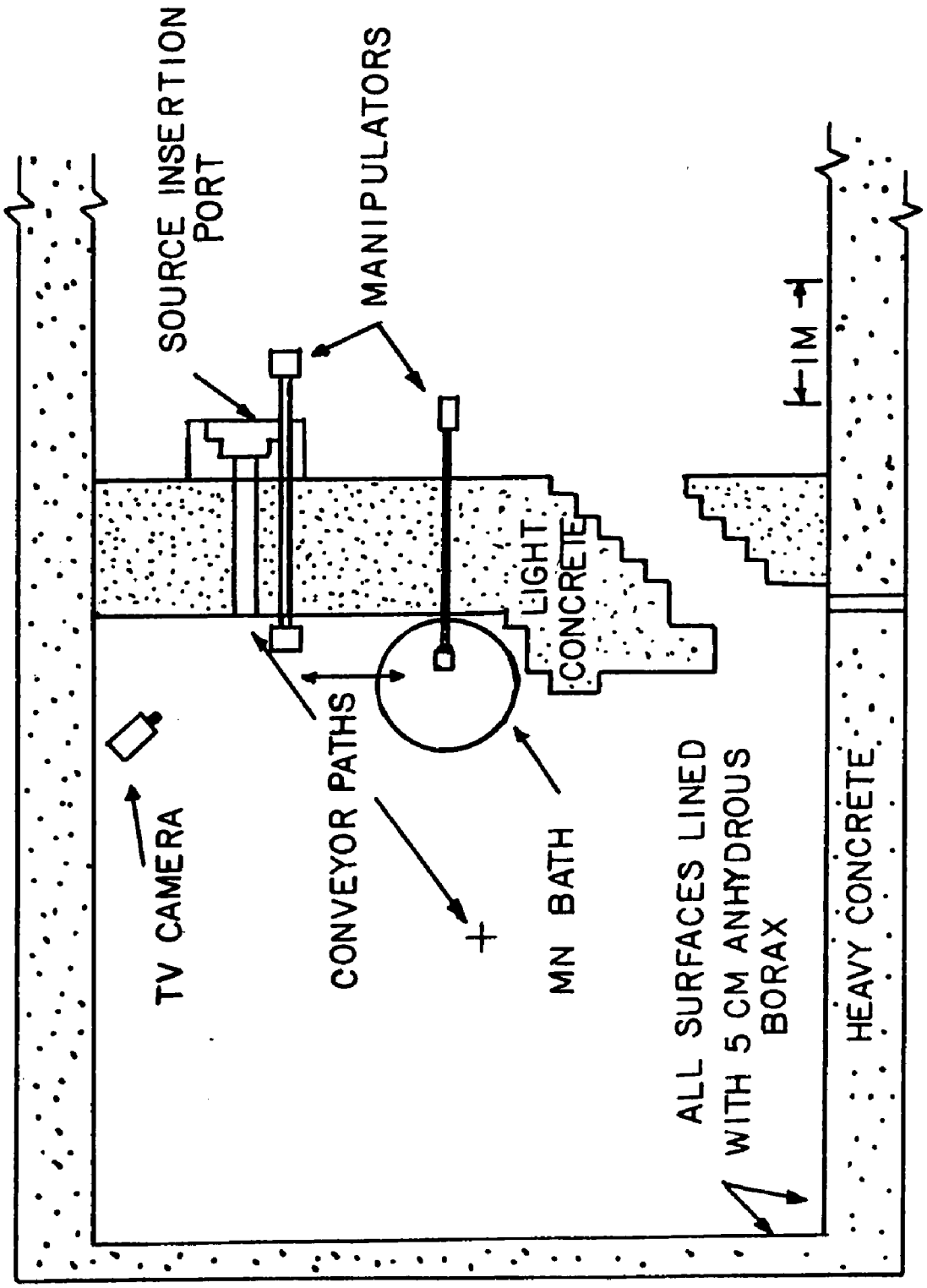


Figure 2.1. Photoneutron Laboratory

shielded area was lined with 5 cm of anhydrous borax. The borax was heat sealed in 4 mil thick polyethylene bags to retard moisture absorption. The bags themselves are contained in cardboard beam-like boxes secured to the ceiling and walls of the room by Unistrut supports. The average radius of the experimental area (the root mean inverse square room-center to room-surface distance) is 2.1 meters.

The cave area of the laboratory was built to allow safe remote handling of up to 100 Ci of ^{24}Na activity. It has controlled air flow, simple master slave manipulators, a trolley to allow positioning of the experiment package at its geometric center, closed circuit television, a massive shield plug to prevent access when a source is present, and a remote source insertion port.

C. Detector-Target Composite.

A 40 micron thick totally depleted silicon surface barrier detector (Serial number 11-373B) purchased from ORTEC, Inc. was used to make the measurement. The detector has an active surface area of 200 mm^2. The operational characteristics of the detector are summarized in Table 2.2.

Table 2.2.

Operating Characteristics of

Surface Barrier Detector

	Original	At Time of Cross Section Measurement
Alpha Resolution, keV, FWHM	26.7	48
Noise Width, keV, FWHM	23	41
Sensitive Thickness, microns	42.5	same
Resistivity, Ω-cm	415	same
Reverse Current: __μamps at___volts	.42 at 40	1.2 at 30
Electrode Thickness, $\mu gms/cm^2$		
Au	40.0	same
Al	40.4	same

The values shown in Table 2.2 for the operating characteristics at the time of the cross section measurements were made without a gamma source. The performance degradation is suspected to be the result of radiation damage due to repeated use of the detector during preliminary experimental runs or to physical damage due to handling.

The target deposits were made by vapor deposition directly onto the Al and Au electrode surfaces. This

work was performed at the Isotope Target Laboratory at Oak Ridge National Laboratory. The target specifications called for 100 mm^2 deposits of ^6LiF to be centered on the electrode surfaces, with a mass thickness of 160 $\mu gms/cm^2$ to 180 $\mu gms/cm^2$. Deposit thicknesses of approximately 178 $\mu gms/cm^2$ were obtained. The thicknesses were determined during vapor deposition by the resonance frequency probe technique and subsequently confirmed be weight gain determinations on Al monitor foils surrounding the detector during the deposition process. The operating characteristics of the detector were measured before and after the targets were applied and no change was observed.

D. Detection System.

A schematic drawing of the pulse processing system is shown in Figure 2.2. Bias voltage was maintained and leakage current monitored using the ORTEC Model 210 Detector Control Unit. The ORTEC 204 Precision Pulse Generator was used to obtain relative calibration spectra, normalized using a ^{241}Am alpha source. The SSR-1120 amplifier was attached near the detector. Figure 2.3 is a schematic drawing of the electrical connections interfacing the detector with the pulser, detector control unit and the SSR-1120 amplifier.

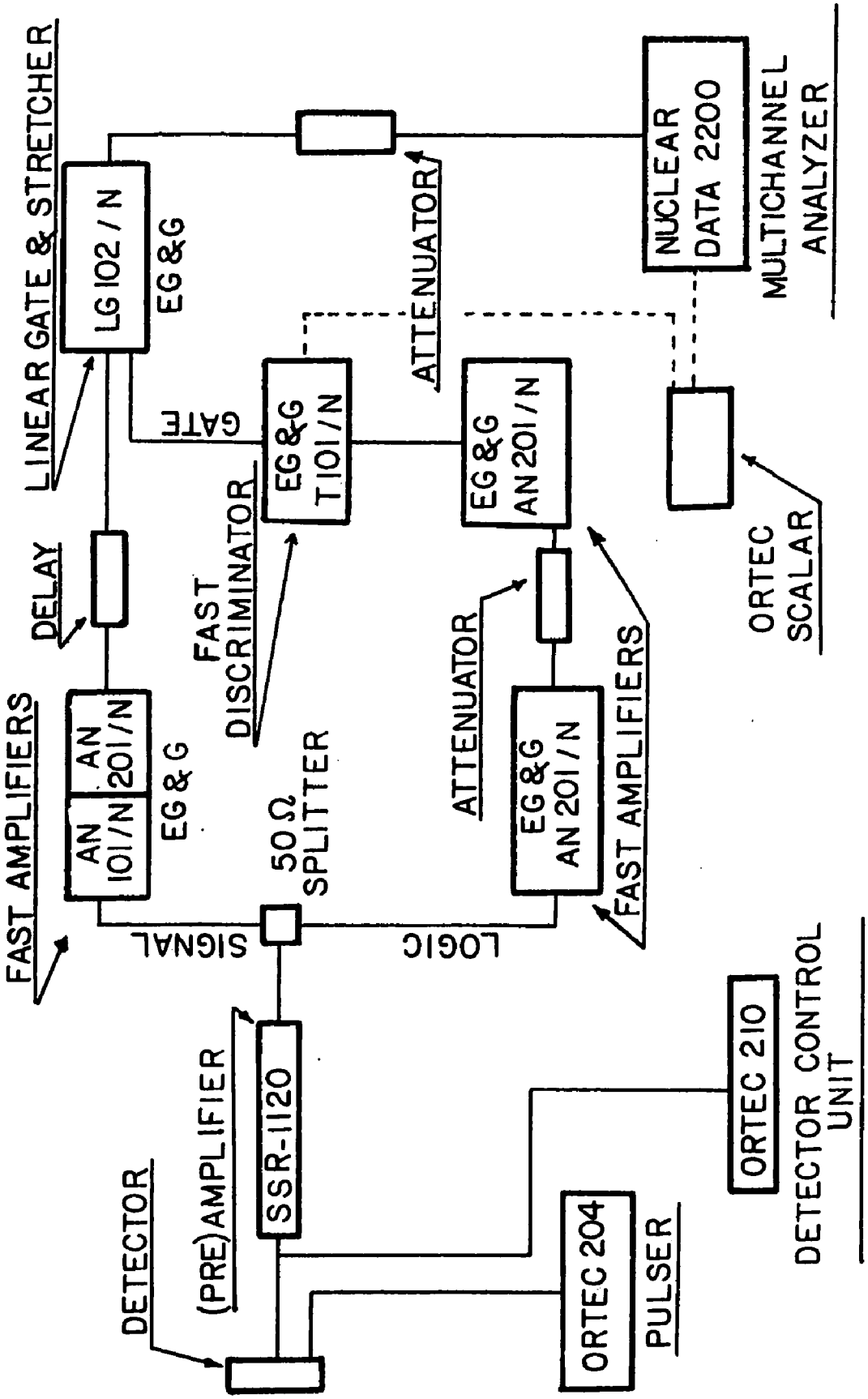
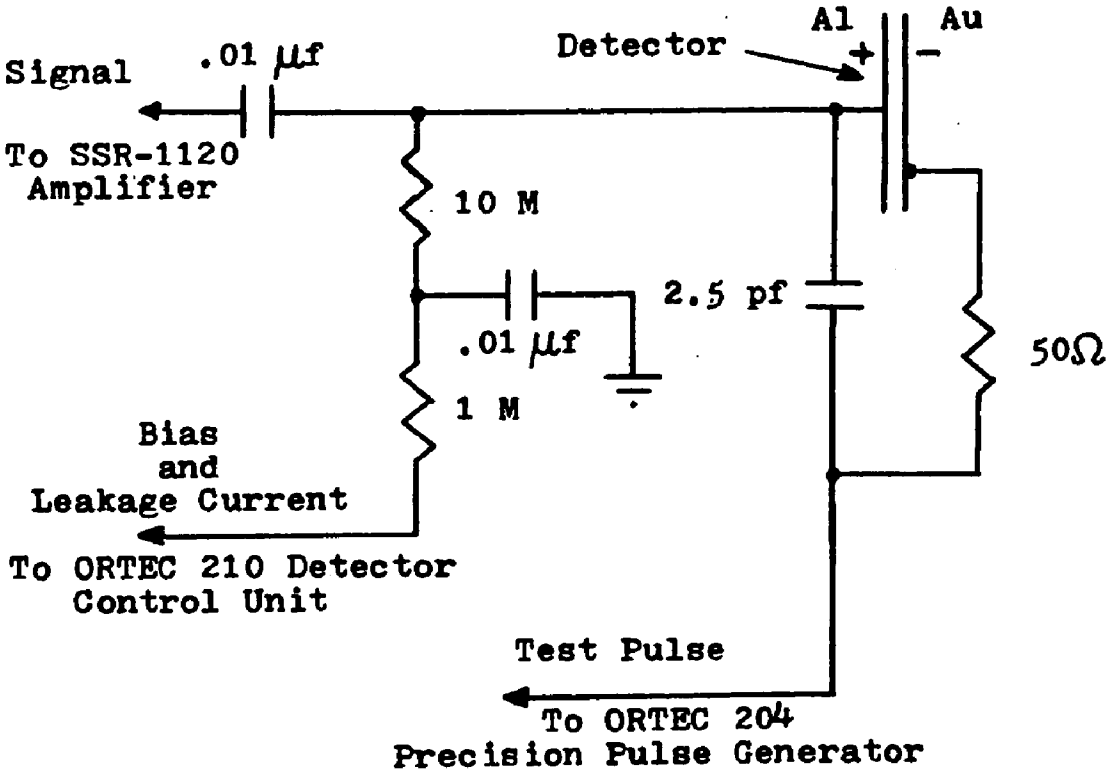


Figure 2.2. Schematic Diagram of Pulse Processing System

Figure 2.3.

Schematic Diagram of Electrical

Connection to Detector



The signal pulse leaving the SSR-1120 amplifier had a measured rise time (baseline to peak) of 12 nsec and a fall time (peak to baseline) of 130 nsec.

The output pulse from the SSR-1120 was split to use linear gating on the basis of amplitude discrimination. The T 101/N discriminator setting was adjusted such that the LG 102/N was enabled only when an event exceeding approximately 0.8 MeV was encountered.

The discriminator trigger level was determined by the requirement to maintain a count rate of less than

10^4/sec into the multichannel analyzer to assure linear pulse processing while recording as many of the gamma induced counts as possible. The scalar was put in the circuit as a convenient means of determining the low energy efficiency limit of the system as a function of discriminator setting.

The pulse shape was unaltered except for stretching to accomodate the input requirements of the multichannel analyzer. Because of the sensitivity of the system to Mhz frequencies meticulous electromagnetic shielding of the experiment package and cables was required.

E. Detector Mount and Support Frame.

The detector was mounted in an aluminum casing allowing electrical connections to be made and enabling it to be suspended from a 36 cm x 36 cm x 48 cm tubular support frame within a cadmium cylinder. The detector in its mount is shown suspended in the tubular frame in Figure 2.4.

The framework of the tubular support frame is made of 0.010 in. wall thickness, 3/8 in. O.D. stainless steel tubes and brass corner blocks. The detector mount was held in position by four pair of 1/8 in. diameter, 0.010 in. wall thickness stainless tubes. Each pair of tubes is connected at the far end to a brass sleeve which

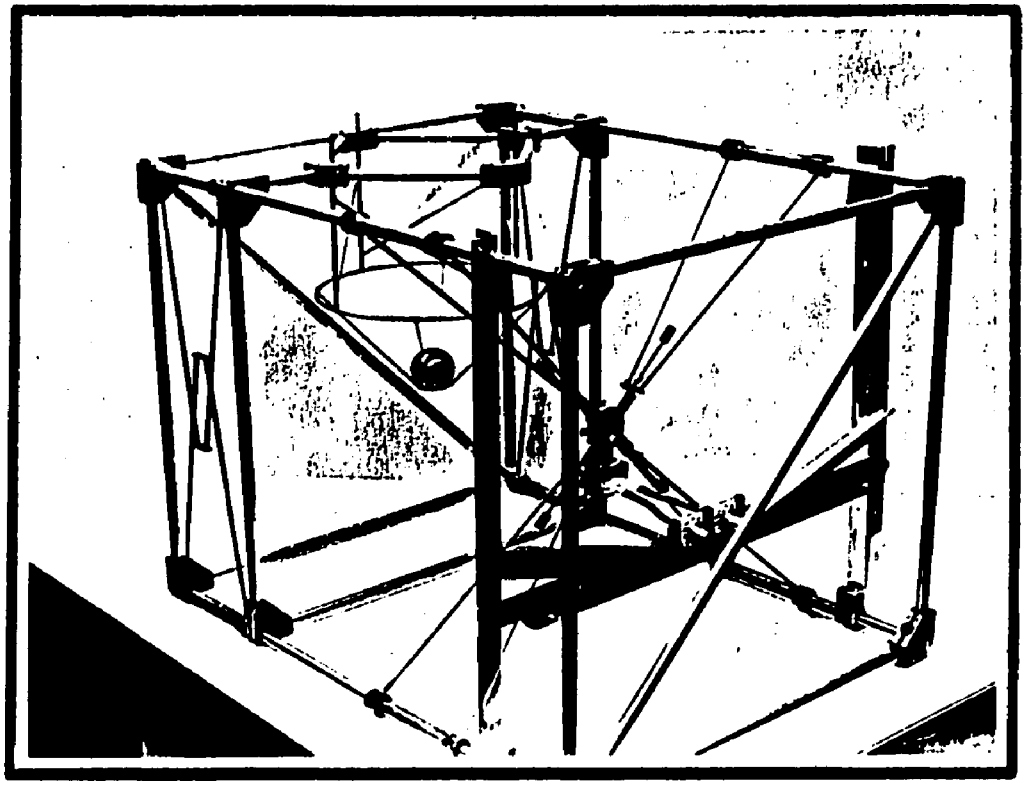


Figure 2.4. Detector and Mock Source in Support Frame

slides along the framework tubing. Small thumb screws (No. 2-56) enabled attachment of the detector mount to these 1/8 in. struts.

The source was supported by a closed ring of 0.060 in. diameter stainless steel wire. Wires of the same thickness extend from the source support ring upward to a 1/8 in.tube structure which joins to the main framework.

During the experiments the entire source-detector framework is enclosed in a 60 cm diameter by 60 cm high cadmium drum. The walls of the drum are 0.010 in. cadmium, supported by a lightweight aluminum and steel frame. This drum was filled with dry air during the experiments.

The detector mount consisted of two .050 in. thick plates of 7075-T6 aluminum, with internal teflon insulation and a pure aluminum gasket to contact the gold layer of the detector. The mass of the mount was mimimized by using 0.50 in. wide arms extending to join with the 1/8 in. stainless steel struts to connect it to the main tubular framework.

Doubly shielded, teflon insulated coaxial cable, grounded to the detector mount, was used to make the electrical connections. The cable shielding was directly soldered to the detector mount at a distance of 1.5 in. below the centerline of the detector. Two cables were attached. One cable interfaced the detector to the

SSR-1120 amplifier and ORTEC Detector Control Unit. The second cable connected the detector to the pulse generator. The cables were approximately 5 in. in length and mated with BNC connectors supported in a special cross mount in the tubular box framework. Short intermediate cables led from this connection point to BNC bulkhead connectors mounted in the cadmium drum, enabling connection with the external electronic system.

F. Manganese Bath.

The manganese bath system consists of a spherical tank with a radius of 46.8 cm. An aqueous manganous sulfate solution is pumped through the sphere at a flow rate refilling the sphere every five minutes. A dry source well extends from the top of the bath to a point somewhat below the center to allow positioning of the source at the bath center. The manganous sulfate solution is continuously stirred and sampled by recirculation of the solution, with a part of the recirculated liquid passing through a lucite detector chamber. The recirculating liquid returns to the sphere at eight uniformly spaced points on its surface.

An important feature of the system is that the bath fluid can be pumped from the spherical tank in the low scatter laboratory and stored in an auxiliary storage tank in an adjoining room when low albedo conditions are required in the laboratory for a cross section measurement.

The ^{56}Mn activity is monitored by a 3 in. x 3 in. NaI crystal in a dry well in the lucite detector chamber. The pulses are amplified, processed through a single channel analyzer, and counted in multiscaling mode by a multichannel analyzer. The timing for the multiscaling is provided by a crystal base timer having an accuracy of $\pm$ 0.004%.

CHAPTER III

EXPERIMENTAL PROCEDURE

A. Overview of the Procedure.

The experimental procedure is summarized in Table 3.1.

Table 3.1.

Sequence of Experimental Procedures

For Cross Section Measurement

1. Close Space Run (9 cm)
   - A. Preparation of the Detector and Experiment Package
   - B. System Calibration and Background Counting
   - C. Photon Source Run
   - D. Calibration Check and Background Counting
   - E. Photoneutron Source Run
   - F. Manganese Bath Run with Photoneutron Source
   - G. Manganese Bath Run with NBS-II
   - H. Gamma Activity Comparison Using Ge-Li System

II. Far Spacing Run (20 cm)

Same as Above

Each experimental sequence required about five days, excluding the gamma activity comparison measurements which necessitated allowing the sources to decay about seven days so that dead time corrections for the Ge-Li

system would be insignificant. All of the measurements were completed during the same reactor cycle so that empirical estimates of source activities for the far spacing experimental sequence would be accurate. The actual data runs using the photon or photoneutron source required approximately 24 hours. During these runs the manganous sulfate solution was stored in the remote storage tank then pumped into the comparator sphere after removal of the photoneutron source from the low scatter cave. The manganese bath system was then allowed to come to thermal equilibrium. The bath electronic system was then adjusted and background counting initiated. Background data was acquired for approximately four hours. The photoneutron source was then inserted into the bath and data acquired. Following removal of the photoneutron source from the bath, after allowing the ^{56}Mn activity to decay to background, NBS-II was inserted to obtain the data necessary for source yield comparison.

Both the photon and photoneutron sources were each allowed to decay seven days from the time of removal from the reactor core to the Ge-Li gamma activity comparison measurements. They were allowed to decay three more days before semi-remote preparation for reactivation.

B. Description of Major Procedures.

1. Preparation of Detector and Experiment Package.

The detector was outgassed at 10^{-8} Torr overnight prior to placing it in the mount. Except for the time required to mount it and align it in the tubular support framework it was kept in a dry air environment. The detector was secured in the aluminum detector mount, which was then suspended in the tubular support framework.

A four piece positioning jig was used to facilitate alignment of the detector mount in the tubular frame. Before removing the jig the position of the detector was fixed by tightening the set and thumb screws coupling the detector mount to the tubular frame. The positioning jig was then removed and a flat reference plate was carefully attached to the surface of the detector mount facing toward the source support ring. A precision chrome sphere was placed in the source support ring and a series of measurements of the sphere surface to reference plate surface was made. The tubular framework rested on a steel machining flat during these measurements.

Calibrated internal micrometers were used to obtain the spacing values. The spacing values were obtained by increasing the span of the internal micrometer until light touch contact between the ends of the micrometer was achieved with the sphere surface and the center

of the reference plate. The center of the reference plate corresponds to the center of the detector and this point had been permanently marked on the plate. These spacing measurements were made before and after each experiment. The consistency of the values was very satisfactory.

The tubular framework was then set into a support frame within the cadmium drum. The electrical connections were made and the drum sealed. Immediately a dry air purge of the drum was initiated. The purge consisted of forcing the dry air through the drum at a relatively high flow rate until approximately five volume changes had occurred. The dry air flow rate was then reduced such that a slow circulation continued for the entire time the detector was in the cadmium drum.

2. System Calibrations and Background Counting.

With the detector in the sealed cadmium drum, reverse bias was applied and leakage current monitored. A preliminary routine electronics check-out ensued using the precision pulse generator. This was followed by a formal system calibration using the pulser to obtain the relative pulse height spectrum, exposing the detector to an ^{241}Am alpha source to obtain normalization of the relative pulse height spectrum, and finally adjusting the T 101/N discriminator threshold. The upper and lower energy limits of detection of the system were defined by

pulsing at 60 Hz and using the ORTEC scalar in preset time mode to accumulate the counts being processed by the multichannel analyzer. Full efficiency was obtained from 0.72 MeV to 5.2 MeV. Equivalently, from an operational point of view, the scalar recorded 600 counts during a preset time interval of 10 sec while monitoring the counting procedure of the ADC for test pulse amplitudes corresponding to 0.72 MeV to 5.2 MeV, with the pulse amplitude to energy correspondence determined by the prior system calibration curve.

The no source background counts were taken during approximately 24 hour periods, spanning both day and night. This was necessary to gain assurance that no external noise sources were affecting the system.

3. Photon and Photoneutron Experiments.

Following activation of the source in the reactor core, the source was transferred via water lock to a hot cell adjacent to the reactor pool. In the hot cell the aluminum can containing the source was opened and the source placed in a heavy lead mobile cask for transfer to the docking port of the low scatter cave. With the detector bias turned off, a small triangular lid is removed from the cadmium drum. The cave is sealed and the activated source set into the source support ring using the simple vacuum manipulators. The procedure is viewed by the closed circuit television monitor. The lid of the cadmium drum is set into

place and sealed.

With the ^{241}Am alpha source prepositioned the pulse height spectrum is recorded. The test pulse generator is also used to obtain a relative pulse height spectrum. The detector bias is turned off and the source removed from the drum so that the cave may be entered to remove the ^{241}Am test source. With the ^{241}Am test source removed, the activated source is repositioned in the drum, the drum is sealed, bias applied and the relative pulse height spectrum again taken. The drum is then moved by the trolley to the center of the low scatter cave.

The data acquisition sequence is initiated (See Table 4.2), with system stability monitored on a regular basis. During the counting intervals the leakage current was observed for signs of instability, i.e., either oscillations or increase. Between data acquisition intervals, the multichannel analyzer record was printed out and the calibration rechecked using the pulse generator.

After completion of the data acquisition sequence, the system was formally recalibrated with and without the activated source in position.

These same calibration and system monitoring procedures were followed with both the photon and photoneutron sources. Following the photoneutron source run at

each spacing, the cadmium drum was opened to remove the tubular framework. The spacing measurements were again made and the detector returned to a dessicator for temporary shelf storage.

4. Manganese Bath Runs.

With the photoneutron source stored in the lead transfer cask, the manganese bath is filled, cleared of air pockets, and brought to thermal equilibrium. The recirculation flow rate is checked and the low scatter cave resealed. The manganese bath system electronics are then adjusted and background data acquired. The photoneutron source is then inserted into the bath for approximately 20 hours. Data is acquired before, during and after the source is in the bath.

The counting acquisition during the activation and decay cycle is completely automatic. The crystal base timer advances the multiscaler to the next channel after 600 sec to give a detailed history of the activity seen by the NaI crystal over the duration of the cycle. At the end of the cycle, the data is recorded on paper tape.

The bath calibration procedure was repeated using NBS-II starting approximately 36 hours after removal of the photoneutron source from the bath, corresponding to 14 ^{56}Mn half-lives.

5. Gamma Activity Comparisons.

The photon source was used to simulate all experimental conditions encountered during the primary data

acquisition runs using the photoneutron source. In particular, detector performance in the high gamma flux had to be simulated. The measurements of the gamma activity of the sources were intended to verify that equal gamma activity was achieved.

A Ge-Li detection system was set up in the photoneutron cave with a source holder at six feet from the head of the detector. The output from the Ge-Li system preamplifier was simply sent through a Hamner single delay line amplifier the output of which, in turn, could be processed by the multichannel analyzer. The system was calibrated using a small ^{60}Co source. The activity ratio of the photon and photoneutron sources was based on the ratio of count rates observed for the photopeak due to the 2.754 MeV ^{24}Na gamma. Correcting to the start time of the first data acquisition interval for each spacing experiment showed the gamma activity of the sources to differ by less than 5%.

CHAPTER IV

PRIMARY DATA - NEUTRON EVENTS

A. Preliminaries.

1. System Calibration.

Before and after each experiment the counting system was calibrated with and without the source (photon or photoneutron) in position. The pulse height spectra were normalized to the same absolute scale using the ORTEC pulser. The absolute energy calibration of this scale was determined using an ^{241}Am alpha source.

The gamma activity of the sources caused an increase in the FWHM of 10 percent and 50 percent for the ^{241}Am and pulser pulse height distributions, respectively, relative to the response for the no source cases. The cause of this phenomenon is thought to be a distortion of the electric field of the detector due to the high gamma induced electron production rate, estimated as 10^6 events per second. The gamma activity also caused small gain and zero offset shifts, observed as changes of the order of two percent in the calibration results obtained before and after each run. The counting system was fully efficient from 1.0 MeV to 5.1 MeV, as measured using the 60 cycle per second pulser. The lower energy limit was imposed by the need to assure linear pulse processing by the analog to

digital convertor in view of the high gamma event rate. The upper energy limit was selected to allow recording of all reaction products.

2. System Noise and Spurious Background.

Two noise sources affected the electronic system: 1) low energy system noise characterized by a uniform pulse height distribution and having a well defined upper limit; 2) low and high amplitude pulses caused by inductive and/or capacitive coupling of the system with the environment.

The system noise was monitored by long duration, no source background counting during preliminary system evaluation as well as prior to each of the four data acquisition sequences. The noise level extended to 0.82 MeV prior to the close spacing runs and to 0.72 MeV prior to the far spacing runs. This observed high noise level resulted from the absence of pulse shaping circuitry in the system (high or low pass filters) which would have reduced the high noise level from the detector itself. The high noise level of the detector was probably due to radiation damage, damage caused by handling or simply the result of performance deterioration caused by prolonged storage.

Because of the lack of high and low pass filters, the electronic system was very sensitive to external electronic interference causing, during preliminary system performance evaluations, a signal-to-noise ratio

near unity over the energy range of interest. This condition was corrected by the following measures: 1) single grounding and physical breaking of all possible ground loops; 2) complete electrostatic shielding using aluminum foil of the cadmium can containing the detector, of the SSR-1120 amplifier mounted on the outside of the cadmium can, of the junction box interfacing the amplifier, detector, bias supply and leakage current monitor, and of all coaxial cables. The only noise source which persisted in causing spurious events, although greatly reduced after implementing the aforementioned measures, was the room air conditioner. It was left off during the data acquisition periods.

Table 4.1 shows the results of the long duration background counts taken prior to each experiment, leading to a predicted signal to noise ratio of approximately 2000 for spurious events above the low energy system noise level for the cross section experiments.

Table 4.1.

Measured System Noise Level

and Spurious Background Counts

Experiment Number	Maximum Energy of System Noise, MeV	Spurious Counts Above System Noise	Background Count Duration, sec
I-A	.81	1	40000
I-B	.82	2	40000
II-A	.70	0	40000
II-B	.72	1	60000

3. Detector Performance.

As indicated in the above section, the noise level of the detector was high. In addition, during final preparation for the cross section measurements the leakage current was observed to be approximately twice the previously observed level of 0.1 μamp. Fluctuations in the leakage current were concomitantly observed, as well as resolution deterioration. The detector was returned to the manufacturer (ORTEC) for testing. The tests indicated a tendency toward microplasma breakdown when operated above 30 volts reverse bias, compared with its original rating of 40 volts. However, full depletion could be achieved in the 42μ depth at 14 volts. The cause of these instabilities appears to have been some damage to the electrode surfaces or deterioration of the dielectric properties of the epoxy cement used to hold the detector in its lavite ring.

Since instabilities were not observed at bias voltages below 30 volts, as confirmed by testing after return from ORTEC, we decided to proceed with the measurements applying approximately 20 volts bias during the actual experiments.

During the actual data acquisition runs, the bias was maintained between 16 and 20 volts. The leakage current was continuously monitored for oscillations or an abnormal increase, these being signs of incipient

instability. This phenomenon of increasing and fluctuating leakage current was observed only once during the four data acquisition runs. The data from that counting interval, I-B-4, was rejected. (See Section IV.B.3.) The situation was remedied by removing the photoneutron source from the cadmium can and allowing the detector to remain in the no source environment at a few volts bias for approximately 30 minutes. The photoneutron source was then repositioned in the experiment package, the calibration checked, and the counting sequence resumed with no further indication of instability. A minimum bias of 16 volts was maintained during the duration of the measurement.

The breakdown of the detector during counting interval I-B-4 was also evidenced by high amplitude, high rate pulses. The short data acquisition intervals, compared with the duration of the experiment, allowed subsequent statistical evaluation of the counts obtained during each interval. This evaluation is presented in Section IV.B.3.

4. Photon Background Subtraction Technique.

Figure 4.1 shows the lower quarter of a typical pulse height spectrum obtained using the photoneutron source. The neutron events extend up to about 4.2 MeV, and the photon tail ends at about 1.4 MeV. The detection system was intentionally set up to record

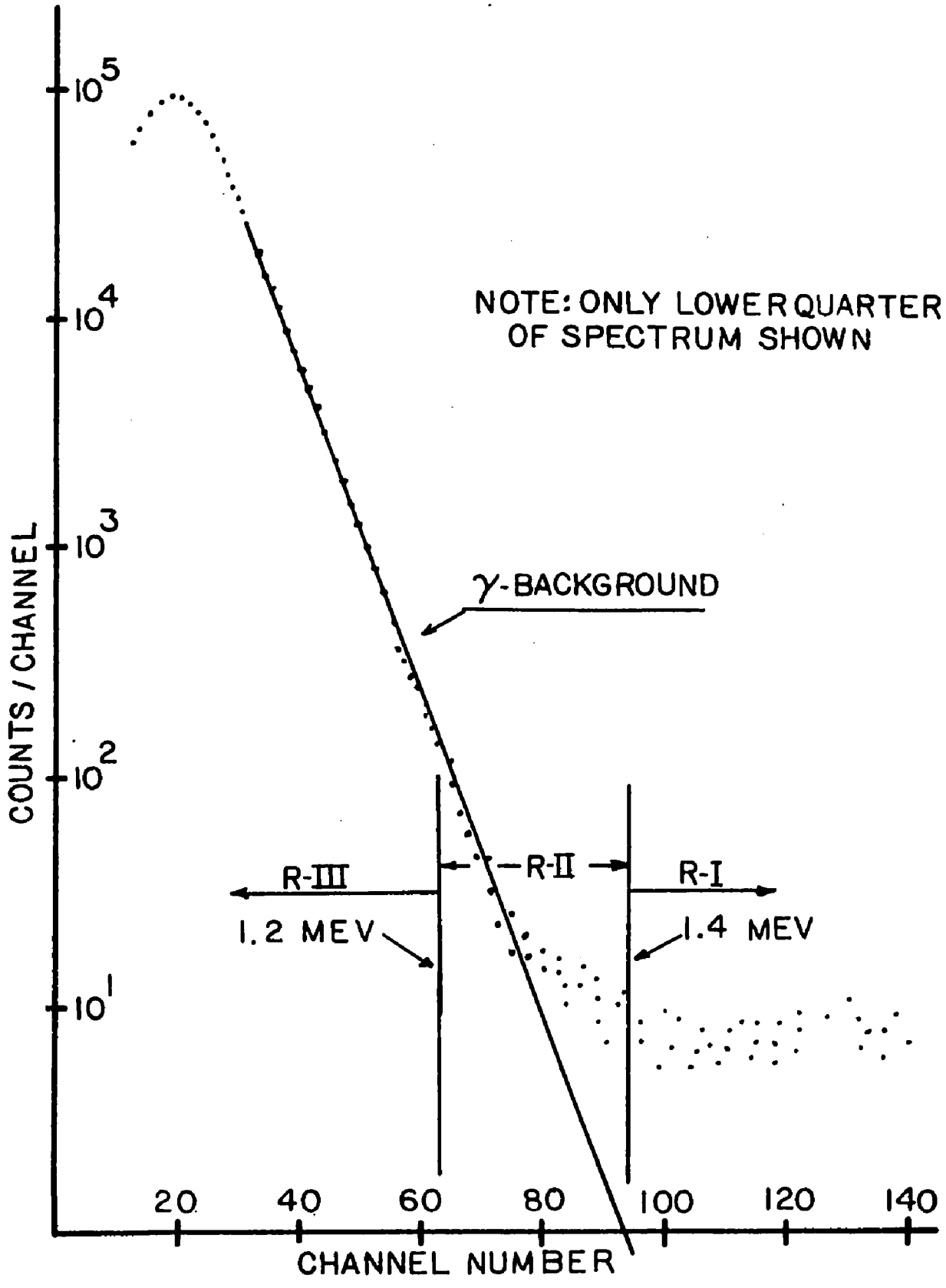


Figure 4.1. Typical Data from Photoneutron Source Run

the gamma response. For the purpose of data reduction, each pulse height spectrum was divided into three regions, labelled I, II and III in Figure 4.1. In Region I, there is no gamma background and all events are assumed to be neutron induced. In Region II, the photon response was subtracted from the photoneutron response as will be described later in this section. In Region III, the subtraction procedure is statistically meaningless and the number of neutron events was inferred using the measured response of the detector to a thermal neutron beam. For the case illustrated in Figure 4.1, the number of neutron events below 1.19 MeV was estimated by multiplying the total number of thermal neutron induced events below 1.19 MeV (obtained in the independent thermal beam response measurement) by the ratio of the total number of neutron events for the photoneutron source run above 1.19 MeV to the number of thermal neutron events in the same energy range. Differences in the observed and true event rate which are dependent on the degree of anisotropy of the reaction product yield as a function of neutron energy were not taken into account in the extrapolation.

To extract the neutron event data for Region II, paired photon-photoneutron data sets were used. A cubic spline fit (Gar, 68) was made to the pulse height spectrum obtained using the photoneutron source for

each data acquisition interval. The paired photon response data set, obtained using the equivalent photon source, was similarly smoothed using the cubic spline fitting code. The smoothed photon response was then normalized to the smoothed photoneutron response over a range of channels where the photon response is physically and statistically well defined and in which the neutron response is quantitatively insignificant. Referring to Figure 4.1, by channel 30 the photon response is well defined. The counting system is fully efficient inasmuch as the response is independent of threshold and zero offset settings. Between channels 30 and 50 the photon induced count rate is several orders of magnitude greater than the neutron induced event rate, which is therefore assumed to be negligible. The total number of events observed between channels 30 and 50 for the photoneutron source data set was then compared with the corresponding total obtained from the equivalent photon source data set. The ratio of the total number of counts in this channel range for the smoothed photoneutron data set to the same total obtained from the corresponding smoothed photon data set is defined as the count normalization factor, C_N. The smoothed photon response data was multiplied by this factor to obtain the corrected photon response for subtraction from the

corresponding photoneutron data set over the channel range of interest. The calculated difference, obtained by channel by channel subtraction, is the estimated neutron response in Region II.

This subtraction process could only be used until the photon response strongly dominated the neutron response, causing large statistical uncertainties in the remainder, due to subtracting one large number from another. The error in the remainder was taken as the square root of the sum of the individual terms in each subtraction. For the case illustrated in Figure 4.1, the process could only be extended down to 1.19 MeV.

B. Neutron Induced Events.

1. General Comments.

A synopsis of the data acquisition procedure is shown in Table 4.2 The gamma background runs using the equivalent activity photon source are labelled as the Photon Source Experiments in Table 4.2. Approximately 48 hours after completion of each gamma background run, the photoneutron source was used to obtain the primary data following a counting interval sequence facilitating direct set-by-set comparison of the primary and background data sets.

The start time of each counting interval was determined using the Michigan Bell time signal, the

	Photon Source Experiments			Photoneutron Source Experiments		
	Counting Interval Designation	Start Time, Time of Day	Duration, sec	Counting Interval Designation	Start Time, Time of Day	Duration, sec
Close Spacing Experiment	I-A-1	5/18 1400	8000	I-B-1	5/21 1328	8000
	-2	1645	|	-2	1605	|
	-3	1922	|	-3	1859	|
	-4	2246	|	-4	2135	|
	-5	5/19 0114	|	-5	5/22 0028	|
	-6	0354	|	-6	0301	|
	-7	0635	|	-7	0539	|
	-8	0921	|	-8	0906	|
	-9	1156	|	-9	1140	|
	-10	1426	8000	-10	1412	|
	---	----	----	-11	1650	8000
Far Spacing Experiment	II-A-1	6/1 1247	10000	II-B-1	6/4 1357	10000
	-2	1552	|	-2	1726	|
	-3	1852	10000	-3	2051	10000
	-4	2156	20000	-4	2355	20000
	-5	6/2 0350	|	-5	6/5 0550	|
	-6	1058	20000	-6	1156	|
	--	----	-----	-7	1816	20000

Table 4.2. Data Acquisition Sequence for the Cross Section Measurement

accuracy of which is verified daily against a standard time signal from the National Bureau of Standards. The error in the counting interval start times is negligible, of the order of ± one second. The duration of the counting intervals was obtained using the preset live time option on the multichannel analyzer. Since the maximum count rate was less than 350 counts per second, the 12 μsec maximum resolving time of the Nuclear Data-2200 multichannel analyzer leads to dead time corrections of less than 0.5%.

The counting interval durations were selected to afford good statistical definition of the events while also allowing for the possibility of anomolous detector performance without losing all the data from an experiment.

2. Neutron Events for Each Data Acquisition Interval.

Tables 4.3 and 4.4 show the number of neutron induced events associated with each data acquisition interval for each of the three previously described energy regions. Table 4.3 shows the results for the close spacing run and Table 4.4 shows the results for the far spacing run.

The fourth data set from the close spacing experiment (I-B-4) was not used in the tabulation because of obvious anomolous behavior as mentioned previously. (See Section IV.A.3.) The basis for elimination of the sixth data set from the far spacing run (II-B-6) will be discussed later.(See Section IV.B.3.)

Counting Interval	Start Time Actual	Start Time Relative, sec	Duration, sec	Primary Data Events R-I	R-II	R-III	Total
I-B-1	5/21 1328	0	8000	706 ± 27	92 ± 24	11 ± 11	809 ± 38
I-B-2	1605	9420		678 ± 26	70 ± 20	10 ± 10	759 ± 34
I-B-3	1859	19860		555 ± 24	61 ± 20	9 ± 9	625 ± 32
I-B-5	5/22 0028	39600		464 ± 22	64 ± 12	7 ± 7	535 ± 26
I-B-6	0301	48780		456 ± 21	36 ± 16	7 ± 7	499 ± 27
I-B-7	0539	58260		433 ± 21	36 ± 11	7 ± 7	475 ± 25
I-B-8	0906	70680		344 ± 19	25 ± 9	5 ± 5	375 ± 21
I-B-9	1140	79920		302 ± 17	22 ± 8	5 ± 5	329 ± 20
I-B-10	1412	89040		252 ± 16	12 ± 7	4 ± 4	268 ± 18
I-B-11	1650	98520	8000	210 ± 15	15 ± 6	3 ± 3	228 ± 16
Totals				4400 ± 66	434 ± 46	67 ± 67	4900 ± 105

Table 4.3. Primary Events From the Close Spacing Experiment

(1) R-I: Observed above Gamma Region
R-II: Calculated by Subtraction
R-III: Estimated from Thermal Beam Data

(2) Errors shown are one standard deviation except those of the thermal beam data which are defined as ± 100%.

Counting Interval	Start Time Actual	Start Time Relative, sec	Duration, sec	Primary Data Events R-I	R-II	R-III	Total
II-B-1	6/4 1357	0	10000	209 ± 15	36 ± 54	2 ± 2	247 ± 56
II-B-2	1726	12540	10000	198 ± 14	46 ± 17	2 ± 2	246 ± 22
II-B-3	2051	24840	10000	176 ± 13	51 ± 15	2 ± 2	228 ± 20
II-B-4	2355	35880	20000	286 ± 17	18 ± 17	3 ± 3	307 ± 24
II-B-5	6/5 0550	57180	20000	185 ± 14	20 ± 17	2 ± 2	206 ± 22
II-B-7	1816	101940	20000	97 ± 10	25 ± 10	1 ± 1	123 ± 14
Totals				1151 ± 34	195 ± 64	11 ± 11	1357 ± 73

Table 4.4. Primary Events for the Far Spacing Experiment

(1) R-I: Observed above Gamma Region
R-II: Calculated by Subtraction
R-III: Estimated from Thermal Beam Data

(2) Errors shown are one standard deviation except those of the thermal beam data which are defined as ± 100%.

The errors whown in Tables 4.3 and 4.4 for each counting interval were determined in view of the differences in the procedure used to obtain the number of neutron events in each of the separate energy ranges. In energy Region I (R-I), above the gamma region, the error was assumed to be the square root of the number of observed events. In energy Region II (R-II), in which the photon background subtraction procedure was used, the error was taken as the square root of the sum of the squared errors associated with each term in the subtraction. In energy Region III (R-III), where the system response to a thermal neutron beam was used to estimate the number of events, the error was arbitrarily defined as $\pm$ 100% of the inferred event number to account for differences in angular distribution. The errors for the total number of counts in each of the three energy ranges were obtained by taking the square root of the sum of the squares of the errors from each of the counting intervals. Finally, these totals by energy region were added to obtain the overall neutron event total for each experiment. The error in the total count was obtained by taking the square root of the sum of the squares of the errors for the three distinct energy ranges.

3. Statistical Evaluation of the Data.

To evaluate the reliability of the data obtained during each data acquisition segment, the following data

sets from each counting interval were compared with the most probable value of the mean:

a. the number of events above the gamma region - (R-I);

b. the number of events calculated by the subtraction procedure - (R-II);

c. the total number of events - (R-I + R-II + R-III).

To make this comparison, the time dependence of the observed count rate was eliminated by correcting for the decay of the ^{24}Na activity. For each counting interval, the number of counts equivalent to that obtained during the first counting interval of each experiment (close and far spacing runs) was obtained for each of the aforementioned data sets, a, b and c.

Let C_1 denote the number of counts associated with the first counting interval. Then C_1^i, the equivalent number of counts from the i^{th} counting interval is given by equation 4.B.1.

$$C_1^i = \left[\left(1 - e^{-\lambda \Delta t_1}\right) \left(1 - e^{-\lambda \Delta t_i}\right)^{-1} e^{\lambda t_i} \right] C_i \qquad 4.B.1$$

where,

C_i is the number of events associated with the i^{th} counting interval,

λ is the ^{24}Na decay constant,

t_i is the start time of the i^{th} counting interval relative to the start time of the first counting interval,

and,

$\Delta t_1, \Delta t_i$ are the durations of the respective counting intervals.

The error in C_1^i, $\sigma(C_1^i)$, was calculated using standard error propagation formulae, taking into account the uncertainties in the C_i's and in λ. The uncertainties in the C_i's were taken from Tables 4.4 and 4.5. The error in λ was obtained from the error in the ^{24}Na half-life, for which a value of 15.00 ± 0.03 hrs was used. (Mer, 71; Em, 72) $\sigma(C_1^i)$ was dominated by the error in C_i with $\sigma(\lambda)$ contributing less than one per cent to the calculated error in C_1^i.

The mean value for the C_1^i's was calculated by weighting each C_1^i inversely by its own variance as defined by equation 4.B.2.

$$\bar{C}_1 = \sum_i \left(C_1^i / \sigma^2(C_1^i) \right) \Big/ \sum_i \left(1/\sigma^2(C_1^i) \right) \qquad 4.B.2$$

The uncertainty in $\bar{C}_1$, $\sigma(\bar{C}_1)$, is given by equation 4.B.3.

$$\sigma^2(\bar{C}_1) = \left[\sum_i \left(1/\sigma^2(C_1^i) \right) \right]^{-1} \qquad 4.B.3$$

The numerical results are tabulated in Tables 4.5 and 4.6 for the close and far spacing runs, respectively. The close spacing run results are graphically compared with the mean in Figures 4.2 through 4.4. The far spacing run results are similarly compared with the mean in Figures 4.5 through 4.7.

Counting Interval Designation	Counts per Interval, Corrected to Time of First Interval		
	Above Gamma Region	Calculated by Subtraction	Total, Including Thermal Beam Extrapolation
I-B-1	706 ± 26.6	91.8 ± 24.1	808.8 ± 37.5
-2	765 ± 29.3	79.2 ± 22.2	856.0 ± 38.6
-3	716 ± 30.5	79.0 ± 26.1	806.1 ± 41.6
-5	771 ± 35.8	106.0 ± 19.6	889.0 ± 42.6
-6	853 ± 40.0	67.9 ± 29.2	934.0 ± 51.1
-7	915 ± 44.0	75.8 ± 23.7	1004.1 ± 51.8
-8	852 ± 45.9	62.9 ± 22.3	928.2 ± 52.6
-9	842 ± 48.6	61.4 ± 21.2	916.0 ± 54.4
-10	790 ± 49.9	37.6 ± 20.4	839.2 ± 55.2
-11	744 ± 51.4	53.1 ± 21.3	808.1 ± 56.7
Mean	775.6 ± 11.7	71.2 ± 7.1	870.4 ± 14.7

Table 4.5.

Number of Primary Events per Interval Compared with the Mean. Close Spacing Run

(Errors shown are one standard deviation)

Counting Interval Designation	Counts per Interval, Corrected to Time of First Interval		
	Above Gamma Region	Calculated by Subtraction	Total, Including Thermal Beam Extrapolation
II-B-1	209.0 ± 14.5	36.1 ± 53.7	247.1 ± 55.6
-2	232.6 ± 16.6	54.0 ± 20.0	289.0 ± 25.8
-3	242.1 ± 18.3	69.5 ± 20.6	314.2 ± 27.6
-4	241.2 ± 14.3	15.3 ± 14.6	258.6 ± 20.5
-5	205.1 ± 15.1	21.6 ± 19.1	228.6 ± 24.4
-7	191.0 ± 19.3	49.0 ± 18.9	242.0 ± 27.2
Mean	220.9 ± 6.5	37.5 ± 8.0	263.5 ± 10.8

Table 4.6.

Number of Primary Events per Interval Compared with the Mean. Far Spacing Run.

(Errors shown are one standard deviation)

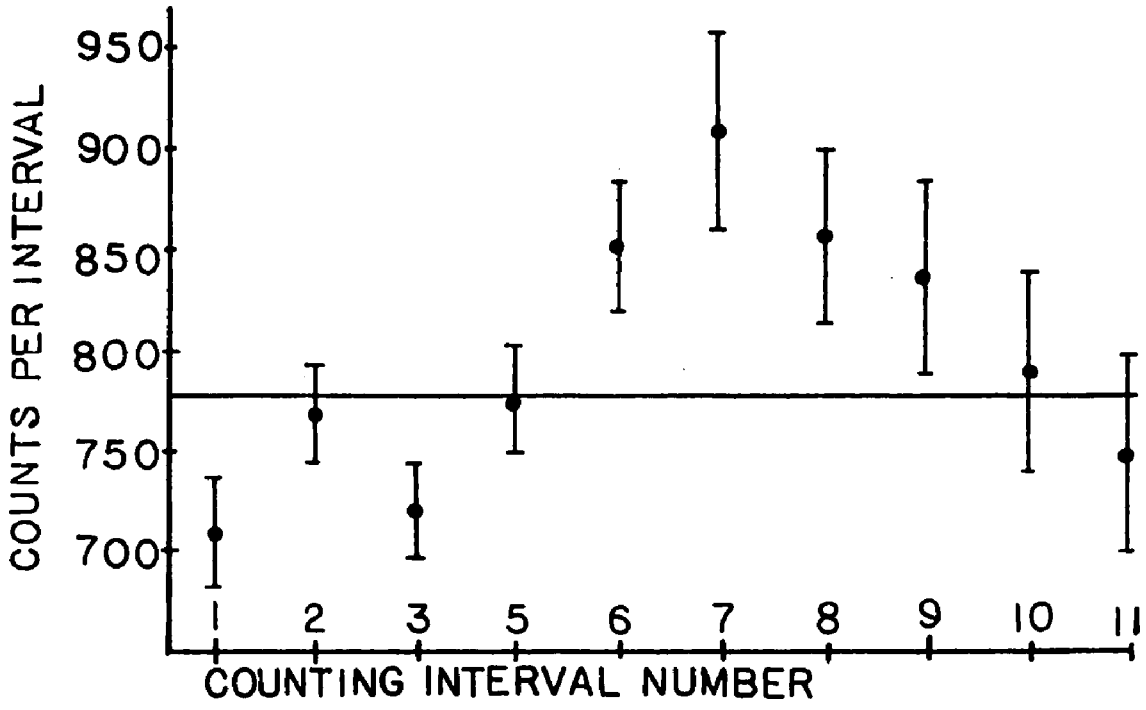


Figure 4.2. Primary Events per Interval above Gamma Region Compared with the Mean--Close Spacing Run

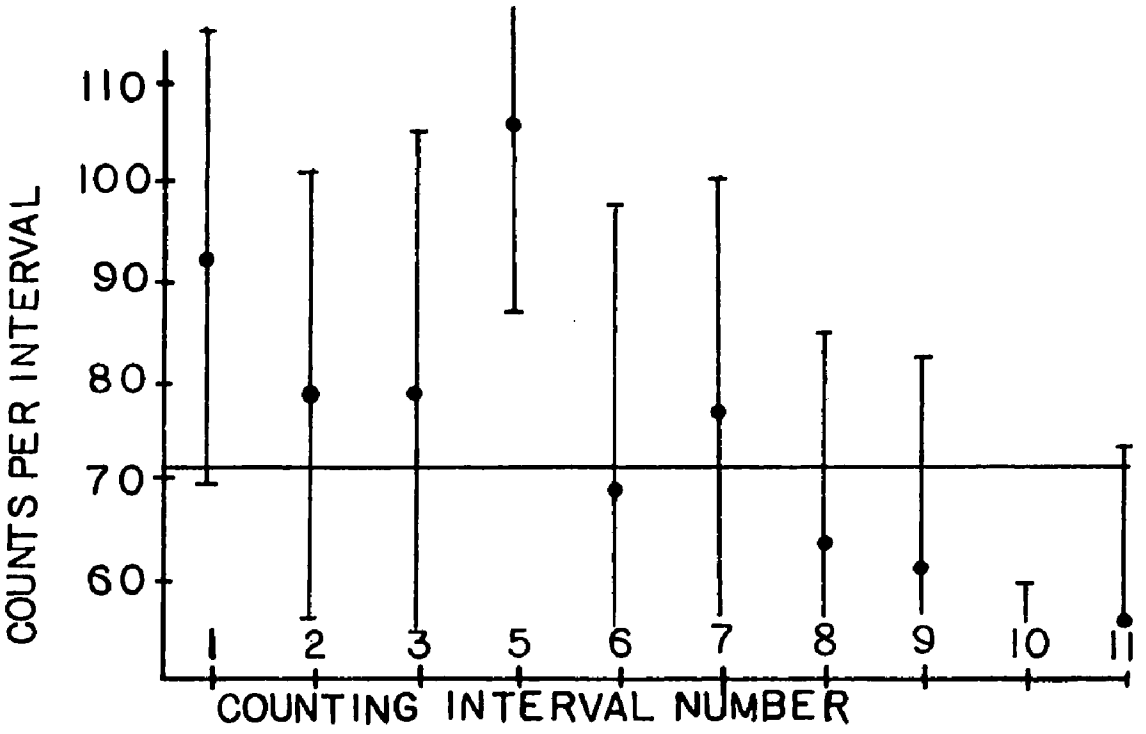


Figure 4.3. Primary Events per Interval Obtained by Gamma Background Subtraction Compared wt.Mean--Close Spacing Run

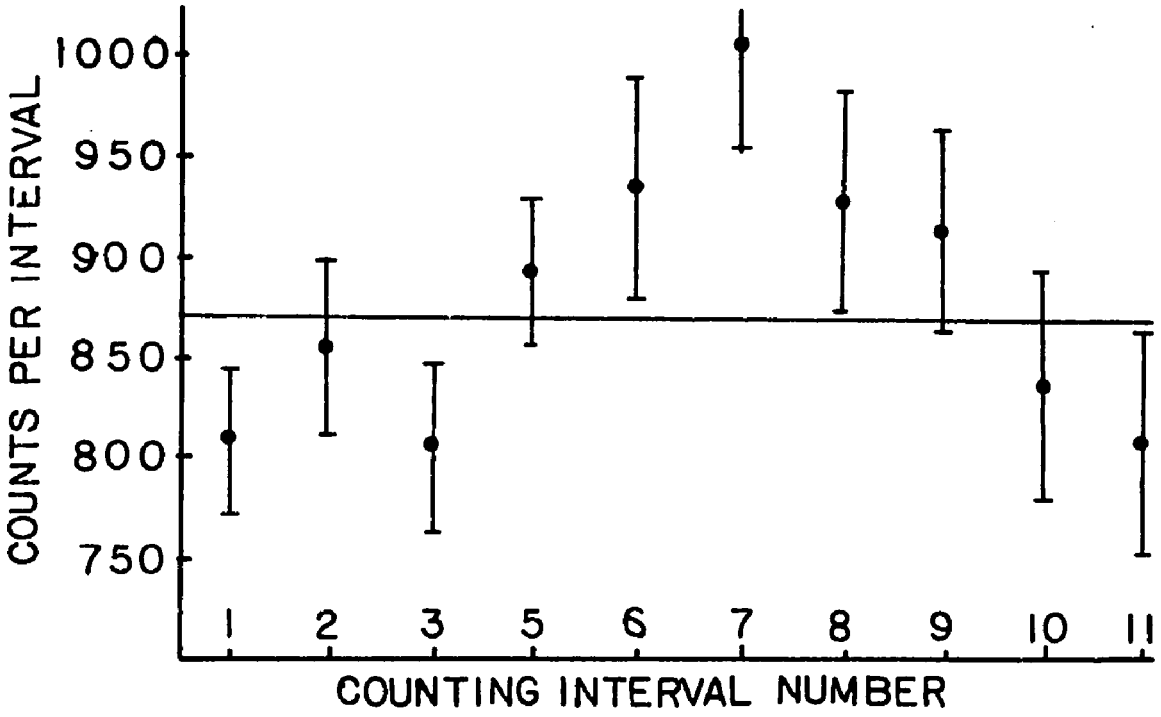


Figure 4.4. Total Number of Primary Events per Interval Compared with the Mean--Close Spacing Run

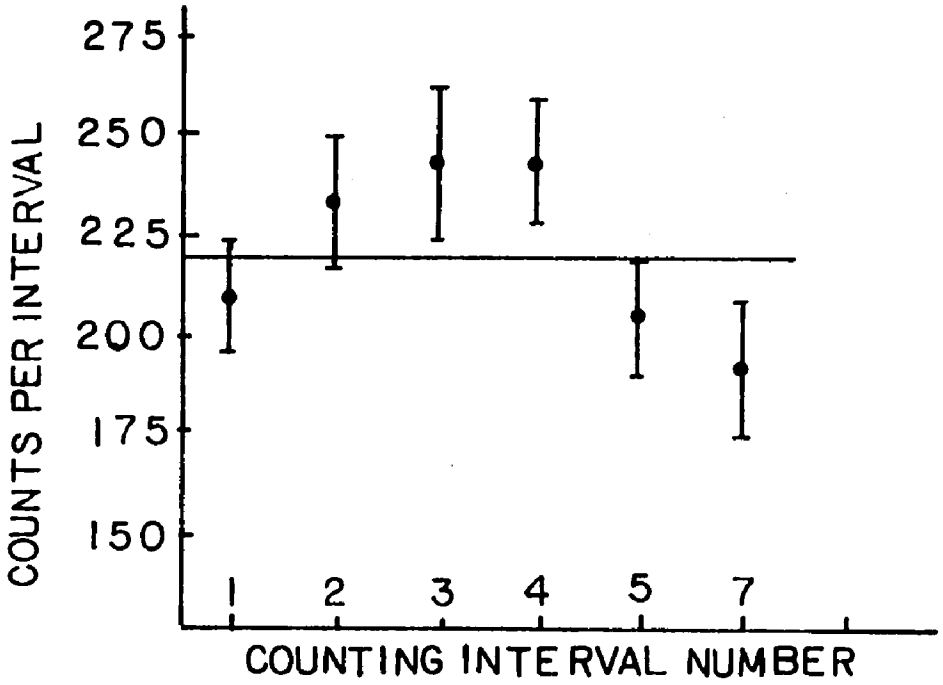


Figure 4.5. Primary Events per Interval above Gamma Region Compared with the Mean--Far Spacing Run

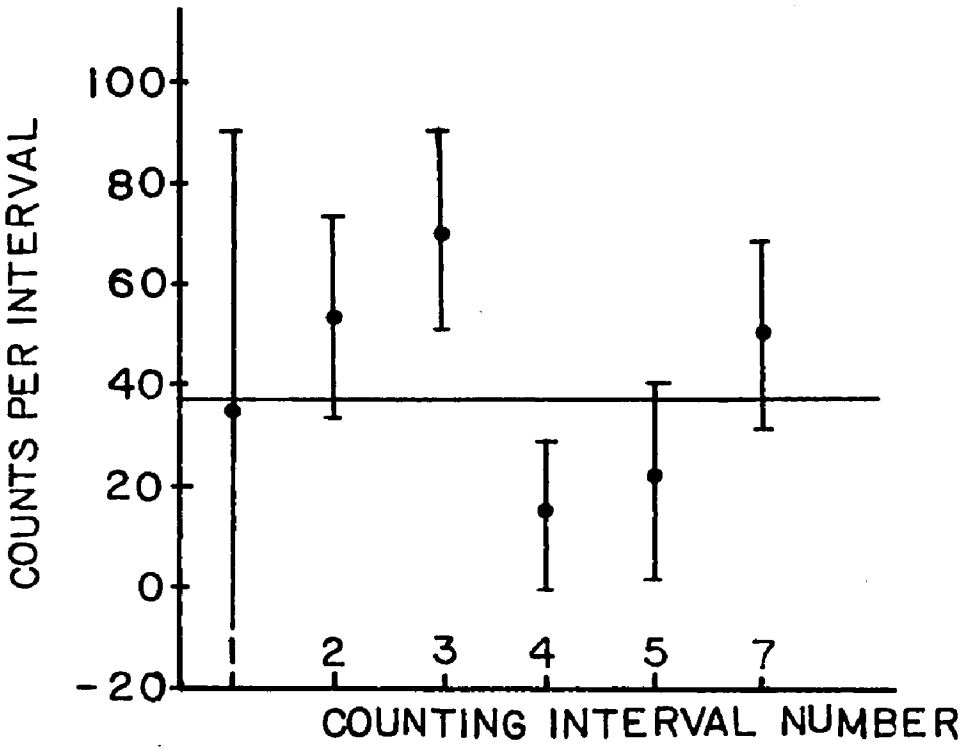


Figure 4.6. Primary Events per Interval Obtained by Gamma Background Subtraction Compared wt.Mean--Far Spacing Run

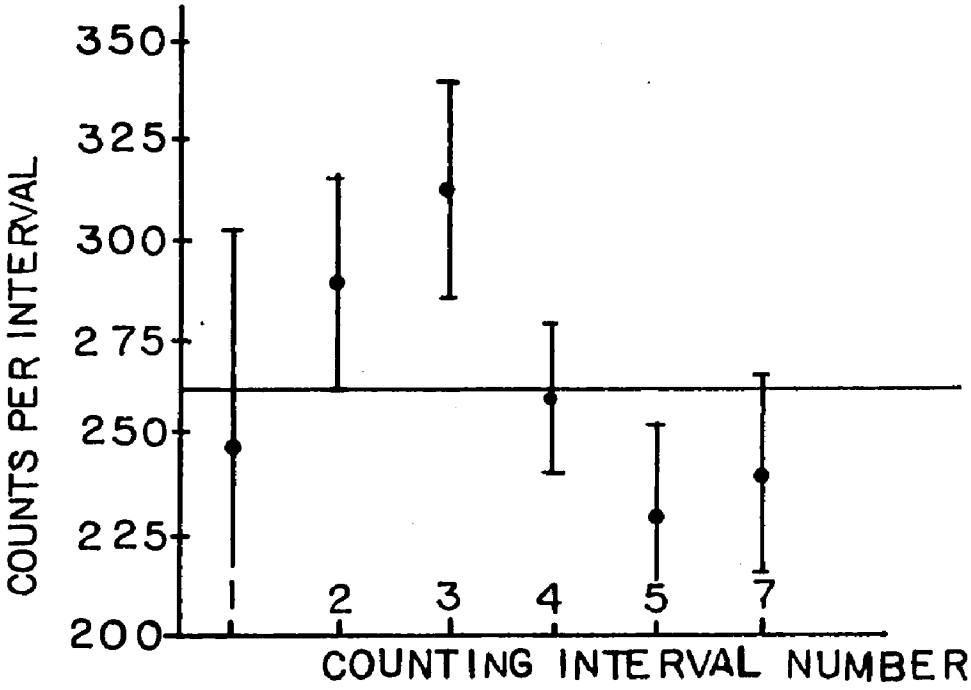


Figure 4.7. Total Number of Primary Events per Interval Compared with the Mean--Far Spacing Run

These plots allow observation of systematic trends in the data and are used as a check on the consistency of the distribution of the values about the mean with the standard statistical criterion, namely that 67 per cent of the values should be within one standard deviation of the mean.

As far as the close spacing run is concerned, the analysis does not include the data from counting interval I-B-4 because of the obvious anamolous behavior of the detector. In addition, this statistical analysis indicate a possible trend in the data, with the equivalent count from interval I-B-7 being 2.6 standard deviation greater than the mean, corresponding to a probability of occurrence of approximately one per cent. The data for the total number of events for the close spacing run excluding counting interval I-B-7 is graphically compared with the mean in Figure 4.8. The results from the close spacing run are consistent with the 67 per cent criterion if the data from interval I-B-7 are rejected. This question of a possible systematic error in the results will be incorporated into the final cross section evaluation by calculating the cross section including and excluding the results from counting interval I-B-7.

As regards the data from the far spacing experiment, the results are statistically acceptable applying the 67 per cent criterion and no trends are evident after excluding the results from counting interval II-B-6.

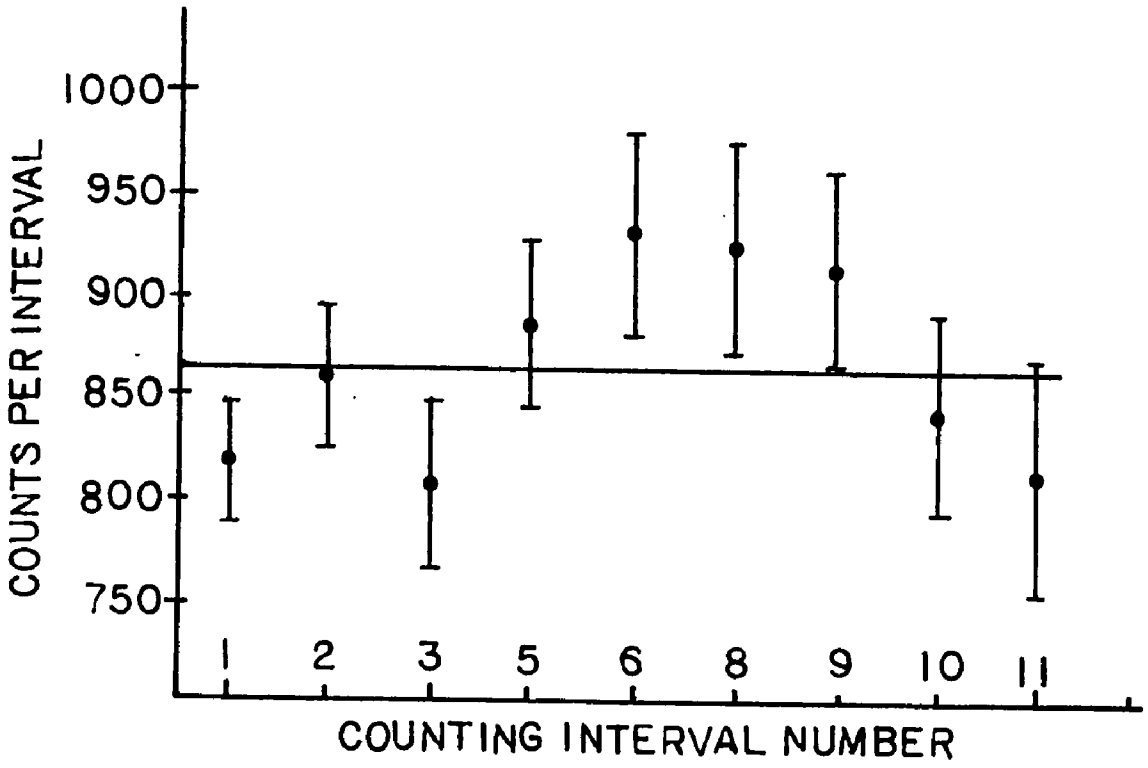


Figure 4.8. Total Number of Primary Events per Interval Compared with the Mean, Excluding I-B-7--Close Spacing Run

This data set was excluded since the number of neutron events in energy Region II, obtained by the photon background subtraction procedure, exceeded the calculated mean for this data subset by approximately five standard deviations. There was no physical evidence for anomolous detector performance during this run and the number of events from energy Region I, above the gamma region, were consistent with the data obtained from the other data acquisistion intervals. The probable cause of this unusually high count is detector instability. However, since there were no high rate - high amplitude pulses concomitantly observed, as during counting interval I-B-4, some doubt remains concerning this conclusion.

The primary count values used in evaluating the cross section are summarized in Table 4.7.

Table 4.7.

Primary Counts Used for Cross Section Evaluation

Experiment	Reason for Exclusion of Data Set(s)	Primary Count with Designated Data Set(s) Excluded
Close Spacing: excluding		
1) I-B-4	Detector Breakdown	4900
2) I-B-4 & I-B-7	Statistical	4425
Far Spacing: excluding		
II-B-6	Statistical	1357

CHAPTER V

SECONDARY DATA

A. Neutron Activity Determination.

1. Saturated Count Rates.

The basic parameter used in determining the neutron activity of a source by the manganese bath technique is the saturated ^{56}Mn count rate. In our use of the bath as a source comparator the calculated ^{56}Mn saturated count rate of the Na-Be photoneutron source was compared with the ^{56}Mn saturated count rate obtained in the bath using NBS-II. The details of this technique have been thoroughly discussed by Gilliam (Gil, 73; Gil, 75) and only the major points will be discussed here.

The observed ^{56}Mn activity, recorded in multi-scaling mode in 600 sec intervals, is converted to a saturated activity value referred to the time of source insertion into the bath. This was done using the code SAT2 which corrected for the decay of the neutron activity of the source, activation and decay of the ^{56}Mn, detector background, counting system deadtime and mixing delays. (Gil, 73) The saturated count rates obtained for the four bath runs to determine the neutron activity of the photoneutron source are shown in Table 5.1.

Table 5.1.

Saturated Count Rates for

Activity Determination

Neutron Source	Saturated Count Rate, Counts / sec	Saturated Count Rate Ratio, Na-Be / NBS-II
Na-Be (1)	1090.25 ± 0.14	3.783 ± 0.08%
NBS-II	288.19 ± 0.07	
Na-Be (2)	726.97 ± 0.15	2.522 ± 0.08%
NBS-II	288.23 ± 0.07	

(1) Immediately following close spacing experiment.

(2) Immediately following far spacing experiment.

The errors shown are the quadrature sum of the uncertainties in the aforementioned corrections applied to the observed count rate data to obtain the saturated count rates.

2. Integrated Neutron Activities.

a. General Comments. Since the saturated count rate is proportional to the neutron activity of the source in the bath, the ratio of the saturated count rates for two different sources is equal to the ratio of their neutron activities, after corrections are made to eliminate source dependent differences. These corrections take into account differences in parasitic absorption, neutron leakage and photoneutron production due to the deuterium content of the aqueous manganous

sulfate solution. These effects have been quantitatively determined by Gilliam in the cited references and his results are shown below.

b. Parasitic Absorption Correction. The parasitic absorption correction accounts for differences in the neutron field within the bath due to different neutron absorption characteristics of the sources and different values for the resultant energy dependent neutron flux at the source position. Based on thermal flux measurements made in the dry well of the bath, the parasitic absorption effect for NBS-II was calculated to be 0.63% greater than for the Na-Be source.

c. Neutron Leakage Correction. Neutrons can escape from the bath by streaming from the dry well or by bulk penetration. The leakage due to streaming was calculated by Gilliam taking into account both direct streaming from the source as well as streaming of slow neutrons returning to the cavity. An upper bound on bulk penetration escape of the Na-Be neutrons was determined to be 0.34%, whereas bulk penetration leakage for the lower energy Ra-γ-Be neutrons from NBS-II is negligible. The net result is that the neutron leakage from the bath is 0.16% greater for the Na-Be source than for NBS-II.

d. Deuterium Photoneutron Correction. The effect of photoneutron production due to the deuterium

content of the bath solution was determined by direct measurement using a ^{24}Na source similar in activity and configuration to the Na-Be photoneutron source, but having no beryllium shell. This measurement determined that 0.94% of the ^{56}Mn count rate obtained with the Na-Be source is due to deuterium photoneutrons. Consideration of the gamma intensities and spectrum of the Ra-γ-Be standard source leads to the conclusion that the deuterium photoneutron effect for NBS-II is about 100 times smaller than for the Na-Be photoneutron source. (Gil, 73)

In summary, the ratio of the ^{56}Mn saturated count rates is related to the ratio of the neutron activities of the Na-Be photoneutron source and NBS-II by Equation 5.A.1:

$$\frac{A^{NA\text{-}BE}}{A^{NBS\text{-}II}} = F_{PA} F_L F_D \frac{C_\infty^{NA\text{-}BE}}{C_\infty^{NBS\text{-}II}} \qquad 5.A.1$$

where,

A denotes the true neutron activity,

C_∞ denotes the saturated count rate, and

F_{PA}, F_L and F_D are the parasitic absorption, leakage and deuterium photoneutron production correction factors, respectively.

e. Source Yield Evaluation. A value of $1.174 \times 10^{+6}$ sec^{-1} ± 0.5% as of June, 1973, was used for the neutron activity of NBS-II to

evaluate Equation 5.A.1, based on Gilliam's evaluation of independent calibrations reported by four laboratories: the National Bureau of Standards (Noy, 63; Spi, 72), the International Bureau of Weights and Measures (Huy, 70), the National Physical Laboratory (Ax, 65), and Argonne National Laboratory (DeV, 69).

The values of the correction factors and the neutron activity of the Na-Be source referred to the time of insertion into the manganese bath, as well as the associated errors, are summarized in Table 5.2.

Table 5.2.

Bath Correction Factors and

Neutron Activity of the Na-Be Source

Term	Value	Residual Uncertainty
Parasitic Absorption	0.9937	0.36%
Neutron Leakage	1.0016	0.18%
Deuterium Photo-neutron Production	0.9906	0.10%
Neutron Activity of Na-Be Source	I - $4.381 \times 10^6 sec^{-1}$	0.65%
	II - $2.921 \times 10^6 sec^{-1}$	0.65%

The 0.65% error shown for the neutron activity values includes, in addition to the stated errors in the correction factors, the errors in the saturated count rate ratios from Table 5.1 and the 0.5% uncertainty

in the value of the neutron activity of NBS-II.

To obtain the integrated neutron activity of the Na-Be source during the counting time of an experiment, the source activity values shown in Table 5.2 were corrected to the time of initiation of the first counting interval for the corresponding experiment (close or far spacing run). Then the integrated neutron activity was obtained by integration, using the start time and counting interval durations shown in Table 4.2. The errors calculated for the initial and integrated neutron activities include the effects of the $\pm$0.65% error from the manganese bath activity determination and $\pm$0.2% uncertainty due to the ^{24}Na decay constant. These results are summarized in Table 5.3.

Table 5.3.

Initial and Integrated Source

Neutron Activities

Case	Neutron Activity at Start of First Counting Interval, sec^{-1}	Integrated Neutron Activity
I (Close Spacing)		
exc.I-B-4	$3.510 \times 10^{7} \pm 0.77\%$	$1.504 \times 10^{12} \pm 0.88\%$
exc.I-B-4 & I-B-7	$3.510 \times 10^{7} \pm 0.77\%$	$1.377 \times 10^{12} \pm 0.85\%$
II (Far Spacing)		
exc.II-B-6	$3.607 \times 10^{7} \pm 0.82\%$	$1.752 \times 10^{12} \pm 0.92\%$

B. Mean Scalar Fluence.

1. General Comments.

Having determined the number of source neutrons generated during each experiment, the number of these intercepting the target deposit must be defined. Using the measured source-target spacing, the point source-point target model enables calculation of the neutron current at the target. This result is obtained, then corrections for the spatial distribution of the source and target are incorporated to obtain an approximation to the mean scalar fluence. Finally, the errors contributed by the effects of the anisotropy of the source neutron yield are shown to be negligible.

2. Source-Target Spacing.

a. General Comments. The source-target spacing is inferred from several measurements. The following distances were measured: the distance from the surface of a precision chrome sphere to the surface of a reference plate attached to the detector mount, after the detector mount had been rigidly secured in position in the tubular support frame; the thickness of the reference plate; and the distance from the reference plate to the near target surface. Corrections for differences in radii between the chrome sphere and the Na-Be source as well as for the thickness of the target - detector composite and off-centeredness of the deposits

relative to the detector mount were evaluated and found to be less than 0.4%.

b. Source - Reference Plate Spacing. Preliminary alignment of the detector relative to the source was accomplished using a positioning jig. The tubular support frame rested on a steel flat during the alignment and spacing measurements. The detector mount was suspended on the triangular arms of the support frame, the positioning jig placed in position and the detector mount moved into alignment with its outline which had been marked on the surface of the jig. The detector mount was then rigidly fixed in this position and the alignment rechecked before removal of the positioning jig. The aluminum reference plate was then secured on the detector mount, the chrome sphere placed in the source support ring and the minimum distance between the surface of the sphere and of the reference plate measured.

These measurements were made using a set of calibrated internal micrometers. The separation was measured three times before and after each experiment. The results are shown in Table 5.4. The error in the measurements, based on the repeatability shown in Table 5.4, is $\pm$ 0.001 inches. For each spacing, the average of the before and after measured values was taken as the actual distance.

Table 5.4.

Measured Reference Sphere to Plate Distances for Close and Far Spacing Experiments

Condition		Reference Sphere to Plate Distances, in.			
		1	2	3	Average
I	Before	2.6570	2.6580	2.6570	2.6573
	After	2.6550	2.6545	2.6555	2.6550
II	Before	7.0280	7.0270	7.0275	7.0275
	After	7.0275	7.0271	7.0270	7.0272

To obtain the source center to reference plate distances, the radius of the reference sphere (0.701 in. $\pm$ 0.0002 in.) was added to the above values, giving a source center to plate spacings of 3.3572 in. and 7.7284 in. for the respective cases to an accuracy of $\pm$ .001 in.

c. Reference Plate Thickness. The thickness of the reference plate was determined to be .049 in. $\pm$ .0005 in. This result was obtained using a standard micrometer, the accuracy of which was checked using Johannsen gage blocks. This value was confirmed later using the calibrated optical microscope set up to measure the target surface to plate surface distance.

d. Target Surface to Reference Plate Distance. The detector mount, with the detector secured in place,

was placed on the moveable stage of a Unitron TM - 1456 optical microscope. The (x, y) position of the cross hairs on the lense was read from vernier dials as the stage was moved in the horizontal plane. A dial gage was mounted on the microcope such that the vertical distance moved to focus on parts of the detector mount in different horizontal planes could be read directly from the gage. The dial gage and (x, y) - verniers were calibrated using Johannsen gage blocks. The measurements made using this system were reproducible to $\pm$ 0.2%.

This calibrated optical microscope system was used for all measurements related to determining component positions and extent, including the target diameter measurements discussed in Section V.C and the physical extent of the epoxy fillet which holds the silicon detector itself to its insulating lavite ring discussed in Section VI.B. The results relevant here are the distance from the target surface to the aluminum plate and measurement to determine the deviation from perfect alignment of the target deposits relative to the detector mount.

Figure 5.1 shows a schematic cross-section of the detector mount.

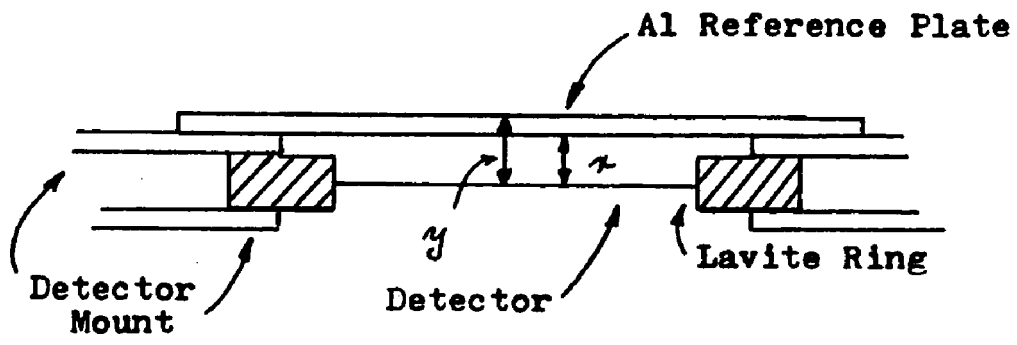


Figure 5.1.
Schematic Cross - Section of
Detector and Mount

First, the detector mount was placed on the moveable stage of the microscope without the reference plate attached, enabling measurement of distance from the near target surface to the corresponding surface of the detector mount to which the plate is secured for the source position measurements. This distance is denoted by "x" in Figure 5.1. The aluminum reference plate was then secured to the detector mount and the distance from the target surface to the reference plate surface, denoted by "y" in Figure 5.1, was determined by subtracting the dial gage reading obtained when focused on the target surface from the reading when focused on the reference plate surface. These results were consistent with the directly measured reference plate thickness. The results are shown in Table 5.5. The actual distance from the target surface to the outer surface of the

reference plate was directly measured to avoid inferring this value from the plate thickness value itself. The error in the source center to target surface distance is the sum in quadrature of the errors of the contributing terms.

Table 5.5.

Source Center to Target Surface

Spacing Results

Distance	Value, in.	Error as % of Value
Target Surface to Detector Mount, "x"	.090	± 0.3
Target Surface to Reference Plate Surface, "y"	.139	± 0.36
Reference Sphere Surface to Reference Plate	I - 3.3572	± 0.03
	II - 7.7284	± 0.001
Source Center to Target Surface	I - 3.496	± 0.36
	II - 7.867	± 0.36

e. Corrections to the Source - Target Spacing Values. The determination of the position of the target relative to the source assumes that the target deposits are centered with respect to the circular opening of the detector mount. Measurements using the optical microscope showed both targets to be off center by 0.2 cm. This implies a .025% increase in the source

center to target surface distance for the close spacing case and a 0.005% increase for the far spacing case. The error in this correction is considered negligible.

The final correction to the distance accounts for the thickness of the target deposits, electrode deposits and of the silicon detector itself. Data on the Si and electrode thicknesses come from the ORTEC data sheet for the detector. The target deposit thicknesses, obtained by electron microscope analysis of the deposits on the monitor foils (See Section V.C) is approximately 7200 Å. The center of the source - detector composite was estimated to be 0.002 cm from the surface of the target deposit on the aluminum electrode, to which surface the previous measurements were referred. No error is included in this term.

Table 5.6 summarizes the results and associated errors for the source - target spacing determination.

Table 5.6. Summary of Source-Target Spacing Results.

Term	Value, cm	Estimated Error in Source - Target Spacing, %
Deposit Asymmetry	I - + .002 II - + .001	------ ------
Detector - Target Composite Thickness	+ .002	------
Source Center - Target	I - 8.884 II - 19.986	± 0.36 ± 0.36

3. Neutron Current per Unit Source Strength.

a. General Comments. The expression $1/4\pi d^2$, where d is the source - target spacing obtained in the preceding section, can be used as a first approximation to the current per unit source strength. An analytic model representing the distributed source and target is used in conjunction with the point source - point target representation, i.e. $1/4\pi d^2$, to obtain a better approximation to the current per unit source strength.

b. Source - Target Spatial Distribution. The physical data required to represent the Na-Be photoneutron source were taken from the manufacturer's (Monsanto Research Corporation) data sheets, incorporating our own measurements of the source diameter.

Equation 5.B.1 was used to evaluate the distributed source effect. The neutron current at a point R_0 due to a uniformly - emitting shell having inner radius "a" and outer radius "b" is given by equation 5.B.1

$$J_{DS}(R_o) = \frac{A_N}{4R_oV}\left[(r^2 - R_o^2) \ln\left(\frac{R_o+r}{R_o-r}\right) + 2R_o r \right]_{r=a}^{r=b} \qquad 5.B.1.$$

where,

A_n is the neutron activity of the source,

V is the neutron generating volume, and

R_0 is the distance from the center of the shell to the point where the current is being calculated.

Equation 5.B.2 was used to account for the spatial distribution of the target. The neutron current for a disk target with radius R_T and area A_T at a distance R_0 from a point neutron source is given by equation 5.B.2.

$$J_{DT}(R_o) = \frac{A_N}{4A_T}\left[\ln\left(R_o^2 + R_T^2\right) - \ln R_o^2\right] \qquad 5.B.2.$$

To represent the Na-Be source, the results of the Monte Carlo neutron spectrum calculation performed by Ryves and Robertson were incorporated. (Ryv, 71). This calculation predicted that 70.35% of the neutron yield from the source is unscattered. Consequently, the remaining 29.65% of the neutron yield is scattered. It was assumed that this scattered component comes from the NaF sphere and Be shell in proportion to the macroscopic scattering cross sections of these components, leading to the result that 53.9% of the scattered component comes from the Be shell and 46.1% comes from the NaF sphere. The current from the Na-Be photoneutron source at R_0 is then represented by equation 5.B.3.

$$J_{DS}(R_o)\Big|_{\substack{\text{NA-BE}\\\text{SOURCE}}} = A_N\left\{.7035G(a, b, R_o) + .2965\left[.5390\right.\right.$$
$$\left.\left.G(a, b, R_o) + .4610G(0, r_c, R_o)\right]\right\} \qquad 5.B.3.$$

Where $G(a, b, R_0)$ and $G(0, r_c, R_0)$ are the current per unit source strength at R_0 due to the shell and inner sphere, respectively, as given by equations 5.B.4 and 5.B.5.

$$G(a, b; R_o) = J_{DS}(R_o)/A_N \Big|_a^b \qquad 5.B.4.$$

$$G(0, r_c, R_o) = J_{DS}(R_o)/A_N \Big|_o^{r_c} \qquad 5.B.5.$$

and where r_c is the radius of the NaF sphere.

The following procedure was used to obtain a superposition of the distributed source and distributed target representations. Let J' represent the current per unit source obtained by dividing equations 5.B.2 and 5.B.3 by A_n. Let $J_0'(R_0) = 1/4\pi R_0^2$, the current per unit source strength from the point source - point target representation. Then, the current per unit source strength $J'(R_0)$ is obtained from equation 5.B.6.

$$J'(R_o) = J'_{DS}(R_o)\Big|_{\substack{\text{NA-BE}\\ \text{SOURCE}}} \left(J'_{DT}(R_o)/J'_o(R_o) \right) \qquad 5.B.6$$

The numerical results obtained for the close and far spacing experiments are shown in Table 5.7.

Table 5.7

Results for Determining $J'(R_0)$

R_0, cm	Current per Unit Source Strength, Neutrons / cm^2 - Source Neutron			
	$J'_{DS}(R_0)\Big\|_{\text{Source}}^{\text{Na-Be}}$	$J'_{DT}(R_0)$	$J'_0(R_0)$	$J'(R_0)$
I- 8.884	1.0198E-3	1.0065E-3	1.0086E-3	1.0176E-3
II-19.986	1.9967E-3	1.9915E-3	1.9924E-3	1.9958E-3

The accuracy of this model was tested by comparison of results obtained from it with a neutron streaming calculation of the current at a disk target, then directly calculating the scalar flux by angular integration over the distributed target. This calculation included the effects of the anisotropy of the neutron emission from the Na-Be source, which are ignored in the present model. (Gil, 73) The results agreed to within 0.1% and 0.03% for source - target spacings of approximately 5 cm and 9 cm, respectively.

The results of this calculation of the current per unit source strength implicitly include the effective target thickness term. For purposes of evaluating the reaction rate in the target these results are equivalent to the results obtained by transport streaming calculations of the mean scalar flux at the target.

The error in the current per unit source strength is combined from two sources: first, the error in the method itself which is taken as $\pm$ 0.1% based on the preceding comparison with the results of Gilliam; secondly, the error in the current due to the uncertainty in the source - target spacing given in Table 5.5 as $\pm$ 0.36%. If Δr is the error in the spacing, the resulting error in the current is $2\Delta r/R_0$ where R_0 is the measured value. This then, contributes

0.72% uncertainty to the current, with the final error in the current per unit source strength being the quadrature sum of these two error terms, viz., ± 0.73%.

The mean scalar fluence is calculated by combining the integrated neutron activity and the current per unit source strength for each experiment. These results are shown in Table 5.8.

The errors in the intermediate parameters shown in Table 5.8 are combined in quadrature to obtain the errors associated with the mean scalar fluence. Again, as in Table 5.3, the case of the close spacing experiment excluding data set I-B-7 is included for later error analysis.

C. Number of Target Nuclei.

1. General Comments.

The number of target nuclei in each target deposit was determined in the following manner. First, the mass thickness of ^{6}LiF on three monitor foils symmetrically placed around the detector during vapor deposition of each target deposit was obtained by weighing the foils before and after the deposition process, thus obtaining the weight gain. From the known monitor foil deposit areas, a ^{6}LiF mass thickness was obtained. This mass thickness was geometrically corrected to

Experiment	Integrated Neutron Activity	Current per Unit Source Strength, Neutrons / cm^2- Source Neutron	Mean Scalar Fluence, Neutrons / cm^2
I: including I-B-7	1.504E+12 ± 0.88%	1.0176E-3 ± 0.73%	1.53E+9 ± 1.14%
excluding I-B-7	1.377E+12 ± 0.85%	1.0176E-3 ± 0.73%	1.40E+9 ± 1.12%
II: ———	1.752E+12 ± 0.92%	1.9958E-3 ± 0.73%	3.50E+8 ± 1.17%

Table 5.8.

Mean Scalar Fluence and Intermediate Values

for the Close and Far Spacing Experiments

obtain that of the target deposits themselves. Next, the target areas were carefully measured. Using this information and the results of a mass spectrographic analysis of the monitor foils, enables calculation of the number of ^{6}Li nuclei in each deposit. These procedures and results will be described.

2. Monitor Foil Deposit Mass Thickness.

The vapor deposition was done by the Isotope Target Laboratory at ORNL. The masked detector was eight inches from the ^{6}LiF source. Three aluminum foils were symmetrically placed on a flat surface around the detector during the vapor depositions. The distance from the center of the detector to the center of the monitor foils was one inch. Since the mass thickness of the deposits is inversely proportional to the square of their mean distance from the ^{6}LiF vaporization source, the mass thickness of the target deposits will be greater than that of the mass thickness of the monitor foil deposits by 1.56%. This correction is based on a point vaporization source model and the assumption that vacuum streaming is the dominant mode of molecular transfer. The applicability of these assumptions was verified by Kobisk. (Kob, 75) The data on the weight gain of the monitor foils is shown in Table 5.9.

Table 5.9.

Weight Gain of Monitor Foils

Reported by ORNL

Monitor Foil Number	Electrode Surface of Detector	Mass Gain, μgms	Monitor Foil Area, cm^2
1	Al	507	2.874
2	Al	490	2.841
3	Al	486	2.850
4	Au	510	2.847
5	Au	490	2.847
6	Au	509	---

The weight gain of each of the three monitor foils associated with each target deposition, (i.e., on aluminum and on the gold electrode surface of the detector) were averaged to obtain the values shown in Table 5.10 for the mass thickness of the foils. A variance of $\pm$ 3 μgms was assigned to these values based on reproducibility of microbalance weighings made on the foils at the University of Michigan.

The monitor foil deposit diameters were measured using the calibrated optical microscope as described in Chapter V.B. Mean areas were inferred from these measurements, as shown in Table 5.10. The target deposit mass thickness results, also shown in Table 5.10, include the 1.56% correction factor previously discussed.

Table 5.10

Results of Target Mass

Thickness Determination

(Errors quoted as % of value)

Electrode Surface	Monitor Foil Mass Thickness, μgms / cm^2	Monitor Foil Areas, cm^2	Target Mass Thickness μgms / cm^2
Al	494.3 $\pm$ 0.61%	2.855 $\pm$ 0.3 %	175.8 $\pm$ 2.3%
Au	503.0 $\pm$ 0.60%	2.847 $\pm$ .14%	179.5 $\pm$ 2.3%

The 2.3% error in the target mass thickness values was obtained using standard error propagation techniques to combine the errors in the monitor foil deposit mass thickness and area determinations. These results agree with the values quoted to us by ORNL in their documentation letter regarding the target vapor deposition (Ada, 72): 173 μgm/ cm^2 $\pm$ 4 μgm/cm^2 and 176 μgm/cm^2 $\pm$ 4 μgm/cm^2 for the monitor foils associated with aluminum and gold surfaces, respectively.

3. Determination of Target Areas.

The technique of diameter measurement using the calibrated optical microscope is described here in detail because of the especially critical nature of these results.

The detector was placed on the moveable stage of the previously described Unitron microscope. (See Section

V.B.2) To assure accuracy of diameter measurements the stage was moved slightly so that the vertical cross hair of the microscope was tangent to the clearly observable ridge of the target deposit. The (x,y) coordinates of this point were recorded. Then the target was scanned until the approximately opposite edge of the deposit intercepted the cross hairs, and the position of the stage again slightly altered to obtain tangency with the vertical cross hair. The diameter was obtained using $D = \left[(y_2 - y_1)^2 + (x_2 - x_1)^2 \right]^{\frac{1}{2}}$, where (x_1, y_1) and (x_2, y_2) are the coordinates read directly from the stage adjustment dials for the points of initial and final tangency. Three such measurements were made for each target deposit. The detector was taken off the stage and replaced in varying orientations to check for uniformity of the diameter. The results are shown in Table 5.11.

The error in the Au side measurements is larger than that for the Al side measurements because of the difficulty encountered in clearly observing the edge of the deposit on the Au electrode. In both cases the error was empirically determined by the degree of reproducibility evidenced in the individual diameter measurements.

Table 5.11.

Measured Target Deposit Diameters and Calculated Areas

(Errors as % of Value)

Electrode Surface	Measured Target Diameter, cm	Mean Target Diameter, cm	Target Deposit Area, cm^2
Al	1.13195 1.13208 1.13213	1.13205 ± 0.08%	1.0065 ± 0.16%
Au	1.16717 1.16542 1.16290	1.16516 ± 0.2 %	1.066 ± 0.4 %

The target areas for the deposits on the Al and Au electrodes, respectively, were directly calculated from the above mean diameter values. The results are included in Table 5.11. The relative error in the areas are exactly twice those in the diameter measurements.

4. Calculation of the Number of Target Nuclei.

Combining the target mass thickness and area values from Tables 5.10 and 5.11, respectively, immediately gives the total target deposit mass as shown in Table 5.12.

Mass spectrographic analysis data obtained at ORNL using one of the monitor foils is also shown in Table 5.12. Using the calculated molecular weight of LiF enriched to 95 atom % ^{6}Li and the total target

deposit mass, the number of LiF molecules in the deposit was determined and, finally, 95% of this number gives the number of ^{6}Li nuclei. This result and the associated error is shown in Table 5.12.

Table 5.12

Summary of Results for the

Number of Target Nuclei

(Errors shown as % of value)

Target Deposit Mass, μgm	$368.3 \pm 1.63\%$
^{6}Li content, atom %	$95 \pm 0.01\%$
Number of ^{6}Li Nuclei	$8.4067 \times 10^{18} \pm 1.7\ \%$

The chemical stability of LiF throughout the vaporization process assures that the vapor deposited target has the same chemical composition as the sample used as the vapor source. (Kob, 75) This was experimentally verified by Le Duigou and Lauer who observed no significant difference between the Li content of evaporated fluoride samples and that of the starting material. (Dui, 71)

D. Photoneutron Source Spectrum.

The neutron spectrum of the Na-Be photoneutron source used in this analysis was calculated for us at NPL using a Monte Carlo code. (Ryv, 71) The results were obtained following 36,000 neutron histories. The spectrum is shown in Figure 5.2 and tabulated in

Appendix I. The source spectrum was also computed using a code written by Bensch and Vesely (Ben, 69) giving almost identical results to those obtained using the NPL code. A brief discussion of the differences has been given by Gilliam (Gil, 73).

The computed spectrum has a mean energy of 964 keV with a FWHM of 32 keV.

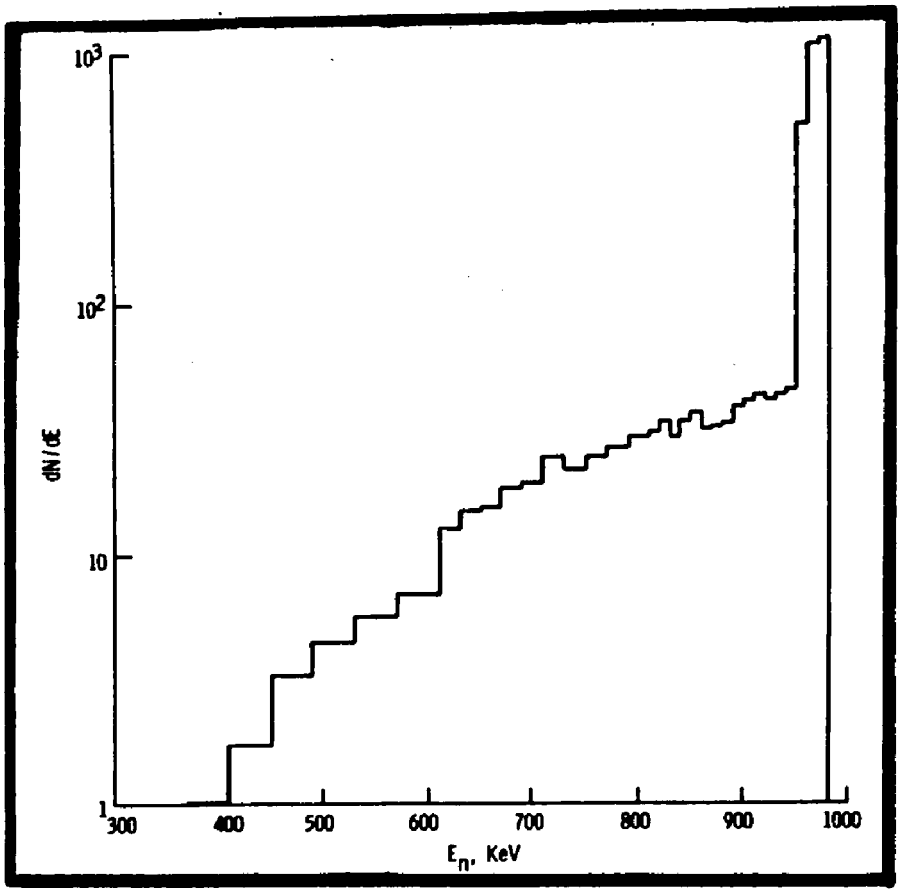


Figure 5.2. Computed Spectrum of the Na-Be Photoneutron Source (Ryv, 71)

CHAPTER VI

CORRECTIONS

A. Detection Efficiency.

1. General Comments.

A detailed calculation of the intrinsic efficiency of the detector - target composite was undertaken to account for target self-absorption of the reaction products and the anisotropy of the yield in the laboratory coordinate system. This calculation was performed for each target separately. The target deposit on the aluminum electrode surface, referred to as the near target since it faced toward the photoneutron source during the experiments, was found to be 100% efficient, i.e. either an alpha particle, a triton or both interacted in the detector for each ^{6}Li (n,α) reaction occurring in the deposit. The target deposit on the gold electrode, referred to as the far target since it faced away from the photoneutron source, was found to be approximately 80% efficient.

The analysis is based on the following assumptions: 1) reaction products do not scatter in the target; 2) the distance a reaction product travels in the target is defined by its range i.e., straggling is ignored; 3) all source neutrons impinge perpendicularly on the target.

2. Reaction Product Energies, Emission Angles, and Range Data.

The energy-angle and angle-angle correlations for the reaction products were obtained by solving the energy and momentum conservation equations using an incident neutron energy equal to the mean source energy, 964 keV. The atomic mass data required to solve energy-momentum equations as well as to calculate the Q-value, were taken from the compilations of Wapstra (Wap, 71). The Q-value is 4.784 MeV. The energy-angle and angle-angle correlation functions are shown in Figure 6.1. For later convenience, the cumulative triton yield as a function of triton emission angle is shown in Figure 6.2, including the results of incorporating the anisotropy of the yield using the angular distribution data of Weddell at 1.1 MeV. (Wed, 59)

The ranges of both the alpha particles and tritons in the target deposits were calculated using Equation 6.A.1.

$$R^{-1} = \sum_i f_i / R_i \ , \ cm^2/gm \qquad 6.A.1.$$

where,

R is the range of the particle in the stopping medium having i constituents,

R_i is the range of the particle in the i^{th} constituent,

f_i is the fraction by weight of the i^{th} constituent

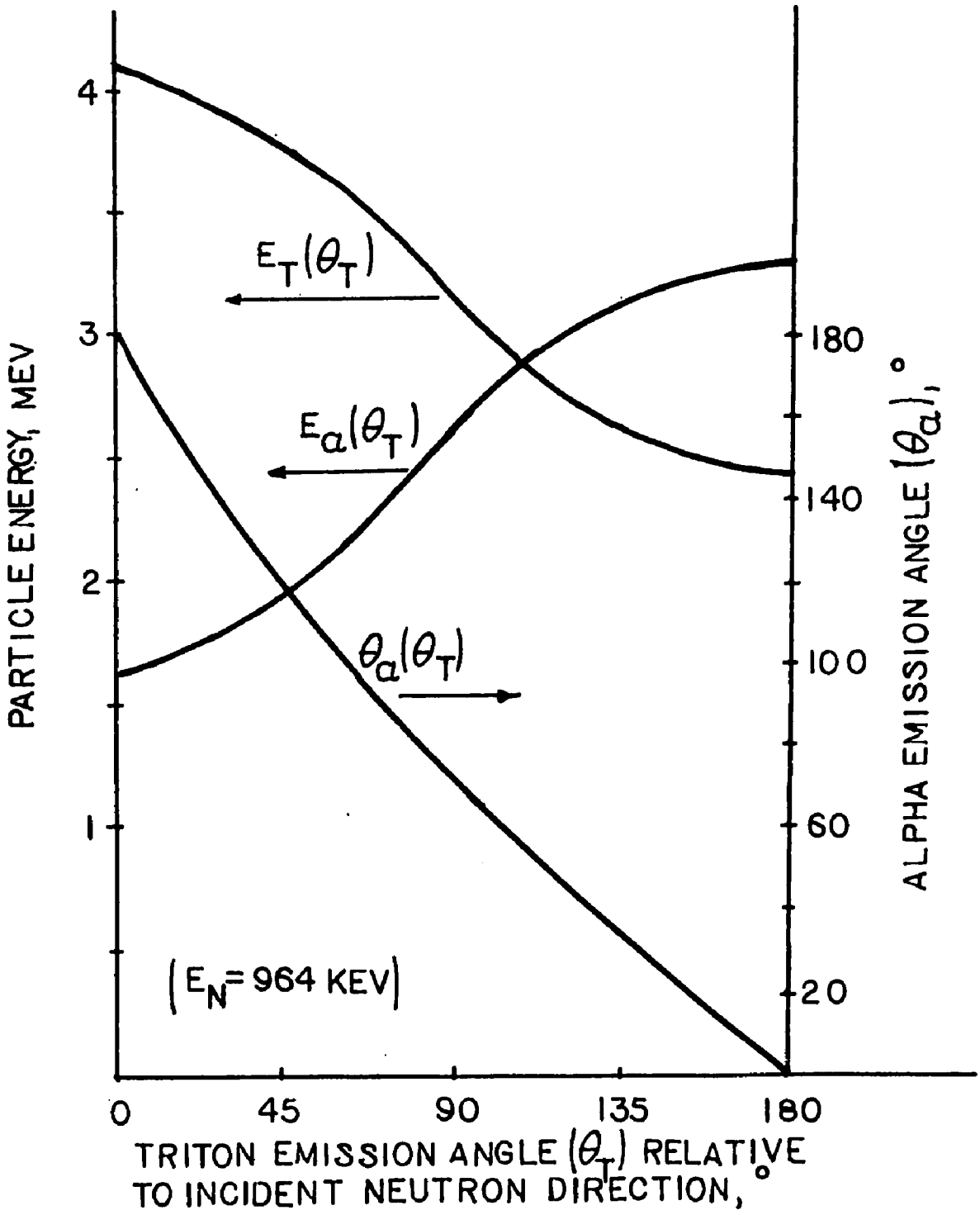


Figure 6.1. Alpha and Triton Energy, and Alpha Emission Angle as a Function of Triton Emission Angle

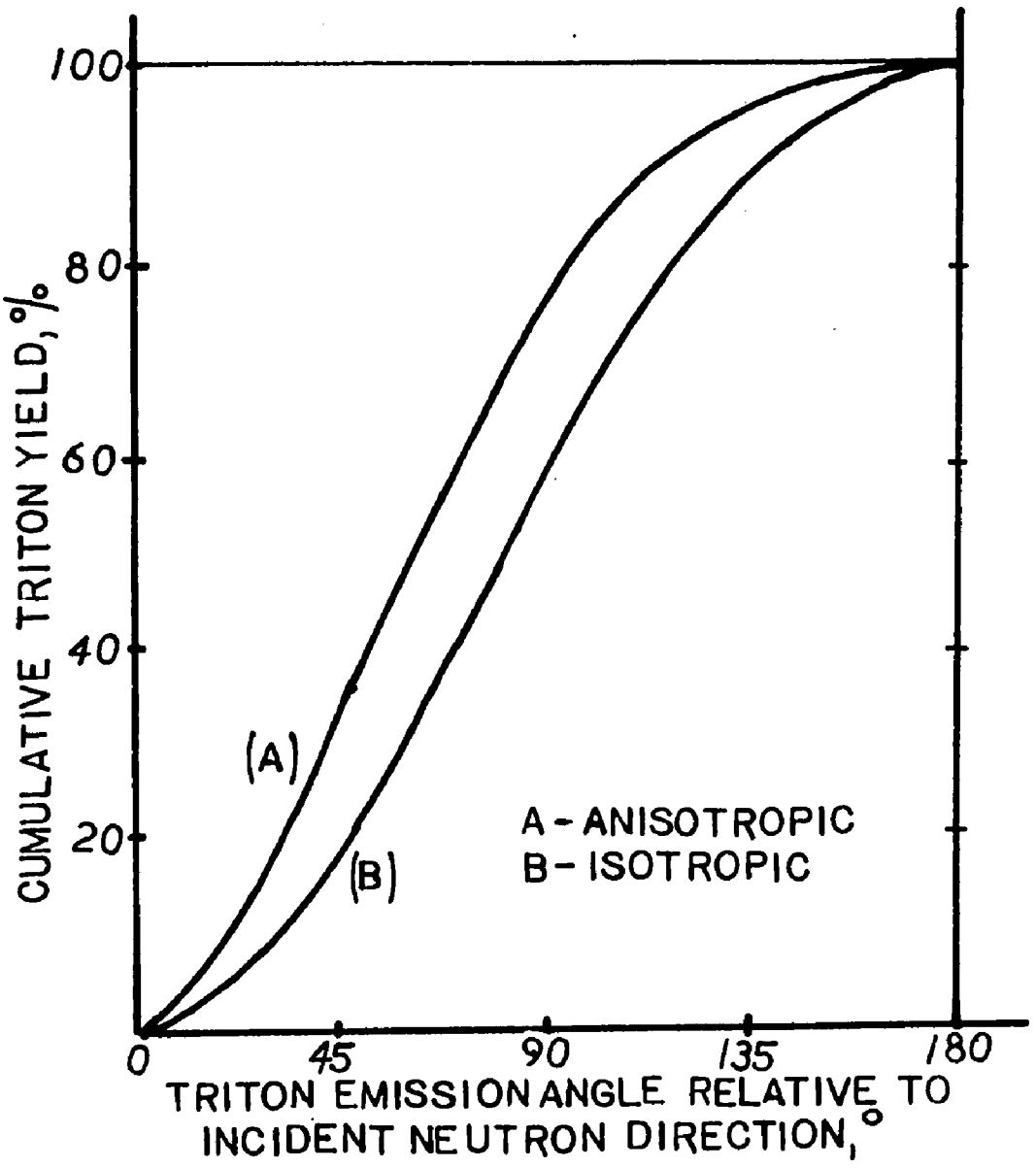


Figure 6.2. Cumulative Triton Yield as a Function of Emission Angle

in the medium (Ueh, 60; NAS, 64).

The weight fractions used were 0.2675 and 0.7325 for lithium and fluorine, respectively. The alpha and triton ranges in lithium and fluorine were taken from the tables of Williamson (Wil, 66). Figures 6.3 and 6.4 show the calculated alpha and triton ranges, respectively, in LiF as a function of particle energy. The range calculations were later redone by integrating the stopping power data of Northcliffe (Nor, 70), giving excellent agreement.

The calculational procedure, applied to both targets, starts with evaluating the effective target thickness as a function of angle relative to the normal to the target plane. For specific angular ranges, the escape probability in the direction of the detector was calculated by comparing the effective target thickness and particle range as a function of angle. The particle ranges are implicit functions of angle with respect to the normal so that, for any given angle, the particle energy is specified from Figure 6.1. Then the range is determined by referring to either Figure 6.3 or Figure 6.4. The angle corresponding to the condition where the effective target thickness is greater than or equal to the particle range defines the limit of the angular range for escape from the target. For each triton or alpha angular range there is a unique relation to the angular range of the

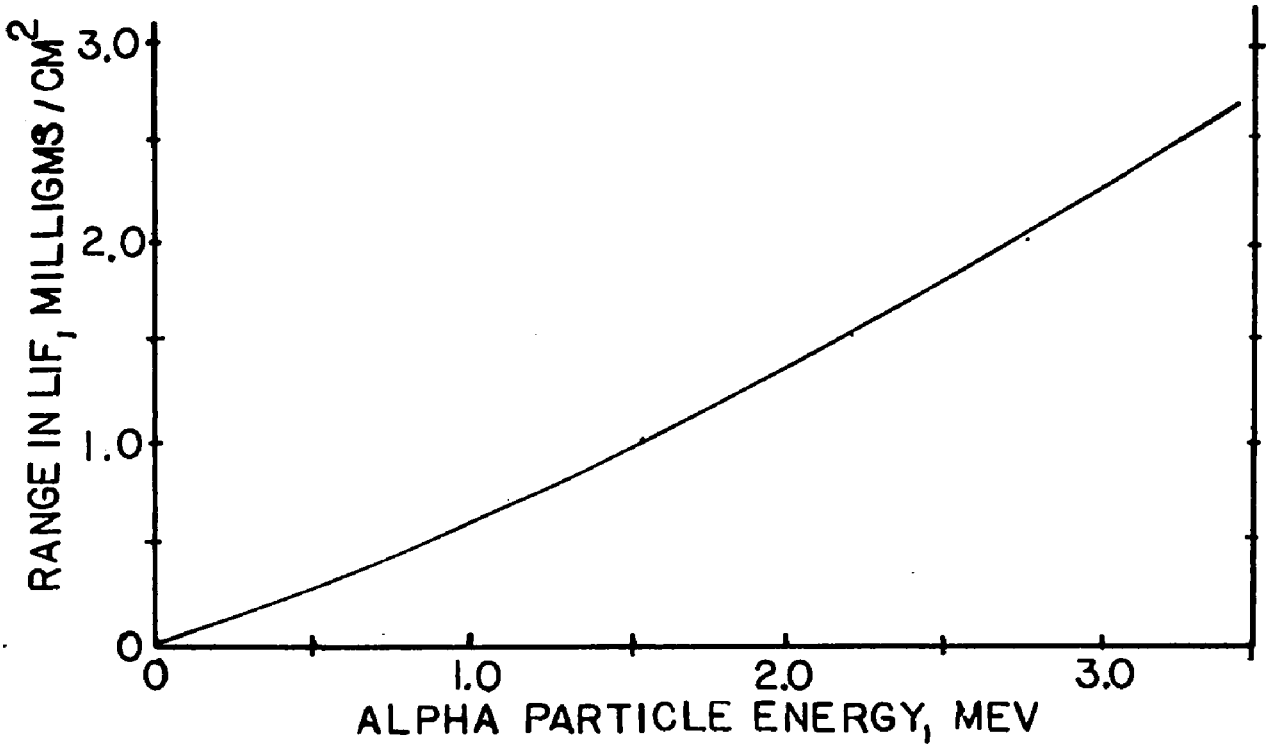


Figure 6.3. Alpha Particle Range in LiF

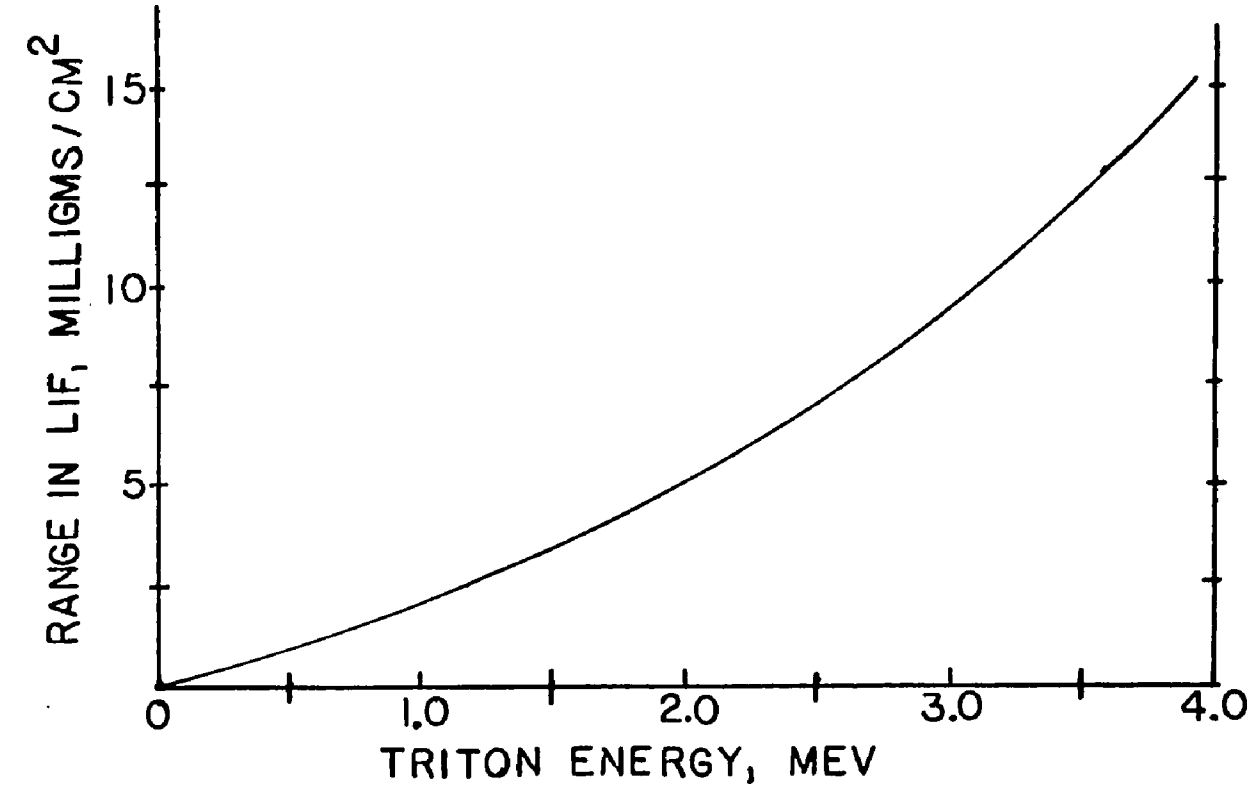


Figure 6.4. Triton Range in LiF

complimentary particle, defined by θ_a (θ_T) plotted in Figure 6.1. The information on the escape fraction is then determined using the cumulative triton yield as a function of angle shown in Figure 6.2. The analysis for each target is shown and then the results are summarized.

3. Near Target Efficiency.

A schematic drawing of the near target relative to the detector is shown in Figure 6.5.

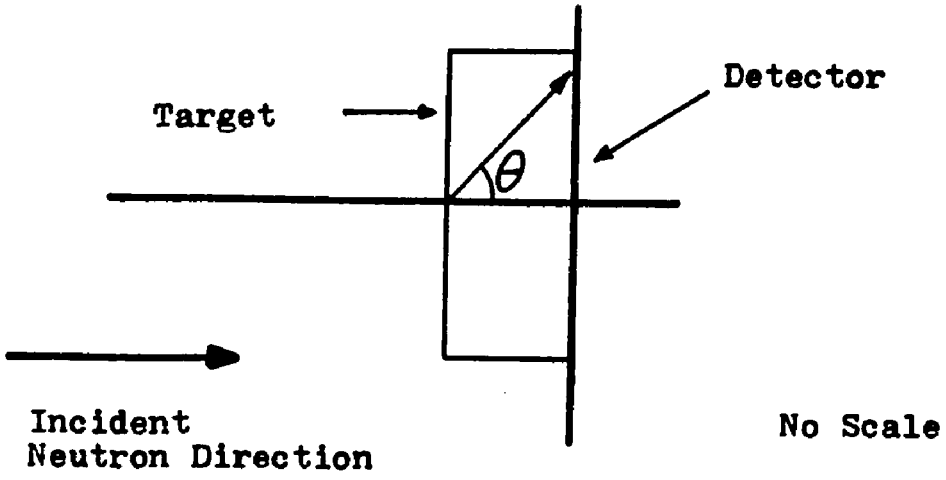


Figure 6.5

Schematic Representation of Near Target and Detector for Efficiency Calculations.

The effective target thickness for the near target is specified by Equation 6.A.2.

$$t_{eff} = 175.8/\cos\theta \text{ , } \mu GMS/CM^2 \qquad 6.A.2$$

For the angular range $90^\circ \leqq \theta_T \leqq 180^\circ$ no tritons will

intercept the detector. The corresponding alpha particle angular range is $0^\circ \leqq \theta_\alpha \leqq 72^\circ$ (Figure 6.1). For $\theta_\alpha = 72^\circ$ $t_{eff} = 569\ \mu gm / cm^2$ whereas the alpha particle range is $1830\ \mu gm / cm^2$. Therefore, all alpha particles escape. The cumulative yeild functions shown in Figure 6.2 lead to the conclusion that 43.5% or 24% of all the reactions occurring in the near target are represented by this case using the isotropic and anisotropic cumulative yield functions, respectively.

The the angular range $90^\circ \leqq \theta_\alpha \leqq 180^\circ$ no alpha particles intercept the detector. The corresponding triton angular range is $0^\circ \leqq \theta_T \leqq 73^\circ$. For $\theta_T = 73^\circ$ $E_T = 3.4$ MeV and the corresponding range is 11200 $\mu gm / cm^2$ as compared with a target thickness of 601 $\mu gm / cm^2$, so that all tritons escape. The isotropic and anisotropic cumulative yield functions show that 41.5% and 62%, respectively, of all reactions in the near target are represented by this case.

The only remaining angular range is $73^\circ \leqq \theta_T \leqq 90^\circ$. Three possible situations must be considered, viz., that reactions producing tritons in this range will: 1) produce no particles which escape toward the detector; 2) produce either an alpha particle or a triton which escapes toward the detector, but not both; 3) produce both an alpha particle and a triton which escape toward the detector.

The results of the analysis are given in terms of the triton angular range.

1) $73^\circ < \theta_T \leqq 78^\circ$.

Only tritons escape toward the detector. Both cumulative yield functions from Figure 6.2 predict that 4.5% of the reaction are represented by this case.

2) $78^\circ < \theta_T \leqq 88^\circ$.

Both reaction products escape toward the detector. The isotropic and anisotropic cumulative yield function predict that 9% and 8%, repectively, of the reactions are represented by this case.

3) $88^\circ < \theta_T < 90^\circ$.

Only alpha particles can escape toward the detector. Both cumulative yield functions predict that 1.5% of the reactions are represented by this case.

In no case are both particles unobserved. Tritons will exit from the near target toward the detector until θ_T is 89°. As θ_T approaches 78°, alpha particles are also able to escape the deposit exiting toward the detector, so that in the angular range $78^\circ < \theta_T < 88^\circ$ both particles are simultaneously observed. The results are summarized in Table 6.1. The minimum and maximum particle energies for the reaction products, taking into account energy loss in the target deposit, are included in Table 6.1.

Table 6.1.

Summary of Detection Efficiency

Calculation for the Near Target

Triton Angular Range	Reaction Product(s) Detected	Energy Range, MeV	Per Cent of Reactions	
			Anisotropic	Isotropic
$[0°, 78°]$	T	3.0-3.9	66.5	46.0
$(78°, 88°]$	α and T	4.4-4.7	8.0	9.0
$[88°, 180°]$	α	2.2-3.2	25.5	45.0
		Total	100.0	100.0

4. Far Target Efficiency.

The calculation of the far target efficiency proceeds in the same manner as the previous calculation of the near target efficiency. However, whereas the forward peaking of the reaction product yield enhanced the detection efficiency for reaction products from the near target, the same phenomenon causes a loss of efficiency for the far target. In consequence, there is a need for greater accuracy in the far target efficiency calculation than for the near target case. The accuracy of the calculation was increased by applying the same method to five uniformly spaced points along the axis of the far target, as shown in Figure 6.6. P_0 is at the detector - target interface, P_4 at the extreme surface and P_2 at the

midpoint. The effective target thickness for the calculation associated with P_4 is $179.4/\cos\theta$. $\mu gm / cm^2$. The effective target thicknesses for the four other points was proportionately reduced, being zero for P_0.

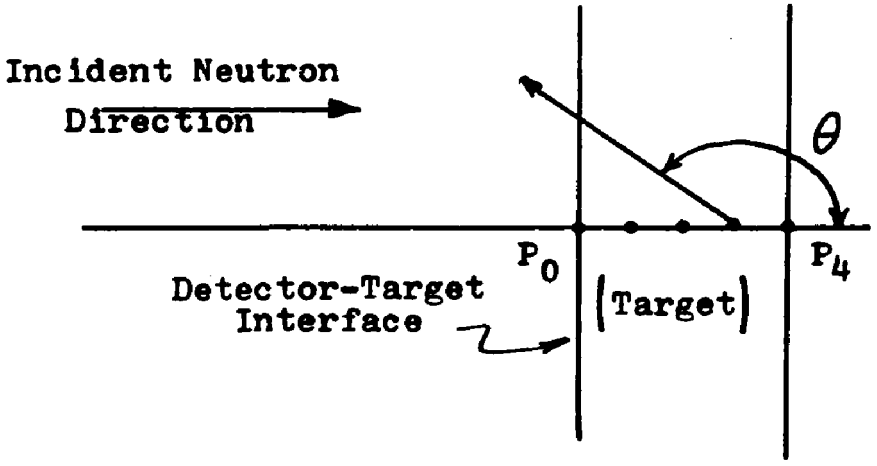


Figure 6.6.

Schematic Representation of Far Target and Detector for Efficiency Calculations

The triton angular range for which escape from the target in the direction toward the detector occurs is $90^\circ < \theta_T \leqq 180^\circ$. The corresponding alpha angular range was calculated by comparing alpha particle ranges and effective thicknesses at each point. The results are summarized in column 1 of Table 6.2. For this case only tritons will be observed.

For the alpha angular range $90^\circ < \theta_\alpha \leqq 180^\circ$ only alpha particles will be detected. These results are also summarized in Table 6.2, column 2.

Table 6.2.

Triton and Alpha Angular Ranges for

Particle Escape from Far Target Toward Detector

Node Point	Range of θ_T Such That Only Tritons Detected	Range of θ_α Such That Only Alpha Particles Detected
P_0	$90^\circ < \theta_T \leq 180^\circ$	$90^\circ < \theta_\alpha \leq 180^\circ$
P_1	$91^\circ \leq \theta_T \leq 180^\circ$	$92^\circ \leq \theta_\alpha \leq 180^\circ$
P_2	$91^\circ \leq \theta_T \leq 180^\circ$	$94^\circ \leq \theta_\alpha \leq 180^\circ$
P_3	$91^\circ \leq \theta_T \leq 180^\circ$	$95^\circ \leq \theta_\alpha \leq 180^\circ$
P_4	$92^\circ \leq \theta_T \leq 180^\circ$	$97^\circ \leq \theta_\alpha \leq 180^\circ$

To determine the fraction of ^6Li (n,α) reactions in the far target corresponding to these angular ranges, the ranges of θ_T corresponding to the ranges of θ_α listed in Table 6.2 were obtained from Figure 6.1. Then the cumulative yield for the isotropic and anisotropic cases from Figure 6.2 was used to calculate the fraction of events represented. These results are shown in Table 6.3.

The minimum and maximum reaction product energies, taking into account energy loss in the target, were calculated to be 1.36 MeV to 2.4 MeV for the alpha particle and 2.36 MeV to 3.1 MeV for the triton, within the limits defined by the angular ranges given in Table 6.3.

Table 6.3.

Summary of Detection Efficiency

Calcuations for the Far Target

Node Point	Angular Range of for Alpha or Triton Detection	Per Cent of Reactions In Far Target Represented % Isotropic	Anisotropic
P_0	$\left\{ \begin{array}{l} 90^\circ < \theta_T \leqq 180^\circ \\ 0^\circ < \theta_T \leqq 72.5^\circ \end{array} \right\}$	84.9	85.5
P_1	$\left\{ \begin{array}{l} 91^\circ \leqq \theta_T \leqq 180^\circ \\ 0^\circ < \theta_T \leqq 71.1^\circ \end{array} \right\}$	82.6	83.8
P_2	$\left\{ \begin{array}{l} 91^\circ \leqq \theta_T \leqq 180^\circ \\ 0^\circ < \theta_T \leqq 69.3^\circ \end{array} \right\}$	81.0	82.0
P_3	$\left\{ \begin{array}{l} 91^\circ \leqq \theta_T \leqq 180^\circ \\ 0^\circ < \theta_T \leqq 68.4^\circ \end{array} \right\}$	80.0	81.0
P_4	$\left\{ \begin{array}{l} 92^\circ \leqq \theta_T \leqq 180^\circ \\ 0^\circ < \theta_T \leqq 66.5^\circ \end{array} \right\}$	75.5	78.0
	Mean Efficiency, %	81.0	82.1

The far target efficiency obtained using the volume weighted average of the values obtained at each node point is 80.95% and 82.14% for the isotropic and anisotropic cases, respectively. The far target efficiency was taken as the average of these values, 81.5%.

The efficiency of the target - detector composite was obtained by weighting the near and far target efficiencies by the target masses, 176.96 μgms and 191.31 μgms,

respectively. The value obtained for the intrinsic efficiency of the target - detector composite is 90.5%.

To evaluate the error in this value due to the choice of angular distribution function, the calculation was redone using both the isotropic (in the center-of-mass system) and anisotropic distributions. The limits on the efficiency were found to vary by $\pm$ 0.2%.

The major error source is due to uncertainties in the adequacy of the model to represent the escape probability of reaction products from the far target due to uncertainties in the range calculations. However, empirical determination of the influence of the particle range uncertainty showed that a 20 per cent error in the range causes a 0.5 per cent error in the value obtained for the far target efficiency.

The assumption of a monodirectional neutron current incident perpendicularly on the detector target composite is considered adequate, since the off-axis, non-perpendicular neutron contributions from the source are symmetric and mutually compensating.

The error associated with the detector - target composite efficiency is the quadrature sum of the range and angular distribution errors, $\pm$ 0.54%.

B. Local Inscatter.

1. Analytic Model.

The contribution to the ^{6}Li (n,α) reaction rate due

to inscattered neutrons was approached as a perturbation to the flux at the target. Referring to Figure 6.7, the flux at the target due to neutrons coming directly from the source, denoted by ϕ_o, is proportional to $1/4\pi R^2$.

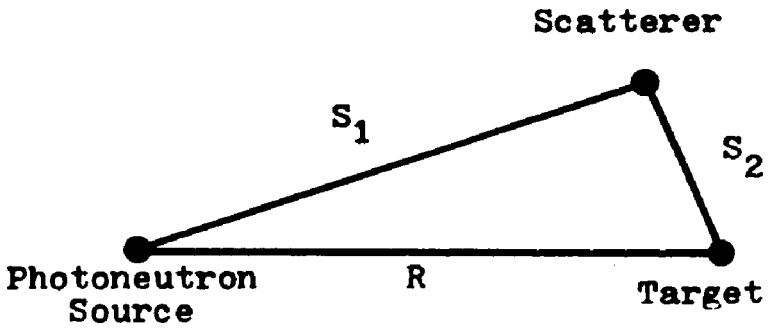


Figure 6.7.

Diagram for Inscatter Evaluation

The flux at the scatterer is proportional to $1/4\pi S_1^2$ and the scattered flux at the target, denoted by $\delta\phi$, is proportional to $1/4\pi S_2^2$. The flux at the target, ϕ_T, is given by Equation 6.B.1.

$$\phi_T = \phi_o + \delta\phi \qquad 6.B.1.$$

For convenience, this is rewritten as shown in Equation 6.B.2.

$$\phi_T = \phi_o \left(1 + \delta\phi/\phi_o \right) \qquad 6.B.2.$$

Assuming isotropic scattering in the laboratory coordinate system, $\delta\phi$ is given by Equation 6.B.3,

$$\delta\phi = \frac{A_N}{4\pi S_1^2} V_S \Sigma_S / 4\pi S_2^2 , \qquad 6.B.3.$$

where,

V_S = volume of the scatterer,

Σ_S = macroscopic scattering cross section at the mean source energy, 964 k eV, and

A_n = neutron source strength.

Since $\phi_o = A_n / 4\pi R^2$, $\delta\phi / \phi_o$ can be obtained from Equation 6.B.3 as shown in Equation 6.B.4.

$$\delta\phi/\phi_o = R^2 S_1^{-2} V_S \Sigma_S / 4\pi S_2^2 \qquad 6.B.4.$$

Equation 6.B.4 is the basic equation used in the analysis. Several refinements will now be discussed which enhance the validity of results.

The first correction relates to the term S_2. S_2 was modified to take into account the finite extent of the target, giving an effective distance from the point scatterer to the target. For the case of a point scatterer in the plane of the target, S_2 is given by Equation 6.B.5.

$$S_2^{-2} = R_T^{-2} \ln\left| d^2 / \left| d^2 - R_T^2 \right| \right| \qquad 6.B.5.$$

where,

R_T = radius of the target deposit, and

d = distance from the point scatterer to the center of the target deposit.

If the scattering source is not in the plane of the target, then S_2 is determined using Equation 6.B.6.

$$S_2^{-2} = R_T^{-2} \ln \left\{ \left[\left(h^2 + d^2 \right)^2 + 2\left(h^2 - d^2 \right) R_T^2 + R_T^4 \right]^{1/2} + R_T^2 + h^2 - d^2 \Big/ 2h^2 \right\} \quad 6.B.6.$$

where,

h is the distance of the scattering source from the plane of the target.

Secondly, although the point source model was consistently used to represent the photoneutron source, the distance from the photoneutron source to the scattering source, S_1, was replaced by a mean value whenever the physical extent of the scattering object would cause greater than a 10 per cent variation in S_1.

This method was applied to all components in the vicinity of the photoneutron source and target with one exception. The epoxy fillet which holds the silicon detector to the insulating lavite ring contains hydrogen. Because of the unique neutron scattering characteristics of hydrogen, as regards both the angular distribution and energy of the scattered neutrons, inscattering from hydrogen is treated separately.

To specify the macroscopic scattering cross sections

of all the materials associated with the experiment, chemical composition and density data was obtained from vendor specifications or standard handbooks. The microscopic scattering cross sections were obtained from BNL-325, edition 2.

2. Inscatter Due to Hydrogen in Epoxy.

The chemical composition of the ORTEC "High Vac" epoxy was determined by elemental analysis (Spa, 73) as shown in Table 6.4.

Table 6.4.

Chemical Composition of ORTEC "High Vac" Epoxy

Element	Atomic Mass Percentage, %
Carbon	71.05
Hydrogen	7.38
Oxygen	17.92
Nitrogen	3.22
"Ash"	0.00

The density of the cured material is 1.15 gms / cc.

The volume of epoxy was determined by measurements using the same calibrated optical microscope set-up as used for measuring the target diameters, comparing the data obtained using the actual detector with data obtained using a bare lavite ring. These volumes as well as the relevent dimensions of the detector are

shown in Figure 6.8. It is assumed that all hydrogen scattering occurs at the center of mass of the epoxy fillet, the associated volume being the sum of the fillet volumes, 0.139 cc.

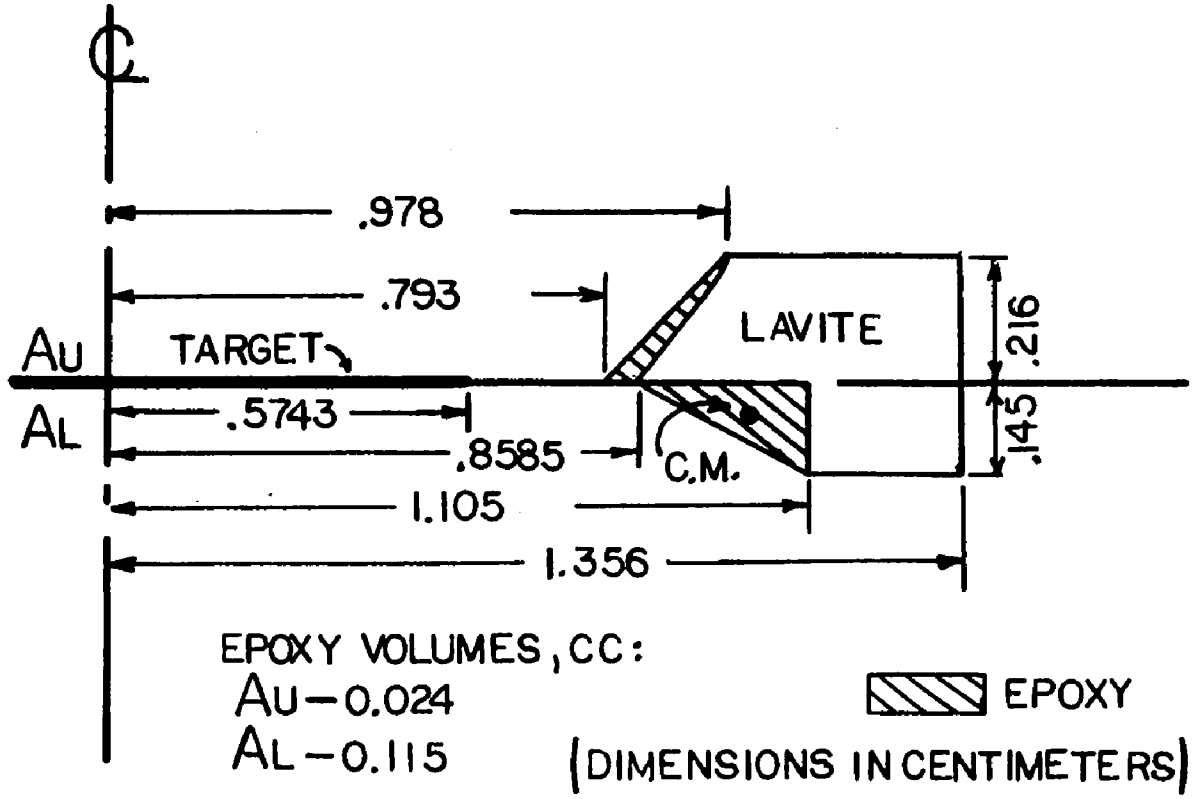


Figure 6.8.

Cross Sectional View of Epoxy Fillets, Lavite Ring and Target Deposits

Because the photoneutron source was always on the aluminum side of the detector during the cross section experiments, the forward scattering property of hydrogen assures that using the center of mass of the epoxy fillet as the scattering point is conservative.

The energy of neutrons scattered from hydrogen is

determined by the cosine of the scattering angle according to Equation 6.B.7.

$$E_N = E_0 \cos^2(\theta_S) \qquad 6.B.7.$$

where,

E_0 = incident neutron energy,

E_n = final neutron energy and

θ_S is the scattering angle.

Using the normalized probability distribution function for neutron scattering from hydrogen, the probability that a neutron with an incident energy E_0 will be scattered to an energy E_n, where $E_1 \leqq E_n \leqq E_2$, is given by Equation 6.B.8.

$$\int_{E_1}^{E_2} P(E_0 \rightarrow E)\, dE = E_0^{-1}(E_2 - E_1) \qquad 6.B.8.$$

The first case considered assumes the neutron flux from the source to be monodirectional, perpendicular to the plane of the target.

The range of the scattering angle for interception with the target was determined using the geometric relations between the target and the center of mass of the epoxy. The scattered neutron energies corresponding to these maximum and minimum scattering angles were used to determine the fraction of neutrons scattered into

this cone. The fraction of these neutrons that would intercept the target was estimated by taking the ratio of the target area to the area of the projection of the angular cone, defined by the maximum and minimum scattering angles, onto the plane of the detector. It was concluded that 0.14 per cent of the neutrons scattered from the epoxy would intercept the target.

The flux perturbation, $\delta\phi/\phi_o$, was evaluated using the hydrogen scattering cross section at 964 keV, and found to be 0.006%. Finally, the ^6Li (n,α) cross section energy dependence was used to determine the relative worth of these inscattered neutrons compared with those at the mean source energy. This increased the flux perturbation by a factor of 10, i.e. to 0.06%. This value applies to the close spacing experiment. The calculation was redone for the far spacing experiment and found to be 0.006%.

The assumption of a monodirectional neutron flux normally incident on the target plane was relaxed to evaluate the effect of the spatial distribution of the source on the hydrogen inscatter correction. The assumption that all the source neutrons are produced at the extreme points of the photoneutron source was made, and calculations identical to the previously described monodirectional normal flux case were completed. The only effect is that the angular range for interception

of scattered neutrons by the target is altered.

For the close spacing (9 cm) case, the maximum hydrogen inscatter correction was found to be 0.045%; for the far spacing case, 0.004%.

In summary, the maximum flux perturbations due to the hydrogen content of the epoxy were found to be 0.06% and 0.006% for the close and far spacing runs, respectively.

3. Inscatter Due to Non-hydrogenous Components.

Because of the lengthiness and repetitiveness of the calculations, only the details for the inscatter correction due to the lavite insulating ring which holds the silicon detector will be shown. The lavite ring inscatter correction is selected as an example both because it is typical and since it is the largest single contributor to the total inscatter correction. The results obtained for the remaining components will then be summarized.

The calculations were done for both the 9 cm and 20 cm source - target spacings. This is necessary since the $\delta\phi$ term depends on S_1 and S_2, the source to scatterer distance and the scatterer to target distance, respectively, which vary more slowly than R, the source - target spacing. (See Figure 6.7) Therefore, for a given increase in R, $\delta\phi$ decreases more slowly than ϕ_o. The result is that $\delta\phi/\phi_o$, the relative flux

perturbation due to inscattering, is larger at the 20 cm source - target spacing than for the 9 cm spacing.

To evaluate the inscatter contribution for any component, the physical dimensions of the component itself as well as its distance from the source and target, and its macroscopic scattering cross section at 964 keV must be specified. This procedure is shown for the insulating lavite ring.

A cross sectional view through the lavite ring is shown in Figure 6.8. The dimensions of the ring itself were determined by measurements using the calibrated optical microscope, as for the target deposit size measurements, on a bare ring, i.e. without a detector mounted within it, supplied by ORTEC.

The scattering volume was assumed to be in the plane of the target. Therefore, equations 6.B.4 and 6.B.5 are used to determine $\delta\phi/\phi_o$. Equation 6.B.4 was simplified by setting the source - target distance equal to the source - scatterer distance. The remaining values to be determined are S_2, the target center to scatterer distance defined by Equation 6.B.5, the volume of the lavite ring and the macroscopic scattering cross section of lavite. S_2 is determined by R_T, the mean target radius and d, the distance from the target center to the center of mass of the lavite ring. The values for the geometric variables are listed in Table 6.5.

Table 6.5.

Geometric Variables for Evaluating

Lavite Ring Inscattering

Term	Value	Source of Value
V_S, lavite ring volume	1.090 cc	Calibrated microscope measurements (Figure 6.8)
d, target center to scattering center distance	1.1703 cm	Same as above
R_T, mean Target radius	0.5743 cm	Same as above (see Section V. C. 3)

Using the values in Table 6.5 S_2 was determined using Equation 6.B.5. The macroscopic scattering cross section of lavite was evaluated from its chemical composition, $3\ Al_2O_3 \cdot 2\ SiO_2$, constituent microscopic scattering cross sections at 964 keV, and a supplier's stated density of 2.3 gm / cc. $\delta\phi/\phi_o$ was calculated as 2.11%.

Similarly, calculations of $\delta\phi/\phi_o$ were individually made for all components of the experiment package for both the 9 cm and 20 cm source - target spacings. The results are summarized in Table 6.6.

Table 6.6.

Summary of Results for Inscattering Corrections Due to Components of the Experiment Package

Component	$\delta\phi/\phi_o$, % Close Spacing Experiment	Far Spacing Experiment
Detector Itself and Electrode Deposits	.00313	.00313
Lavite Ring	2.11	2.11
Epoxy, Including Hydrogen	.262	.262
Detector Mount (10 Separate Components)	2.49	2.617
Electrical Connectors and Supports	.267	.481
Source Support Structure	.174	.345
Tubular Support Frame	.503	.709
Cadmium Cylinder and Support Structure	.238	1.18
Total (linear sum)	6.047	7.71

Many approximations were used to obtain the relative inscattered flux correction terms described above. The model incorporated only single scattering, assumed to be isotropic in the laboratory coordinate system. Also the scattering components were mathematically considered

as point scattering sources, their geometric extent being taken into account by calculating effective distances from the photoneutron source and the target deposits. The assumption was also made that the interaction probability of inscattered neutrons with the ^{6}LiF targets was the same as that of the neutrons coming directly from the source. Implicit herein is the assumption that the lower energy of the scattered neutrons does not enhance their interaction probability with the target deposits. This effect has been evaluated as described below.

The minimum and mean energy of the inscattered neutrons was calculated for the individual scattering components. (The case of hydrogen scattering was treated separately in Section VI.B.2. and is excluded from this discussion.) Using an incident neutron energy of 964 keV, as estimate was made of the mean energy of scattered neutrons intercepting the target and found to be approximately 880 keV. Using the energy dependent shape function of the ^{6}Li (n,α) cross section measured by Friesenhahn (Fri, 74), the interaction probability would be increased by 4% for neutrons of 880 keV relative to the interaction probability for neutrons at the mean source energy. The relative inscatter contribution was increased by 4% to account for this effect, giving $\delta\phi/\phi_o$ as 6.29% and 7.95% for the close

and far spacing runs, respectively. The error associated with this effect is estimated as ± 15% based on the variance in inscattered neutron energies relative to the ^{6}Li (n,α) cross section energy dependence.

Finally, in recognition of the large number of error sources contributing to the final result for the inscatter correction term an additional systematic error of ± 50% is included in the final value. The inscatter correction terms and associated errors are shown in Table 6.7.

Table 6.7.

Relative Flux Perturbation Due to Local Inscatter

Source-Target Spacing	$\delta\phi/\phi_o$,%	Error as % of Value
Close	6.29	± 65
Far	7.95	± 65

C. Charged Particle Production.

1. General Comments.

Detailed consideration of the possibility of charged particle production due to neutron interaction with the components of the experiment package, including the air space surrounding the detector, was included in the preliminary design of the experiment. These initial calculations showed only two components to be of poss-

ible significance, namely the epoxy fillet surrounding the periphery of the detector and the lavite ring. Subsequent calculations of contributions from the lavite ring showed it to be insignificant. A thorough review of these calculations revealed a serious error had been made in the evaluation of the proton contribution via the $^{14}N(n,p)$ reaction in the dry air envelope surrounding the detector. This correction is discussed, followed by a brief review of the small correction due to the contribution from the epoxy fillet.

In general, because of the self absorption of charged particles within the components where they are generated, coupled with the small solid angle these components subtend at the detector, the actual number of such particles impinging on the detector is insignificant. Also the silicon of the detector itself was considered a possible source through the (n,α) and (n, p) reactions. However, the cross sections for these reactions is zero below neutron energies of 4 MeV. (Bul, 50; How, 64; Al, 68).

2. Analysis of Charged Particle Sources.

a. Proton Yield from the Air Envelope Surrounding the Detector. The proton energy as a function of emission angle relative to the incident neutron direction was obtained by solving the energy-momentum conservation equations using a Q-value of 626.4 keV

(Map, 66). The angular yield function for the protons was calculated in the laboratory coordinate system assuming isotropic yield in the center of mass coordinate system.

The cross section for the ^{14}N (n, p) reaction was obtained from the work of Abdau. (Abd, 73). This cross section was weighted using the tabulated photoneutron source spectrum given in Appendix I, giving a value of 16.23 mb at the mean source energy, 964 keV. The ^{14}N number density was obtained for dry air, as used in the experiment, using air composition data from the Handbook of Chemistry and Physics. The range of the protons in air, LiF and the electrode deposits was obtained using the stopping power data of Northcliffe. (Nor, 70).

A detailed calculation of the number of proton events was carried out for the close spacing experiment. These results were extrapolated to the far spacing experiment case using the integrated neutron activities as the basis of scaling.

The maximum air volume coupled with the detector was determined by subtracting the range of a 1.2 MeV proton in air from the range of a 1.585 MeV proton, the most energetic proton occurring in the situation, giving a maximum coupling distance of 1.76 cm. 1.2 MeV was used as the lower energy threshold since, for the close spacing run, data recorded during the experiment was not used

below this energy. This air envelope was then divided into spatial elements and the proton yield from each element was calculated. The envelope and spatial elements are shown in Figure 6.9.

The air volume associated with each element is the volume of revolution calculated by revolving the element around the rotational symmetry axis. The integrated neutron current at the element was obtained by dividing the integrated neutron activity of the source by 4π times the centroid-to-source center distance squared. The total number of protons generated in the element during the live time of the experiment was then calculated.

To determine the proton count associated with an element, the probability that a proton generated in it would intercept the detector with a residual energy greater than or equal to 1.2 MeV was calculated. An angular range in which protons with energies above the 1.2 MeV threshold could reach the detector was calculated, taking into account the attenuation in air, in the target and in the associated electrode deposit and, of course, was physically cut off when interception with the epoxy - lavite annulus occurred. Once the angular range was known, the angular yield function gave the per cent yield in the cone. Finally, a geometric efficiency factor was calculated. This factor was defined as the ratio of the area of the yield cone intercepted by the detector

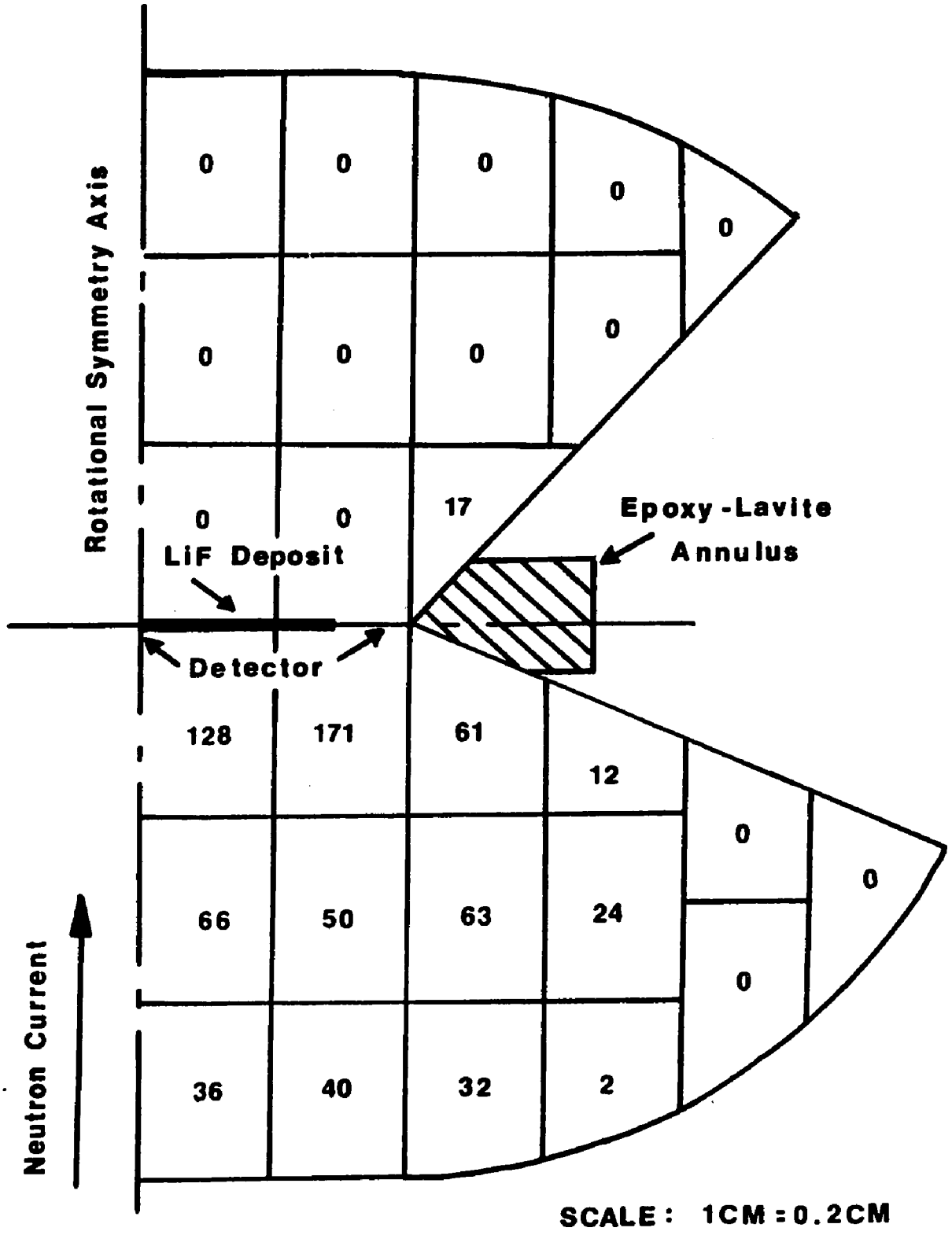


Figure 6.9. Air Envelope Coupled with Detector for $^{14}N(n, p)$ Correction--Close Spacing Run

divided by the total area of the yield cone projected onto the plane of the detector.

For the close spacing run, the number of protons intercepting the detector at energies greater than 1.2 MeV was calculated for 27 spatial elements. The contribution of each element is shown in Figure 6.9. The total number of events for both the close spacing and far spacing runs is shown in Table 6.8. The total proton count for the far spacing run was obtained by scaling on the basis of integrated neutron current, taking into account the differences in the lower energy limits for the experiments.

Table 6.8.

Calculated Proton Count for Close and Far Spacing Experiments

Energy Range, MeV	No. of Protons Events	% of Total Count
I: 1.2 - 1.4	702 ± 562	14.3
II: 1.074 - 1.4	263 ± 210	19.4

The effect of the proton contribution on the observed detector response spectrum is shown in Figure 6.10 and 6.11 for the close and far spacing runs, respectively.

Although the magnitude of the proton count correction is sufficiently large to make a direct measurement of the effect desireable, the model described above was

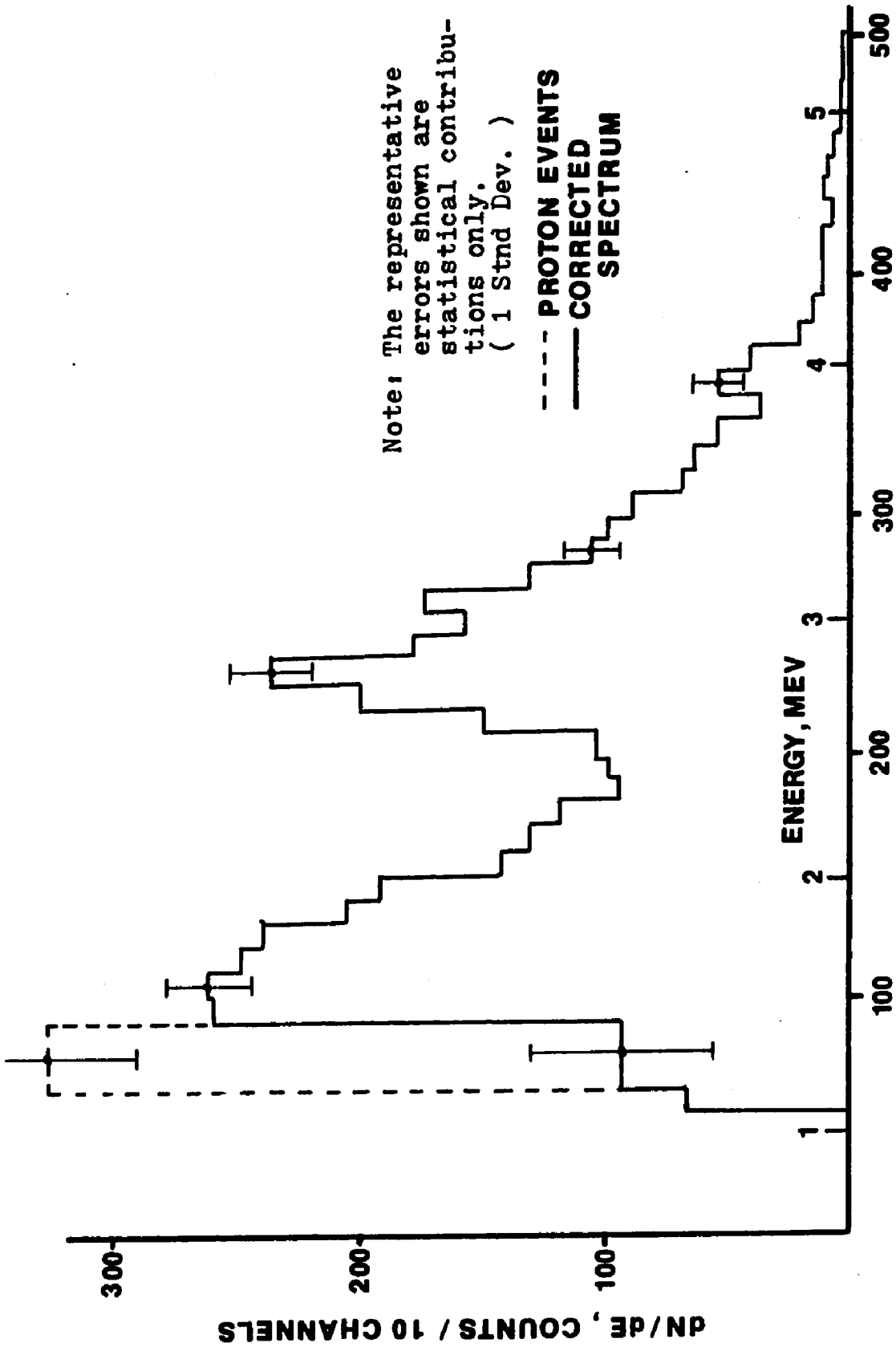


Figure 6.10. Pulse Height Spectrum and $^{14}N(n, p)$ Correction--Close Spacing Run

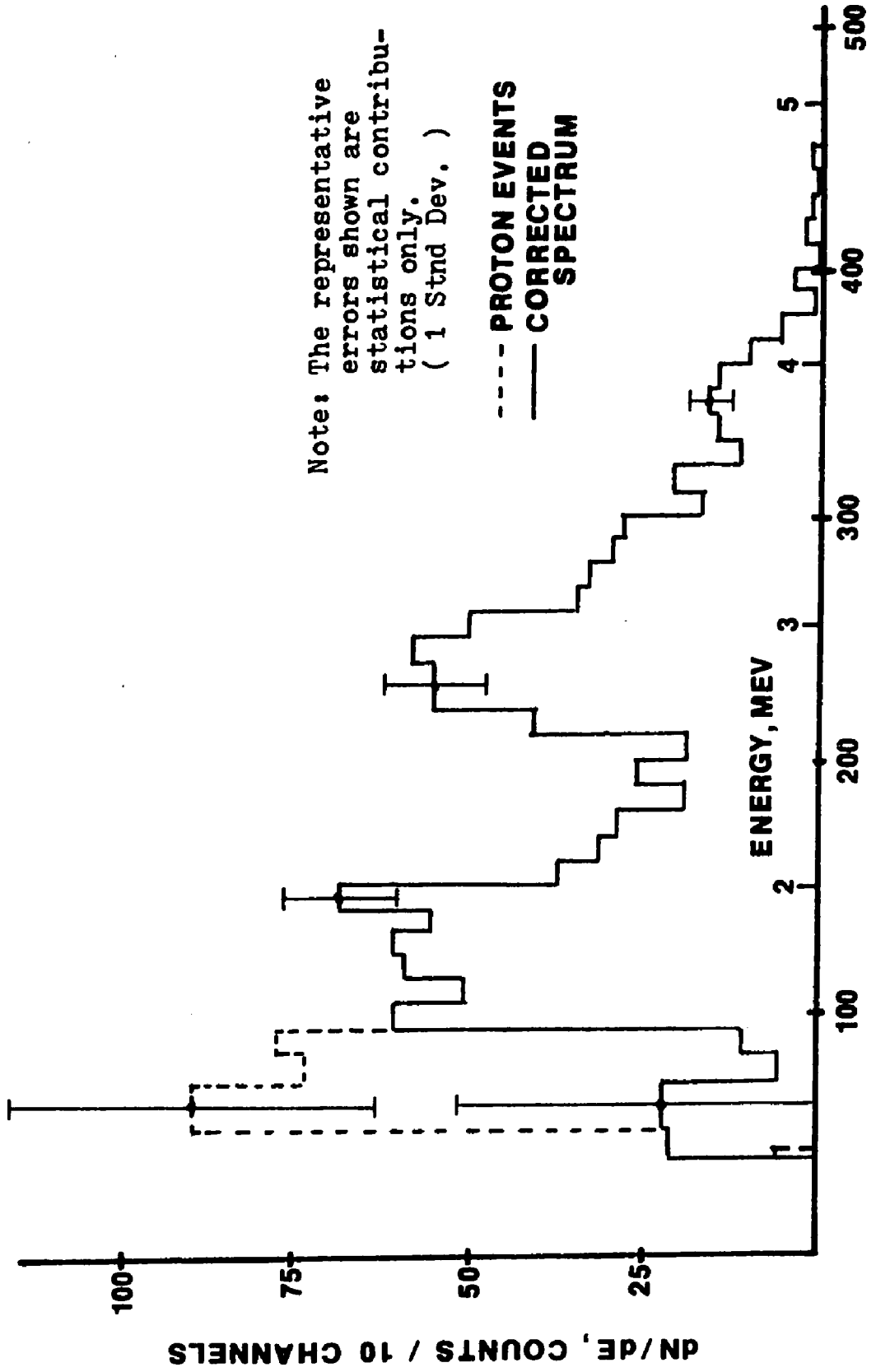


Figure 6.11. Pulse Height Spectrum and $^{14}N(n, p)$ Correction--Far Spacing Run

chosen as the most expedient alternative. A careful and conservative approach in evaluating the errors associated with this model was adopted.

To summarize the error sources three contributing factors are distinguished: 1) the number of ^{14}N (n, p) reactions occurring in the air space; 2) the intrinsic efficiency of the detection system; 3) the extrinsic efficiency, i.e., the probability that a proton produced in the air space will intercept the detector at an energy above the counting threshold. These results are shown in Table 6.9.

Table 6.9.

Error Terms for the ^{14}N (n, p) Correction

Error Source	Error as Per Cent of Value, %
Total number of reactions:	
Integrated source neutron activity	± 1
Spectrum weighted cross section	± 20
Intrinsic efficiency	
System resolution	± 50
Extrinsic efficiency	
Monodirectional neutron current	± 5
Detector dimensions	± 20
Proton range in stopping media	± 10
Reaction kinematics	± 10
Spatial lumping	± 25
Geometric interception probability	± 15
Quadrature sum	± 66

To include consideration of cross correlated effects and to take into account the assumption of uniform energy distribution of the proton yield made in the extrapolation for the close to the far spacing run, a final error of $\pm$ 80% was assigned to the correction term.

The error due to the integrated source neutron activity is based on the $\pm$ 0.9% value stated in Chapter IV. The 20% uncertainty contributed by the spectrum weighted cross section is determined by the accuracy of the ^{14}N (n, p) cross section in the keV energy range.

Since the detector is fully sensitive to the maximum energy proton generated by the ^{14}N (n, p) reaction, the uncertainty in the proton count due to the intrinsic efficiency of the system is due to the low system resolution. This makes our knowledge of the number of these proton events above the 1.2 MeV counting threshold poorly defined. Since the test pulse FWHM at 1.4 MeV was 250 keV, which is comparable to the calculated energy range of the incident protons, a maximum uncertainty of 50% was associated with this effect.

The 5 per cent error caused by using the assumption of a monodirectional neutron current was determined by recalculating the proton contribution for several spatial elements using a spatially extended representation of the photoneutron source. The 20 per cent error associated with the detector dimensions arises from uncertainties in the shape of the epoxy fillets holding the detector to

the lavite ring which in turn determines the size of the air envelope coupled with the detector.

The proton range in air, aluminum, gold and lithium fluoride is not a major error source. The proton range in aluminum and gold is known to 20% (Wil, 66). The combining of elemental ranges to obtain data sets for LiF and air adds a small error. Using a maximum error of $\pm$ 30% for the proton ranges in air and LiF, a maximum uncertainty in the proton count of $\pm$ 6% was obtained for sample spatial elements. Conservatively, an error of 10% was assigned to this term.

The 10% error attributed to reaction kinematics recognizes the lack of knowledge of the angular distribution of the ^{14}N (n, p) cross section. In lieu of any data, the assumption of isotropy in the center of mass system was made.

The errors due to the particular spatial mesh selection and the geometric interception probability calculation are both model dependent and were empirically determined.

b. Proton Yield from the Epoxy Fillet. The maximum proton energy is 1.585 MeV. The total number of protons generated in the epoxy layer facing the detector and having a thickness equal to 23 microns was calculated for both the close and far spacing experiments. Only those generated within this distance are able to

escape with an energy greater than 1 MeV. The angular range for detector interception was calculated, and the fractional proton yield in this cone was specified using the assumption of isotropic yield in the center of mass coordinate system. Finally, a geometric interception factor, defined as the ratio of the area of the detector to the area of the projection of the 2π angular yield cone onto the plane of the detector, was applied. The number of proton counts was determined as seven and four for the close and far spacing runs respectively.

Because of the small magnitude of this correction, a conservative error of $\pm$ 100 % is associated to it. The correction is trivial and further error evaluation unwarranted.

3. Summary of Charged Particle Correction.

The results of the charged particle correction and the associated errors, including their effect on the total number of primary data events are shown in Table 6.10.

Table 6.10.

Summary of Charged Particle Correction and

Its Effect on Primary Event Data

(Errors are one standard deviation,
shown as a per cent of associated term)

Source - Detector Spacing	Charged Particle Correction, Counts		Primary Events	
	Epoxy	Air	Uncorrected	Corrected
Close				
inc. I-B-7	$7 \pm 100\%$	$702 \pm 80\%$	$4900 \pm 2.1\%$	$4191 \pm 13.6\%$
exc. I-B-7	$6 \pm 100\%$	$634 \pm 80\%$	$4425 \pm 2.3\%$	$3785 \pm 13.7\%$
Far	$4 \pm 100\%$	$263 \pm 80\%$	$1357 \pm 5.4\%$	$1090 \pm 20.4\%$

CHAPTER VII

CROSS SECTION EVALUATION

A. Integral Value of the ^{6}Li (n,α) Cross Section.

1. General Comments.

An integral value for the ^{6}Li (n,α) cross section, i.e. the value relative to the energy spectrum of the Na-Be photoneutron source, will be derived by two methods. Both these techniques eliminate the effects of room return neutrons. The first method is simply an algebraic solution of two simultaneous linear equations. The second method, corroborating the results obtained by the first technique, graphically illustrates the room return effects.

2. Method 1 - Algebraic Elimination of the Room Return Flux Contribution.

Making the assumption that the number of events due to the room return flux is dependent only on the integrated activity of the photoneutron source and independent of small variations in the source - target spacing, Equation 7.A.1 is obtained.

$$N_C/\epsilon = N\bar{\sigma}F\left(1 + \delta\phi/\phi_o\right) + KA \qquad 7.A.1.$$

where,

N_c = Number of neutron counts,

ϵ = Detection efficiency,

N = Number of target nuclei,

$\bar{\sigma}$ = Integral ^{6}Li (n,α) cross section,

F = Mean scalar fluence,

$\delta\phi/\phi_o$ = Local inscatter correction,

A = Integrated source neutron activity, and

K = a constant, independent of source- target spacing.

Letting the subscripts I and II denote the close and far spacing data and correction terms, respectively, we have

$$N_C^I/\epsilon = N\bar{\sigma}F_I\left(1+\delta\phi/\phi_o\right)_I + KA \qquad 7.A.2.$$

$$N_C^{II}/\epsilon = N\bar{\sigma}F_{II}\left(1+\delta\phi/\phi_o\right)_{II} + KA \qquad 7.A.3.$$

Using the data and correction terms discussed in the preceding three chapters, this set of equations can be directly solved for $\bar{\sigma}$ by eliminating K. The values for the parameters are summarized in Table 7.1.

Note that data set I-B-7 will be excluded to evaluate the error due to the possible anomolous behavior suggested by the statistical analysis as discussed in Section IV.B.3. The results obtained by solving Equations 7.A.2 and 7.A.3 are shown in Table 7.2.

The error associated with the integral cross section value will be discussed in Section VII.C.

Table 7.2 also shows the contributions of room return neutrons to the count rate. The values shown in Table 7.2 are the per cent increase in the number of neutron events

Table 7.1.

Values Used in Equations 7.A.2 and 7.A.3 to Determine the Cross Section

Variable	Source - Target Spacing	
	Close (8.884cm)	Far (19.986 cm)
	I	II
ϵ, %	90.5	90.5
N, ^{6}Li nuclei	8.4067×10^{18}	8.4067×10^{18}
$\delta\phi/\phi_0$, %	6.3	7.95
N_c, neutron events*	4191 (a) 3785 (b)	1090
A, integrated activity, sec^{-1}	1.5036×10^{12} (a) 1.3773×10^{12} (b)	1.7517×10^{12}
F, mean scalar fluence, cm^{-2}	1.53×10^{9} (a) 1.40×10^{9} (b)	3.50×10^{8}

(a) Data set I-B-4 excluded

(b) Data sets I-B-4 and I-B-7 excluded

*Correction included for ^{14}N (n, p) reaction in air and epoxy.

above that due to direct (source) neutrons because of room return neutrons. The increase in the room return contribution as the source - target spacing was increased is a direct consequence of the assumption of constancy of the room return contribution for small changes in the source - target spacing. Since the direct flux varies as R^{-2}, where R is the source target spacing, the direct flux decreased by approximately $(2.25)^2$, the square of the ratio of the source - target distance for the close and far spacing runs. The ratio of the room return contribution to the direct contribution increased by this same factor.

Table 7.2.

Integral Cross Section Values and Room Return Contributions Obtained by Solution of Equations 7.A.2 and 7.A.3

Case	$\bar{\sigma}$, mb	Room Return Contribution % Increase	
		Close	Far
Reference	326.0	3.1	14.0
Excluding Data Set I-B-7 (For error analysis)	320.2	3.5	15.5

3. Method Two - The Apparent Cross Section.

This method is essentially a graphical technique, or linear fitting, to eliminate the room return contribution. The analysis follows that given by Gilliam and Knoll (Gil, 75) for their analysis of the ^{235}U fission cross section.

Equation 7.A.1 is rewritten in the form

$$N_C = \epsilon N \bar{\sigma} F \left| 1+\delta\phi/\phi_o \right| + \epsilon_w N \bar{\sigma}_w F_w \qquad 7.A.4.$$

where, the subscript "w" denotes room return components. ϵ_w, the detection efficiency for events due to room return neutrons is an unknown constant, differing from ϵ, the detection efficiency for direct neutron events. $\bar{\sigma}_w$ is the cross section relative to the room return neutron spectrum, presumably larger than $\bar{\sigma}$ because of the moderation which occurs in the concrete walls. F_w is the room return fluence, assumed independent of the source - target spacing but depending on the integrated neutron activity of the photoneutron source, and implicitly containing an inscatter correction term.

The apparent cross section is defined by Equation 7.A.5.

$$\sigma_A \equiv N_C / \left| \epsilon N F \left| 1+\delta\phi/\phi_o \right| \right| \qquad 7.A.5.$$

$$= \bar{\sigma} + \frac{\epsilon_w \bar{\sigma}_w F_w}{\epsilon F \left| 1+\delta\phi/\phi_o \right|}$$

The dependence of the numerator in the fractional term of Equation 7.A.4 on A, the integrated neutron activity of the source, is eliminated by dividing numerator and denominator by A, denoting F_w/A by F'_w .

$$\sigma_A = \bar{\sigma} + \epsilon_w \bar{\sigma}_w F'_w / \epsilon F A^{-1} \left| 1 + \delta\phi/\phi_o \right| \qquad 7.A.6.$$

If σ_A is plotted as a function of $\left[\epsilon F A^{-1} \cdot (1 + \delta\phi/\phi_o)\right]^{-1}$, the intercept obtained by extrapolation to $\left[\epsilon F A^{-1} \cdot (1 + \delta\phi/\phi_o)\right]^{-1} = 0$ gives the cross section relative to the source neutron spectrum. This is readily achieved since σ_A is linear in this variable.

The mean scalar fluence, F, is nearly proportional to $1 / R^2$, where R is the measured source to target spacing. It is exactly proportional to $1 / R_e^2$, where R_e is an effective source - target spacing defined by Equation 7.A.7.

$$F = A / \left[4\pi R_E^2 \left| 1 + \delta\phi/\phi_o \right| \right] \qquad 7.A.7.$$

Figure 7.1 shows a plot of σ_A versus $\left[\epsilon F \left| 1 + \delta\phi/\phi_o \right| A^{-1}\right]^{-1}$ and R_e^2. The calculated values, plotted in Figure 7.1, are shown in Table 7.3. Again, the cross section was evaluated with and without data set I-B-7.

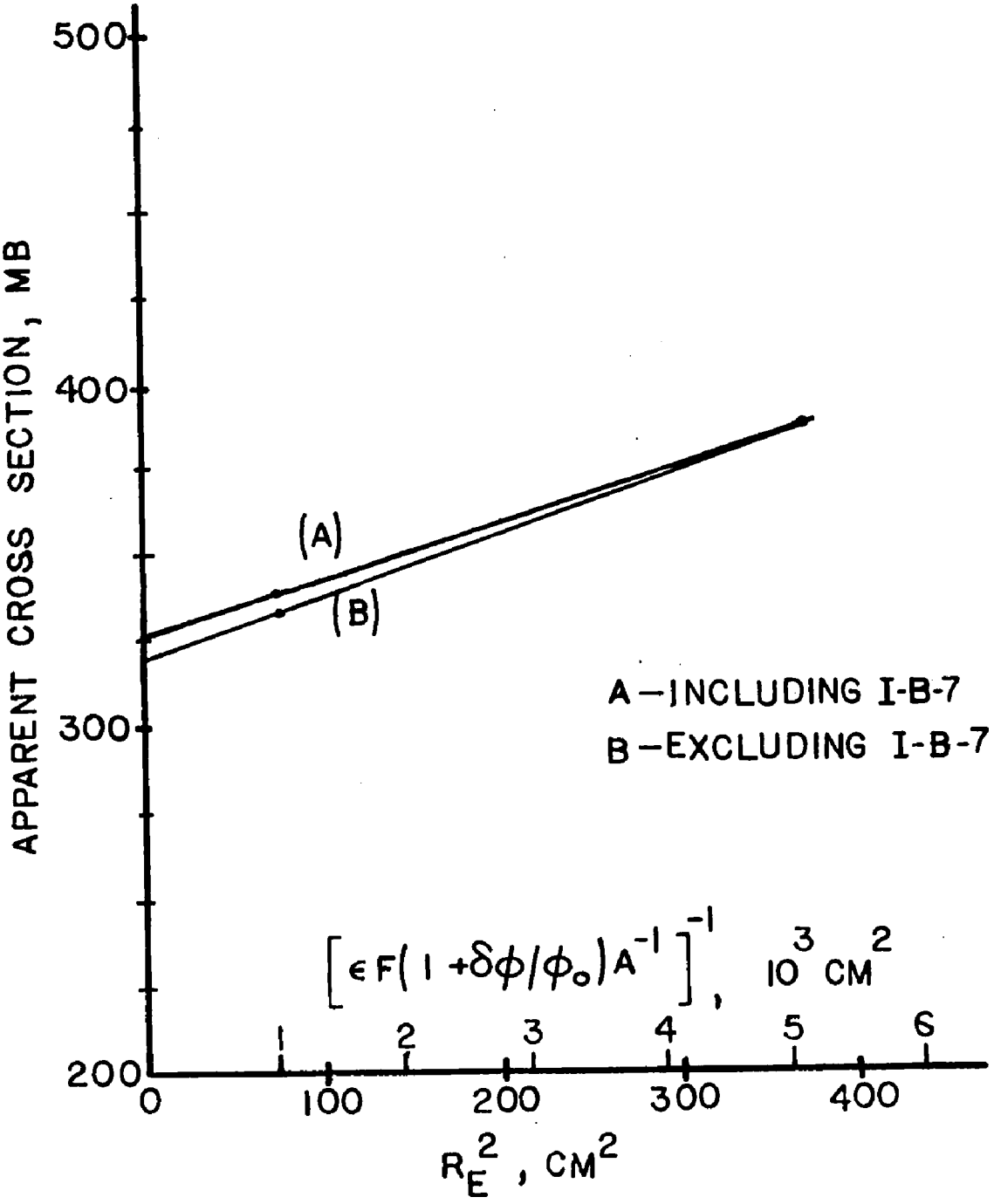


Figure 7.1. The Apparent Integral Cross Section

Table 7.3

Values of the Apparent Cross Section and

Its Linearly Dependent Variables

Source - Target Spacing, cm	$[\epsilon F(1+\delta\phi/\phi_o)A^{-1}]^{-1}$, 10^3 cm^2	Re^2, cm^2	σ_a, mb
8.884	1.0082 (a) 1.0087 (b)	73.09 (a) 73.13 (b)	336.5 (a) 331.9 (b)
19.986	5.0892	368.9	379.2

(a) Including I-B-7

(b) Excluding I-B-7

A linear fit to the data points gives intercepts of 326.0 mb and 320.2 mb, respectively, including and excluding data set I-B-7, in agreement with the results obtained by method one. The integral cross section value is the linear average of the values obtained by including and excluding data set I-B-7, 323.1 mb.

B. Value of the ^{6}Li (n,α) Cross Section at 964 keV.

The integral cross section value obtained in the preceding section (Section VII.A) is dependent on the source neutron energy spectrum and on the shape of the ^{6}Li (n,α) cross section over the energy range of

the source neutrons. These dependencies limit the usefullness of the value obtained as well as inhibit comparison of the result with values obtained by other experimenters. These dependencies will be eliminated by using the energy dependent shape function for the ^{6}Li (n, α) cross section reported by Friesenhahn (Fri, 74) and the energy spectrum of the source neutrons given in Appendix I. The formalism is defined by Equation 7.B.1 where,

$Q(E)$ = energy dependent distribution function of the Na-Be source neutrons,

$\sigma(E)$ = cross section shape function,

$\sigma(964)$ = shape function at 964 keV

$\bar{\sigma}$ = integral cross section, relative to the photoneutron source spectrum, and

σ_{964} = spectrum unfolded cross section value.

$$\sigma_{964}/\bar{\sigma} = \frac{\sigma(964)\int Q(E)\,dE}{\int Q(E)\sigma(E)\,dE} = \frac{\int Q(E)\,dE}{\int Q(E)\,\frac{\sigma(E)}{\sigma(964)}\,dE} \qquad 7.B.1.$$

The energy dependence of the cross section and that of the source neutrons is illustrated in Figure 7.2. The source neutron spectrum is shown as an integral plot to display the rapid decrease in the direct flux as energy

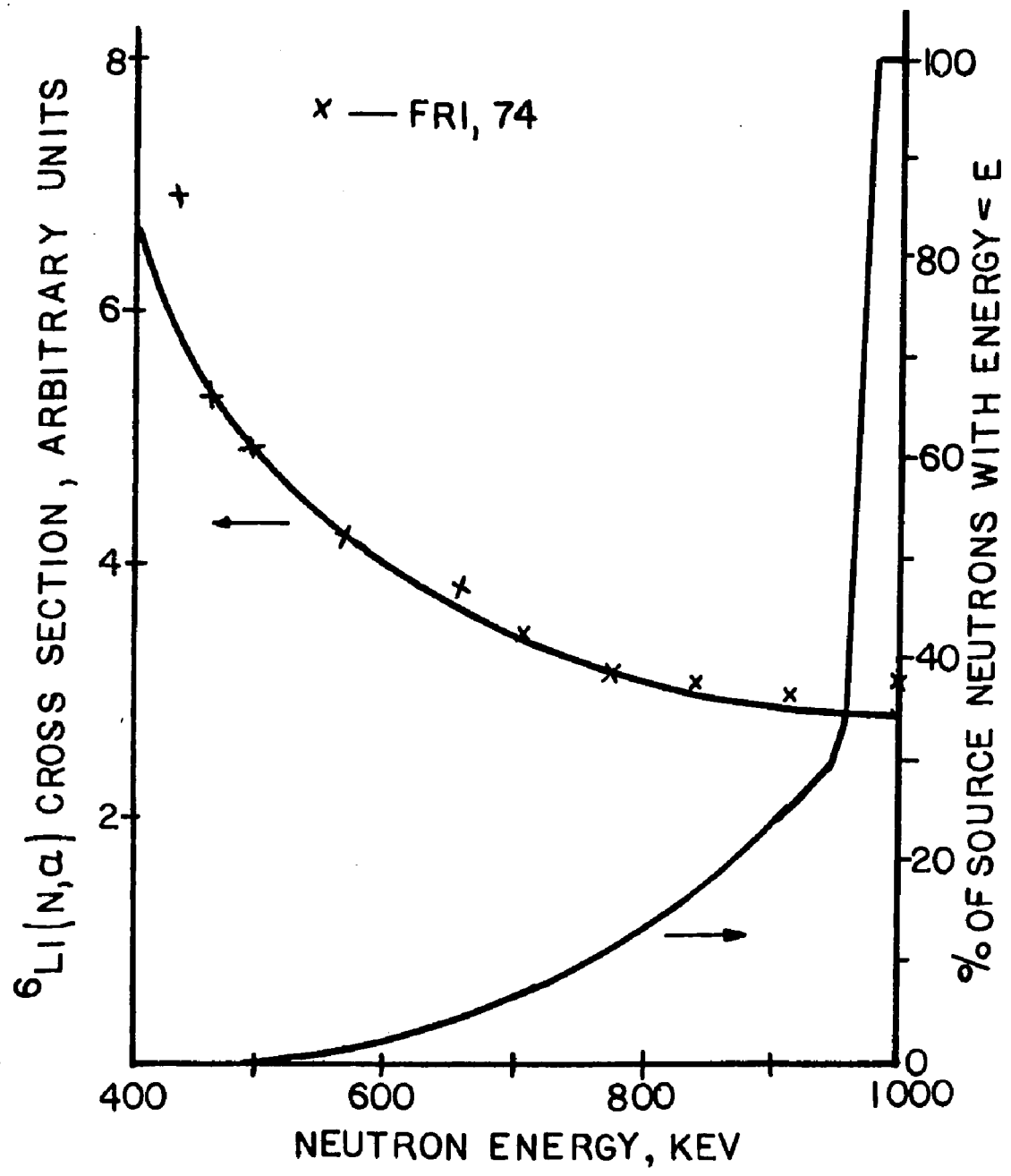


Figure 7.2. ^{6}Li(n,α)Cross Section Shape Function and Integral Neutron Source Spectrum

decreases, with less than 0.9% of the source neutrons having energies below 500 keV. The high energy wing of the resonance in the ^{6}Li (n,α) cross section at 245 keV does not cause a large change in the calculated value, σ_{964}, compared with the integral result, $\bar{\sigma}$.

The cross section values obtained from the Friesenhahn data at the energies corresponding to the midpoints of the source energy spectrum values are shown in Appendix II. Combining these with the source energy distribution function gave the following result:

$$\sigma_{964} = 0.952\bar{\sigma} \qquad 7.B.2.$$

Evaluating Equation 7.B.2 using $\bar{\sigma}$= 323.1 mb, gives 307.6 mb as the cross section value at 964 keV. The error associated with these values is discussed in the following section.

C. Error Evaluation.

1. General Comments.

To assign an error to the final value of the cross section requires combining all of the previously discussed error terms. This will be done by explicitely summarizing these terms and their associated errors and then combining them using a standard error propagation formulation in terms of Equation 7.A.1. Having deter-

mined the error associated with the integral cross section value, the additional error inherent in proceeding to the point value at 964 keV will be included.

Equation 7.A.2 and 7.A.3 were rewritten in a combined form algebraically eliminating the room return background proportionality constant k, giving Equation 7.C.1.

$$\bar{\sigma} = \frac{\epsilon \left(N_C^I - N_C^{II} A^I / A^{II} \right)}{N\left[F^I \left(1 + \delta\phi/\phi_o \right)_I - F^{II} \left(1 + \delta\phi/\phi_o \right)_{II} \frac{A^I}{A^{II}} \right]} \qquad 7.C.1.$$

where the I and II denote the close and far spacing runs, respectively. There are ten independent variables in Equation 7.C.1, whose values and associated errors have been defined and which are summarized in Table 7.4.

First the error in the integral cross section will be evaluated viewing the error sources as independent, then including correlated uncertainties. Next, the magnitude of the random versus systematic error sources will be discussed. Finally, the residual uncertainty in the cross section value at 964 keV will be evaluated.

2. Estimated Uncertainty in the Integral Cross Section.

The error in $\bar{\sigma}$ can be determined from Equation 7.C.1 by evaluating of the partial derivatives of $\bar{\sigma}$ with respect to each of the dependent variables. For uncorrelated variables, the error was evaluated using Equation 7.C.2 in which u_i represents the i^{th} variable.

Table 7.4.

Variable Values and Associated Errors

for Determination of the Integral Cross Section

Variable Description	Value Error (One Standard Deviation) is Shown as % of Value Close Spacing Run I	Far Spacing Run II
ϵ, Detection Efficiency, %	.905 ± 0.54	.905 ± 0.54
N_c, Neutron Events	4191 ± 13.6%	1090 ± 20.4%
A, Integrated Neutron Activity	1.5036×10^{12} ± 0.88%	1.7517×10^{12} ± 0.92%
N, ^{6}Li Nuclei	8.4067×10^{18} ± 1.7%	8.4067×10^{18} ± 1.7%
F, Mean Scaler Fluence, cm^{-2}	1.53×10^{9} ± 1.2%	3.5×10^{8} ± 1.2%
$(1 + \delta\phi/\phi_o)$, Inscatter Correction	0.063 ± 65%	0.0795 ± 65%

$$\sigma_i^2 = \sum_{i=1}^{10} \left(\frac{\partial \bar{\sigma}}{\partial u_i}\right)^2 \sigma_{u_i}^2 \qquad 7.C.2.$$

For interdependent error terms, the error contribution was evaluated using Equation 7.C.3.

$$\sigma_{i,j}^2 = \sum_{\substack{i,j \\ i \neq j}} 2\left(\frac{\partial \bar{\sigma}}{\partial u_i}\right)\left(\frac{\partial \bar{\sigma}}{\partial u_j}\right) \sigma_{u_i}\sigma_{u_j} \qquad 7.C.3.$$

The error in the cross section value was then obtained from Equation 7.C.4.

$$\sigma_{\bar{\sigma}}^2 = \sigma_i^2 + \sigma_{i,j}^2 \qquad 7.C.4.$$

The error terms were individually evaluated and will be quoted as a per cent relative to the 323.1 mb cross section value. Subsequently they are combined in quadrature as defined by Equation 7.C.4.

The calculated values for the independent uncertainties of $\bar{\sigma}$ are shown in Table 7.5.

The contribution of cross correlated uncertainties to the error in the integral cross section are summarized in Table 7.6. To simplify the analysis it was conservatively assumed that correlation between two error terms via an implicit variable is equivalent to direct correlation between the terms themselves. For example, N, the number of target nuclei is implicitly cross correlated with ϵ, the detection efficiency through the target radius and mass thickness determinations.

Table 7.5.

Independent Error Sources

Variable	Error Contribution as % of $\bar{\sigma}$ (328.2 mb)
ϵ	.446
N_C^I	14.49
N_C^{II}	4.84
A^I	.029
A^{II}	.406
N	1.404
F^I	1.216
F^{II}	.245
$(1 + \delta\phi/\phi_o)_I$	3.969
$(1 + \delta\phi/\phi_o)_{II}$	0.977
Combined Error	15.9 %

Table 7.6.

Cross Correlated Error Sources

Variables u_i, u_j	Correlation Type	Contribution as % of $\bar{\sigma}$ (323.1mb)
A^I, F^I	Explicit	.269
A^{II}, F^{II}	Explicit	.446
A^I, A^{II}	Implicit	.154
F^I, F^{II}		.778
N, ϵ		1.119
$(1+\delta\phi/\phi_o)_I$, $(1+\delta\phi/\phi_o)_{II}$		2.78
F^I, $(1+\delta\phi/\phi_o)_I$		3.133
F^{II}, $(1+\delta\phi/\phi_o)_{II}$		0.692
N, F^I		1.863
N, F^{II}	Implicit	0.829
Combined Error		4.93%

However, the cross correlation contribution from this term was taken to be $2\left|\frac{\partial\bar{\sigma}}{\partial N}\right|\left|\frac{\partial\bar{\sigma}}{\partial\epsilon}\right|\sigma_N\sigma_\epsilon$ so that the total error in N and ϵ, i.e., σ_N and σ_ϵ, is considered as contributing, rather than only the partial error due to uncertainties in the target radius and mass thickness determinations.

Combining the errors tabulated in Tables 7.5 and 7.6 in quadrature according to Equation 7.C.4, the total error in the integral cross section was determined to be 16.6%, or $\pm$ 53.6 mb. The result for the integral cross section including the error is, then

$$\bar{\sigma} = 323.1 \text{ mb} \pm 16.6\%$$

An additional systematic error term must be included, as discussed in Sections IV.B and VII.A, namely that due to the anomolous detector response during data acquisition interval I-B-7. The uncertainty in $\bar{\sigma}$ due to this source will be linearly added to the above derived 16.6%. The error is taken as $\pm$ 3.0 mb, the empirically determined variation calculated in Section VII.A. This corresponds to $\pm$ 0.90%, giving the integral cross section error as $\pm$ 17.5%.

3. Estimated Uncertainty in the Cross Section Value at 964 keV.

There are two error sources to be considered in the procedure of going from the integral cross section value to

the value at the mean energy of the source neutrons, 964 keV. The additional error in σ_{964} due to uncertainties in the computed neutron spectrum and in the energy dependent cross section were evaluated empirically.

As regards the effect of the computed spectra, the adjustment in the cross section was recalculated using Friesenhahn's cross section shape function and the spectrum computed by the Bensch - Vesely code (Ben, 69) as obtained by Gilliam (Gil, 73). The result, as shown in Table 7.7, influences the correction factor by a few tenths of a per cent.

Table 7.7.

Effect of Source Spectrum

Calcuation on σ_{964}

Monte Carlo Code	$\bar{\sigma}$ to σ_{964} Correction Factor
Ryves / Robertson	0.952
Bensch / Vesely	0.950

As regards the influence on the value at 964 keV due to uncertainties in the energy dependence of the ^{6}Li (n,α) cross section, the integral to point correction factor was recalculated using the Ryves-Robertson source spectrum and the energy dependent cross section values of Clements and Rickard (Cle, 72)

and of Gabbard (Gab, 59). The results are shown in Table 7.8.

Table 7.8.

Effect of the ^{6}Li (n,α) Cross Section Shape Function on σ_{964}

Data Source for σ(E)	$\bar{\sigma}$ to σ_{964} Correction Factor
Friesenhahn	0.952
Clements/ Rickard	0.951
Gabbard	0.960

The cross section value at 964 keV is relatively insensitive to variations in the source energy spectrum and to the particular cross section energy dependent shape function used to obtain the point value at 964 keV. An additional error of $\pm$ 0.5% in the value at 964 keV compared with the error in $\bar{\sigma}$ is the maximum added uncertainty. The value obtained for the ^{6}Li (n,α) cross section at 964 keV is 307.6 mb $\pm$ 18%.

The 18% error in the cross section is dominated by the systematic error due to the proton contribution from the air space surrounding the detector. Before combining the error terms in quadrature, the contribution of random error sources is 3.5%, that due to systematic error sources via correction terms is 17.7%. Table

7.9 summarizes the results.

Table 7.9.

Summary of Final Cross Section Values and Errors

Cross Section	Total Error	Partial Error and Source
Integral Value 323.1 mb	16.6%	3.5% - Random 16.2% - Systematic (^{14}N (n, p) Correction Dominates)
	17.5%	0.9% - Systematic (Error Contributed From Possibility of Anomolous Detector Behavior)
Value at 964 keV, 307.6 mb	18.0%	0.5% - Systematic (Error From Uncertainties In Integral to Point Value Reduction)

CHAPTER VIII

CONCLUSION

A. Comparison With Other Data.

The cross section value obtained in this work is shown in comparison with other values in Figure 8.1. With the exception of the data of Gabbard (Gab, 59) all the work represented has been done since 1971 (Cle, 72; Fri, 74; Poe, 74; For, 72). In the 1971 review of the status of the ^{6}Li (n,α) cross section the need for direct measurements of the ^{6}Li (n,α) cross section between 600 keV and 1000 keV was stressed, using various techniques so that systematic errors could be eliminated (Ut, 71). The error in the cross section near 1 MeV was then estimated as $\pm$ 15%.

The 308 mb value is in excellent agreement with the earlier results of Gabbard and with the recent data of Friesenhahn. However, the 18% error bar on the value prohibits strongly associating this value with the data of Gabbard and Friesenhahn rather than with those of Poenitz and Fort.

One purpose in undertaking this measurement was to produce an absolute, unnormalized value for the cross section in this energy range. The data of Poenitz and of Fort are also absolute since, for both measurements, the neutron flux was determined without normalization.

Although not contributing to the refinement of the

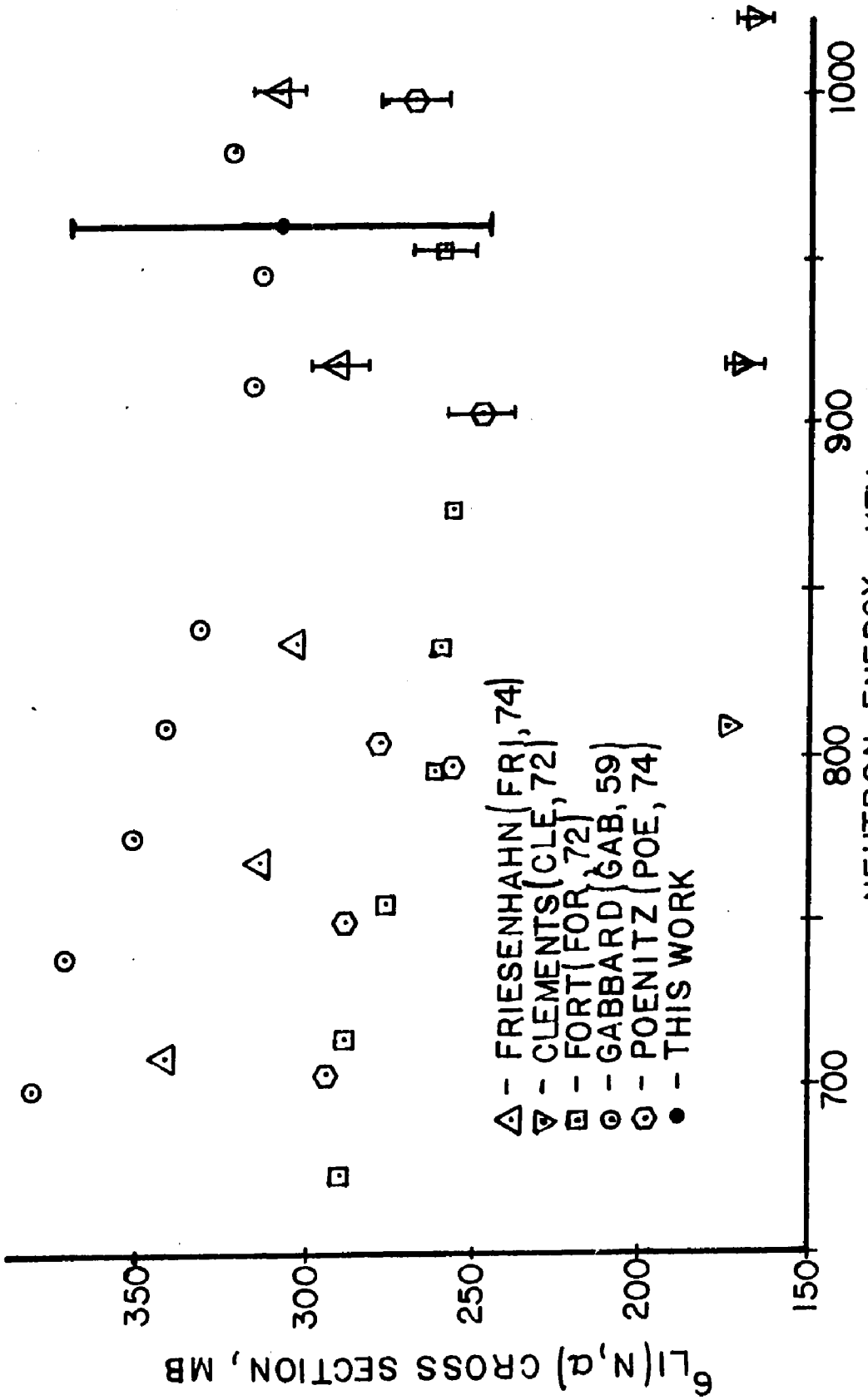


Figure 8.1. Comparison of This Result with Other Values

± 15% error in the cross section, this result definitely shows the cross section is substantially above the 168 mb value obtained by Clements. The Friesenhahn data are about 12% higher at 964 keV than those of Poenitz and Fort. The approximately 4% errors associated with these data may not include systematic uncertainties.

B. Comments and Suggestions.

Three problems seriously affected the degree of accuracy of the result. First, the unanticipated complications of operating the surface barrier detector in the high gamma flux led to lengthy in situ experimentation to obtain a suitable pulse processing system. By the time a suitable system was operational, the performance of the detector itself was degraded, showing a tendency toward instability and exhibiting poor resolution. The other two problems are the large correction terms for local inscatter and charged particle (proton) production in the air space surrounding the detector.

A high accuracy ^{6}Li (n,α) cross section measurement using a surface barrier detector with the photoneutron source could be achieved if the following conditions were met: 1) the target deposits should be at the center of a substantially larger silicon disk so that the lavite ring, a major inscatterer, is several centimeters from the target edge; 2) a low capacitance or equivalently, a small electrode surface

area detector should be used, e.g.; a 4 cm diameter silicon disk with 1 cm diameter electrode surface at the center; 3) the target deposit should be on only one side of the detector, facing the source; 4) the charged particle problem should be physically precluded by suitable shielding.

The first condition, along with careful detector mount design, would eliminate the large inscatter correction. The second condition would allow a fast pulse, in the tens of nanoseconds full width range, to be processed, thereby making pileup problems insignificant. The third condition takes advantage of the forward peaking of the reaction product distribution in the laboratory coordinate system, giving a 100% intrinsic efficiency factor for the detector - target composite. The fourth condition is especially relevant to this experiment. Using an unshielded surface barrier detector for detecting specific charged particles in the low MeV range is, with clear hindsight, a precarious path. It leaves the question as to possible unknown charged particle interference open. The same problem would arise in using, for example, a mica film to record the events from the ^{6}Li (n,α) reaction under the same experimental conditions as this measurement.

APPENDIX I

Tabulated Photoneutron Source Energy Spectrum

Energy, keV (Upper End of Interval	ΔE, keV (Interval Width)	Q (E), 10^{-5} sec^{-1} keV^{-1}
980	10	2675.0
970	|	2549.6
960	|	1216.8
950	|	1121.4
940	|	107.15
930	|	101.90
920	|	105.90
910	10	101.15
900	20	89.042
880	|	79.179
860	|	87.667
840	|	78.297
820	|	74.800
800	|	69.684
780	|	63.381
760	|	57.572
740	|	57.383
720	|	54.200
700	|	47.142
680	|	42.646
660	|	38.340
640	|	34.905
620	20	24.852
600	40	16.535
560	|	13.316
520	|	10.381
480	|	7.212
440	|	3.872
400	|	2.216
360	|	1.046
320	|	0.5463
280	40	0.2810
240	240	0.0546

The Q (E) distribution is normalized to 1 neutron/sec total emission. This spectrum was computed by Ryves and Robertson using the Monte Carlo code developed at NPL (Ryv, 71)

APPENDIX II

$^{6}Li(n,\alpha)$ Cross Section Shape Function Reported by Friesenhahn (Fri, 74) As Used to Determine σ_{964}

$\sigma(964) = 285.33$ mb

E, keV	σ(E), mb	E, keV	σ(E), mb
975	284.16	580	414.01
965	285.23	540	439.25
955	286.30	500	482.40
945	287.37	460	556.85
935	288.44	420	735.88
925	289.52	380	903.69
915	290.59	340	1267.87
905	292.31	300	2284.22
		260	3664.17
890	294.96		
870	298.50	240	3766.20
850	302.03		
830	305.69		
810	309.55		
790	313.41		
770	317.27		
750	325.55		
730	333.83		
710	342.20		
690	356.02		
670	369.84		
650	381.21		
630	388.35		
610	395.51		

LIST OF REFERENCES

Abd 73 M. A. Abdou, C. W. Maynard and R. Q. Wright, ORNL-TM-3994, (July, 1973).

Ada 72 H. Adair, Isotope Target Laboratory, Oak Ridge National Laboratory, private communication, (1972).

Al 68 W. E. Alley, R. W. Gell, and R. M. Lessler, UCRL-50484, (August, 1968).

Ax 65 E. J. Axton, P. Cross, and J. C. Robertson, Journal of Nuclear Energy A/B, 19, 409 (1965).

Bab 61 R. V. Babcock, Westinghouse Electric Corp. report AFSWC-TR-61-57, (August, 1961).

Ben 69 F. Bensch and F. Vesely, Journal of Nuclear Energy A/B, 23, 537 (1969).

Bul 60 R. E. Bullock and R. J. Moore, Jr., Physical Review, 119, No. 2, 721 (July, 1960).

Cle 72 P. J. Clements and I. C. Rickard, AERE-R 7075, (1972).

Der 70 A. J. Deruytter, Proceedings of the Second International Conference on Nuclear Data for Reactors, Helsinki, IAEA-CN-26/106, (1970).

DeV 69 A. DeVolpi, Metrologia, 5, 128 (1969).

Dui 71 Y. Le Duigou and K. F. Lauer, Nuclear Instruments and Methods, 97, 199 (1971).

Em 72 J. F. Emery, S. A. Reynolds, E. I. Wyatt and G. I. Gleason, Nuclear Science and Engineering, 48, 319 (1972).

For 72 E. Fort and J. P. Marquette, Proceedings of the Second IAEA Panel on Neutron Reference Data, Vienna, EANDC(E)-148, (1972).

Fri 74 S. J. Friesenhahn, V. J. Orphan, A. D. Carlson, M. P. Fricke and W. M. Lopez, INTEL-RT 7011-001, (February, 1974).

Gab 59 F. Gabbard, R. H. Davis, and T. W. Bonner, Physical Review, 114, 201 (1959).

Gar 68 B. Garbow, Argonne National Laboratory Code Center, ANL-E3505, (1968).

Gil 73 D. M. Gilliam, Doctoral Dissertation, Department of Nuclear Engineering, University of Michigan, (1973).

Gil 75 D. M. Gilliam and G. F. Knoll, (1975), (to be published in Annals of Nuclear Science and Engineering).

How 64 R. J. Howerton, D. Braff, W. J. Cahill, and N. Chazan, UCRL-14000, (May, 1964).

Huy 70 V. D. Huynh, L. Lafaye, and P. Bréonce, Procès-Verbaux Comité International des Poids et Mesures, 38, 76 (1970).

Kob 75 E. Kobisk, Isotope Target Laboratory, Oak Ridge National Laboratory, private communication, (1971).

Map 66 C. Maples, G. W. Goth, and J. Cerny, UCRL-16964, (July, 1966).

Mer 71 J. S. Merritt and J. G. V. Taylor, Progress Report AECL-3912, 43 (1971).

NAS 64 National Academy of Sciences, National Research Council Publication 1133; Nuclear Science Series Report No. 39, 111 (1964).

Nor 70 L. C. Northcliffe and R. F. Schilling, Nuclear Data Tables, A7, 233-461 (1970).

Noy 63 R. H. Noyce, E. R. Mosburg, Jr., S. B. Garfinkel and R. S. Caswell, Journal of Nuclear Energy A/B, 17, 313 (1963).

Poe 74 W. Poenitz, Zeitschrift für Physik, 268, 359 (1974).

Ric 72 I. C. Rickard, Nuclear Instruments and Methods, 105, 397-411 (1972).

Ryv 71 T. B. Ryves and J. C. Robertson, National Physical Laboratory, private communication, (1971).

Spa 73 H. Spang, Spang Microanalytical Laboratory, Ann Arbor, Michigan, private communication, (1973).

Spi 72 V. Spiegel, Jr., National Bureau of Standards, private communication to D. M. Gilliam, (1972).

Ueh 60 E. A. Uehling, National Academy of Sciences, National Research Council Publication 752; Nuclear Science Series Report No. 29, (1960).

Ut 71 C. A. Uttley, M. G. Sowerby, B. H. Patrick, and E. R. Rae, Proceedings of the Symposium on Neutron Standards and Flux Normalization, Argonne National Laboratory, CONF-701002, 80 (August, 1971).

Wap 71 A. H. Wapstra, Nuclear Data Tables, 9, 265-468 (1971).

Wed 59 J. B. Weddell and J. H. Roberts, Physical Review, 95, No. 1, 117 (1954).

Wil 66 C. F. Williamson, J. Boujot, and J. Picard, CEA-R 3042, (1966).